

**Identification
of Sources in
MAMBO 1.2mm Deep Fields**

Dissertation der Fakultät für Physik
der Ludwig-Maximilians-Universität München

vorgelegt von
Helmut Dannerbauer
aus München

25. Mai 2004

Erstgutachter: Prof. Dr. Reinhard Genzel

Zweitgutachter: PD Dr. Hans Böhringer

mündliche Prüfung: 12. Januar 2005

Zusammenfassung

Seit Winter 1998/1999 führen Gruppen am Max-Planck-Institut für Radioastronomie (MPIfR), Max-Planck-Institut für extraterrestrische Physik (MPE) und dem National Radio Astronomy Observatory (NRAO) bei 1.2 mm eine tiefe, große Gebiete abdeckende Himmelsdurchmusterung mit dem Max-Planck-Millimeter Bolometer Array (“MAMBO”) am IRAM 30-m Millimeterteleskop durch, um eine signifikante Anzahl von hellen mm-Quellen zu detektieren. Diese Quellen sind höchstwahrscheinlich staubreiche Galaxien bei hoher Rotverschiebung mit Sternentstehungsraten von bis zu einigen Tausend Sonnenmassen pro Jahr. Kosmologisch gesehen sind sie hochinteressant, da sie signifikant zum extragalaktischen kosmischen Hintergrund, d.h. zur Stern- und Galaxienentwicklungsgeschichte des Universums, beitragen. Zum Verständnis ihrer Natur sind Identifikationen mit Hilfe tiefer optischer und Nahinfrarotaufnahmen essentiell.

Aufgrund der geringen Winkelauflösung des IRAM 30-m Millimeterteleskopes ($10.7''$) ist eine eindeutige Identifikation der mm-Quellen, die nur auf Bolometerdaten basiert, unmöglich. Deshalb ist die mm- und cm-Interferometrie ein Schlüsselement in der Nachbeobachtung dieser staubhaltigen, hochrotverschobenen Quellen. Unsere Identifikationsstrategie basiert auf der Kombination von radio- (VLA) und millimeter- (PdBI) interferometrischen Beobachtungen, um die genauen Positionen der mm-Quellen zu bestimmen, und optischen/Nahinfrarotaufnahmen zur eigentlichen Identifikation. Ziel dieser Arbeit ist die Identifizierung und Charakterisierung der Quellen der mm-Strahlung, fokussierend auf das auf der südlichen Himmelskugel gelegene NTT Deep Field und seine Umgebung.

Im Winter 2000/2001 wurden mit dem mm-Interferometer PdBI Beobachtungen durchgeführt, um exakte Flüsse und Positionen von einigen der hellsten MAMBO-Quellen bestimmen zu können. Vier wurden erfolgreich auf einem 5σ -Niveau mit dem PdBI detektiert. Für alle PdBI-Detektionen konnten auch schwache Radiogegenstände detektiert werden. Interessanterweise offenbarten die Positionen, die durch die interferometrischen Beobachtungen exakt bestimmt werden konnten, dass keine dieser MAMBO-Quellen ein Gegenstück im Nahinfraroten bis zu sehr schwachen Magnituden besitzt ($K \sim 22.0$ mag). Diese tiefen K-Band Grenzen der helleren 1.2 mm MAMBO-Quellen setzen strikte Beschränkungen hinsichtlich der Natur und Rotverschiebung dieser Objekte: Falls die spektrale Energieverteilung der mm-Quellen denen der ultraleuchtkräftigen Infrarotgalaxien (ULIRGs) ähnelt, dann müssten sie bei Rotverschiebungen größer als 4 liegen, was einem Zeitpunkt von etwa 1.5 Mrd Jahren nach dem Urknall entspricht. Andernfalls könnten sie bei niedrigeren Rotverschiebungen sein, müssten jedoch UV-optische Farben besitzen, die röter sind als selbst die der extremsten ULIRGs, wie zum Beispiel Arp 220. Unsere Analyse basierend auf nahinfrarot/radio/(sub)mm Daten zeigt, dass es einen Trend zwischen den Flussverhältnissen nahinfrarot-zu-submm und radio-zu-submm gibt. Dieses Ergebnis deutet daraufhin, dass die geringe Helligkeit im K-band von unseren PdBI-Detektionen in erster Linie auf die hohe Rotverschiebung dieser Objekte zurückzuführen ist.

Durch eine Korrelation zwischen Radioquellen, die sich nahe der nominalen mm-Position befinden und unseren tiefen optischen/Nahinfrarotaufnahmen konnte die Anzahl von sicher identifizierten MAMBO mm-Quellen auf 18 signifikant erhöht werden. Für 13 1.2 mm-Quellen wurden optische/NIR Gegenstücke gefunden, deren K-band Magnituden zwischen 19 und 22.5 liegen. Fünf MAMBO-Quellen sind “Blank Fields” und sind schwächer als $K > 22$ mag. Basierend auf dem radio/mm Spektralindex, wurde der Median der Rotverschiebung der radio-identifizierten mm-Quellen berechnet: $z \sim 2.6$. Der Median der optischen/NIR photometrischen Rotverschiebung für mm-Quellen mit einem Gegenstück ist ~ 2.1 . Dies weist daraufhin, dass die radio-identifizierten mm-Quellen ohne einem optischen/NIR Gegenstück dazu tendieren, bei höheren Rotverschiebungen als die mit optischen/NIR Gegenstücken zu liegen. Ein Vergleich mit publizierten Identifikationen von Objekten aus 850 μ m-Durchmusterungen (SCUBA) von vergleichbarer Tiefe zeigt, dass die K- und I-Magnituden unserer Gegenstücke etwa 2 mag schwächer sind und die Dispersion der I-K Farbe geringer ist. Tatsächliche Unterschiede im Median der Rotverschiebungen, verbleibende falsche Identifikationen mit hellen Quellen, kosmische Variationen und statistisch kleine Proben tragen höchstwahrscheinlich zu dem signifikanten Unterschied bei, welcher auch die Strategie zur Messung von Rotverschiebungen beeinflusst. In dieser Arbeit werden die Eigenschaften von NIR/(sub)mm/radio spektraler Energieverteilungen unserer Galaxien und von interferometrisch identifizierten submm-Quellen aus der Literatur diskutiert. Basierend auf einem Vergleich mit submm-Quellen mit durch CO-Messungen bestätigten spektroskopischen Rotverschiebungen argumentieren wir, dass etwa zwei Drittel der (sub)mm Galaxien bei einer Rotverschiebung höher als 2.5 liegen. Wahrscheinlich ist dieser Anteil höher, wenn Quellen ohne radio-Detektion hinzugenommen werden.

ABSTRACT

In the winter of 1998/1999, groups at the Max-Planck-Institut für Radioastronomie (MPIfR), the Max-Planck-Institut für extraterrestrische Physik (MPE) and the National Radio Astronomy Observatory (NRAO) began a deep, wide 1.2 mm survey with the Max-Planck-Millimeter Bolometer Array (“MAMBO”) at the IRAM 30 m millimeter telescope whose goal was the detection of a significant number of bright mm sources. Most probably, these sources are dusty galactic systems at high redshift with star-formation rates up to several thousands of solar masses per year. From a cosmological viewpoint this source population is very interesting as it contributes significantly to the extragalactic background light and to the formation of massive galaxies. Identification of the mm sources via optical and near-infrared imaging is essential for the understanding of its nature.

Due to the large angular size of the IRAM 30 m millimeter telescope beam ($10.7''$), a proper identification of the mm sources based only on bolometric data is impossible. The key element for the follow-up of these dusty, high-redshift sources is therefore mm and cm interferometry, which can provide resolution of $\lesssim 1''$. Thus our identification strategy is based on a combination of radio (VLA) and millimeter (PdBI) interferometric observations in order to determine accurate positions of the mm sources, and optical/near-infrared imaging for the proper identification. In the framework of the aforementioned collaboration, the MPE group carries out the latter task and works together with the MPIfR group to conduct the PdBI observations of the mm sources. The aim of this work is to identify the counterparts of the mm sources.

Due to the faintness of these sources in the optical and near-infrared, our observational strategy was to obtain very deep optical and near-infrared images. Our group focuses its efforts in the southern hemisphere NTT Deep Field (NDF) and its flanking fields. Moreover, interferometric observations were carried out together with the MPIfR

(mm interferometry) and the NRAO (cm interferometry). During the winter of 2000/2001 we carried out observations with the PdBI in order to obtain accurate fluxes and positions of several of the brightest MAMBO sources — four in the NDF and one in the field of the northern galaxy cluster Abell 2125. Four mm sources were detected at a 5σ level. The PdBI-detected NDF sources are three of the brightest known, probably nonlensed (sub)mm sources. For all of the PdBI detections we also detected faint radio counterparts. Strikingly, these accurately determined interferometric positions showed that none of the MAMBO sources has a near-infrared counterpart down to faint magnitudes ($K \sim 22.0$ mag). These deep K-band limits on counterparts of the bright 1.2 mm MAMBO sources place strict constraints on the nature and the redshift of the sources: if the spectral energy distribution (SED) of the mm sources is similar to that of ultraluminous infrared galaxies (ULIRGs), then their redshift would be greater than 4 (about 1.5 billions years after the big bang). If not, they would lie at lower redshift but their UV-optical colors would be redder than even the most extreme ULIRGs, e.g., Arp 220. Our analysis based on the near-infrared/radio/(sub)mm data shows a trend between the flux ratios of near-infrared to submm and the radio to submm. This indicates that the K-band faintness of our PdBI detections is primarily due to a high redshift and not to high extinction. Due to the nondetection of the PdBI sources in the near-infrared on a 4 m telescope, we carried out follow-up observations at the Very Large Telescope (VLT; four 8 m telescopes) for the NDF sources in order to obtain even deeper near-infrared images. Two of the three PdBI sources were detected at faint magnitudes ($K = 21.9$ and $K = 22.5$ mag). The successful detection in the near-infrared shows that the spectral energy distribution of local ultraluminous infrared galaxies can be used to predict the properties of the high- z (sub)mm galaxies despite the diversity of ULIRGs.

We cross-correlated the radio sources close to the nominal mm position with our deep optical/near-infrared images thereby increasing the number of securely identified MAMBO mm sources to 18. We find thirteen 1.2 mm sources associated with optical/near-infrared objects in the magnitude range $K = 19.0$ to 22.5 mag, while five are blank fields at $K > 22$ mag. We argue from a comparison of optical/near-infrared photometric redshifts and radio/mm redshift estimates that two of the 13 optical/near-infrared objects are likely foreground objects distinct from the mm-emitting sources, one of them possibly lensing the mm source. The median redshift of the radio-identified mm sources is ~ 2.6 from the radio/mm estimator, and the median optical/near-infrared photometric redshift for the

objects with counterparts is ~ 2.1 . Although this redshift difference is marginal given the possible sources of systematic and random uncertainties, it suggests that those radio-identified mm sources without optical/near-infrared counterparts tend to lie at higher redshifts than those with optical/near-infrared counterparts. Compared to published identifications of objects from 850 μm surveys (SCUBA) of similar depth, the median K and I magnitudes of our counterparts are roughly 2 mag fainter, and the dispersion of I–K colors is less. Real differences in the median redshifts, residual misidentifications with bright objects, cosmic variance, and small-number statistics are likely to contribute to this significant difference, which also affects redshift measurement strategies. Some of the counterparts are red in J–K ($\gtrsim 20\%$), but the contribution of such mm objects to the recently studied population of near-infrared selected ($J_s - K_s > 2.3$) high-redshift galaxies is only of order a few percent. The recovery rate of MAMBO sources by preselection of optically faint radio sources is relatively low ($\sim 25\%$), in contrast to some claims of a higher rate for SCUBA sources ($\sim 70\%$). In addition to this difference, the MAMBO sources also appear significantly fainter (~ 1.5 mag in the I band) than radio-preselected SCUBA sources. We discuss the basic properties of the near-infrared/(sub)mm/radio spectral energy distributions of our galaxies and of interferometrically identified submm sources from the literature. From a comparison with submm objects having CO-confirmed spectroscopic redshifts we argue that roughly two-thirds of the (sub)mm galaxies are at $z \gtrsim 2.5$. This fraction is probably larger when including sources without radio counterparts.

Contents

1	INTRODUCTION	1
1.1	Motivation	1
1.2	Submm and mm Galaxies	4
1.2.1	Why Can (Sub)mm Sources Be Detected?	4
1.2.2	Locating and Identifying (Sub)mm Sources	5
1.2.3	Redshift Determination	7
1.3	Aim of this Thesis	8
2	OBSERVATIONS AND DATA REDUCTION	10
2.1	Introduction	10
2.2	Optical/Near-Infrared Imaging	13
2.2.1	Optical Data	14
2.2.2	NIR-Data	19
2.2.3	Combination of the Imaging Data Sets of the NTT Deep Field	21
2.3	Interferometry	25
2.3.1	1.2 mm Interferometry	25
2.3.2	1.4 GHz Interferometry	28
2.4	Spectroscopy	28
2.5	Millimeter Photometry Mode Observations	33
3	IDENTIFICATION RESULTS	37
3.1	Identification of the PdBI Detections	37
3.1.1	NTT Deep Field	37
3.1.2	Abell 2125	38
3.2	Identification of the VLA Detections	42
3.2.1	Association of MAMBO Sources with Radio Sources	42
3.2.2	Notes on Individual Objects	48
3.3	Discussion	66
3.3.1	Optical/Near-infrared Properties: Very Faint Counterparts	66
3.3.2	Dependence on Radio Properties	78
3.3.3	Optical to Radio SED Constraints	81
3.3.4	Redshift Estimates and Star-Formation-Rate Density	90
3.4	What Causes the Difference between SCUBA and MAMBO?	96
A	Photometric Redshifts of Sources in the NDF	100

<i>CONTENTS</i>	ix
Bibliography	119
List of Tables	131
List of Figures	132

Chapter 1

INTRODUCTION

1.1 Motivation

A local census of the distribution of the baryonic mass reveals — albeit with large uncertainties — that of the baryons presently locked in stars, a majority reside in spheroids (Persic & Salucci, 1992; Fukugita, Hogan, & Peebles, 1998). When and how did all these baryons come to reside in spheroids? There are two competing explanations. The classical pictures are the “monolithic collapse” of Eggen, Lynden-Bell, & Sandage (1962) and the (hierarchical) merging model of Searle & Zinn (1978). The hierarchical picture of galaxy formation and evolution is, for many excellent reasons, widely favored (e.g., Ellis, 1998). The debate is not over which model is correct — merging obviously plays an important role in galaxy evolution, so the real questions are how did star formation proceed in galaxies and is our understanding of the hierarchical framework complete. With the development of new techniques (e.g., searches for galaxies which “drop-out” in deep images; Steidel, Giavalisco, Dickinson, & Adelberger, 1996) and new technology (e.g., 10 m class telescopes and imaging mm/submm bolometers), our understanding of the cosmic history of star formation has grown rapidly and we are now in a position to begin to address the question of how and when spheroids were assembled.

To tackle this tantalizing question, different routes to investigate star formation and the formation of spheroids can be taken — an important one being the investigation of faint submm and mm sources. The search for high-redshift objects in the submm wavelength regime only became possible through the advent of new submm arrays like

SCUBA¹. Then finally, detection of faint extragalactic submm sources several years ago has opened a new exciting era in observational cosmology (e.g., Smail, Ivison, & Blain, 1997; Hughes et al., 1998). These observations reveal a population of luminous high-redshift infrared galaxies. A unique advantage to studying (sub)mm sources is the near constancy of observed (sub)mm flux with redshift because of the favorable negative k-correction for galaxy spectral energy distributions (SEDs) peaking in the rest frame far-infrared. Therefore, given the flux limits for detection, (sub)mm observations favor the detection of objects resembling extreme versions of the most luminous infrared sources in the local universe, ultraluminous infrared galaxies (ULIRGs) — either powerful, heavily obscured starbursts (with star-formation rates (SFRs) $\sim 10^2 - 10^3 M_{\odot} \text{ yr}^{-1}$) or active galactic nuclei (AGNs). Given their likely high luminosities and the fact that a majority of the submm sources do not appear to be luminous (Compton-thin) AGNs (e.g., Fabian et al., 2000; Bautz et al., 2000; Hornschemeier et al., 2000; Barger et al., 2001a,b; Almaini et al., 2003; Alexander et al., 2003), it is hard to resist the speculation that a substantial fraction of the faint (sub)mm population are massive spheroids in formation (e.g., Sanders, 1999; Frayer et al., 1999; Lilly et al., 1999; Tan, Silk, & Balland, 1999; Lutz et al., 2001; Genzel et al., 2003; Neri et al., 2003). Analysis of the stellar content of spheroids (e.g., Trager et al., 2000a,b) and investigations of the dynamics of merging galaxies hosting powerful starbursts at low redshift (Genzel et al., 2001; Tacconi et al., 2002) suggest diverse formation mechanisms and evolutionary histories for early-type galaxies. If the speculative connection between spheroid formation and the faint submm population turns out to be well-founded, then determining the redshifts, bolometric luminosities, and morphological and spectral properties of a significant number of sources would greatly enhance our understanding of how and when spheroids formed and the relative importance of the mechanisms, monolithic collapse or merging.

A second motivation for investigations in the submm and mm waveband is related to one of the most important topics to date in observational cosmology, the cosmic infrared background (CIB; Partridge & Peebles, 1967). The photometer DIRBE (Diffuse Infrared Background Experiment; Silverberg et al., 1993) and the spectrometer FIRAS (Far Infrared Absolute Spectrometer; Mather, Fixen, & Shafer, 1993; Fixsen et al., 1994; Mather et al., 1999) on board COBE (Cosmic Background Explorer;

¹Submillimetre Common-User Bolometer Array (Holland et al., 1998). SCUBA consists of two arrays, operating at 450 μm and 850 μm , with 91 and 37 bolometer elements, respectively.

Bogges et al., 1992) enabled for the very first time the detection of the CIB (e.g., Puget et al., 1996; Fixsen et al., 1998; Hauser et al., 1998; Schlegel, Finkbeiner, & Davis, 1998; Lagache et al., 1999). The submm shape of the CIB spectrum indicates that infrared galaxies at higher redshift are contributing substantially to this background (Puget et al., 1996; Gispert, Lagache, & Puget, 2000). The amount of energy radiated in the infrared is at least as great as that in the optical (e.g., Hauser & Dwek, 2001; Blain et al., 2002), making it clear that obscured star formation at high redshift contributes significantly to the star formation history of the universe. To resolve the CIB into discrete sources, surveys at different infrared and submm wavelengths with ISO were conducted (e.g., FIRBACK survey; Puget et al., 1999; Lagache & Dole, 2001; Dole et al., 2001) and with SCUBA are still underway. Deep SCUBA imaging down to 0.3 mJy^2 resolves 65 – 95 % of the submm background light at $850 \mu\text{m}$ (Cowie, Barger, & Kneib, 2002).

In order to understand both the individual properties of (sub)mm galaxies and those of the (sub)mm population in the framework of galaxy formation and evolution, the identification of optical/near-infrared/radio counterparts of (sub)mm galaxies is crucial. Identification of (sub)mm galaxies will help to address following open questions:

- What are the the properties of (sub)mm galaxies and their counterparts detected in the optical/near-infrared? How big is the fraction of (sub)mm sources having μJy faint radio counterparts? What is the redshift distribution of the whole population? Are their morphologies mainly merger-like?
- Which object classes contribute to the (sub)mm background? Are mainly extremely red objects (EROs) responsible for the (sub)mm emission? What is the contribution of sources from UV-selected surveys — Lyman Break Galaxies (LBGs)? What is the fraction of sources from NIR-selected surveys — Optical Red Galaxies (ORGs)? Are cold luminous infrared galaxies (LIRGs) contributing the most to the (sub)mm background?
- What is the star-forming history of the universe, and what fraction is obscured? Is the star-formation rate density constant beyond a redshift of $z \sim 1 - 2$?
- Are (sub)mm sources the progenitors of spheroids/ellipticals still in formation? Are these massive systems?

²The confusion limit of SCUBA at $850 \mu\text{m}$ is $\sim 2 \text{ mJy}$, but using massive lensing clusters submm sources below this limit can be detected and investigated.

- What is the connection between spheroid formation and the formation and growth of black holes at high redshift? What is the fraction of luminous AGNs in (sub)mm sources?

1.2 Submm and mm Galaxies

At the beginning of the last decade new technology enabled the building of new, much more sensitive multi-pixel submm/mm instruments (e.g., SCUBA). In 1997, Smail, Ivison, & Blain (1997) reported the first detection of submm sources in a survey of seven clusters by SCUBA (SCUBA Cluster Lens Survey (SCLS); e.g., Smail et al., 2002a). Shortly thereafter, the redshift $z = 2.8$ of the optical counterpart of the submm source SMM J02399–0136 (Ivison et al., 1998) was confirmed by CO interferometry (Frayser et al., 1998). This provided strong evidence that these sources are indeed at high redshift as predicted by Blain & Longair (1993) and cast alternative models, e.g., cold dark dusty gas clouds (Lawrence, 2001), in disfavor.

1.2.1 Why Can (Sub)mm Sources Be Detected?

The peak of the SED of infrared galaxies lies in the far-infrared at a wavelength $\lambda \sim 100 \mu\text{m}$. Dust grains heated by UV photons dominate the far-infrared emission in galaxies. The heating radiation can be due to the diffuse starlight (UV and optical) in the galaxy³, the near-UV photons of a starburst, or radiation from the accretion disk of an AGN. Assuming that the SED peaks at $\sim 100 \mu\text{m}$ in the far-infrared, we observe at $850 \mu\text{m}$ the Rayleigh-Jeans tail of the SED up to a redshift $z \approx 7.5$. The far-infrared SED of a galaxy can be described by a modified blackbody with the emissivity function $\epsilon_\nu \propto \nu^\beta$, a function of the frequency ν , with the emissivity index β (in the range of $1 - 2$) and dust temperature T_d , determining the wavelength of the far-infrared peak. An increase of T_d shifts this peak to shorter wavelengths. The higher the redshift, the shorter is the observed rest-frame wavelength and the closer it lies to the infrared peak. This overcomes the natural dimming of the source caused by the increasing distance and keeps the flux constant over a wide range of redshifts, $z \sim 1 - 10$ (e.g., Blain & Longair, 1993). This negative k-correction makes observations of the (very) high-redshift universe feasible in

³This is known as infrared cirrus emission and first identified in our galaxy by Low et al. (1984).

the submm/mm and an important tool for observational cosmology.⁴ Currently, we detect only the most luminous infrared ($L_{IR} > 10^{12} L_{\odot}$) and thus, the most actively star-forming galaxies⁵ ($\sim 100 - 1000 M_{\odot} \text{ yr}^{-1}$) in the (sub)mm regime. This limitation is set by the sensitivity of the detectors, the coarse telescope beams and the sky background.

1.2.2 Locating and Identifying (Sub)mm Sources

Up to now more than 150 submm and mm sources are detected in different surveys (e.g., Smail, Ivison, & Blain, 1997; Barger et al., 1998; Hughes et al., 1998; Eales et al., 1999; Bertoldi et al., 2000; Scott et al., 2002). But only 11(-12) redshifts confirmed by interferometric CO observations are published so far (Frayser et al., 1998, 1999; Neri et al., 2003; Hainline et al., 2004, T. Greve et al. 2004, in preparation; J.-P. Kneib et al. 2004, in preparation). This number illustrates well that successful identification work is difficult and progress slow. What renders the identification work so complicate? Due to the large (sub)mm beam (full width at half maximum (FWHM) $11''$ at 1.2 mm at the IRAM⁶ 30 m telescope, and $15''$ at $850 \mu\text{m}$ at the James Clerk Maxwell Telescope (JCMT)), the position of a (sub)mm source is uncertain. Ideally, the 1σ position error is $0.5 \times \text{FWHM} \times \text{SNR}^{-1}$ (Fomalont, 1999). Considering that a significant fraction of objects will be found outside the 1σ error radius and allowing for some systematic offsets in the (sub)mm maps, it is more conservative to assume that the true source position is inside the beam radius. Down to the current reachable sensitivities at different wavelengths, the surface density of objects detected in the optical/near-infrared⁷ is much higher than in the submm, and several optical/near-infrared objects typically lie in the (sub)mm beam (e.g., Lilly et al., 1999). It is therefore difficult to identify the source of the dust emission in deep optical/near-infrared images without additional subarcsecond-accurate position measurements. Interferometric techniques are required in order to locate the (sub)mm source securely. Moreover, due to its high redshift and high rest-frame UV/optical extinction, a counterpart is rather faint ($I > 25.0 \text{ mag}$; $K > 21.0 \text{ mag}$) in the observed optical/near-infrared regime, making optical/near-infrared spectroscopic follow-up obser-

⁴Due to luminosity function evolution, the (very) high-redshift universe can also be tackled through radio-/X-ray observations. But these generally detect only powerful AGN at $z > 2$.

⁵Especially for actively star-forming galaxies the infrared luminosity L_{IR} is proportional to the star-formation rate, see e.g., Kennicutt (1998).

⁶Institut de Radioastronomie Millimétrique.

⁷Based on our own data the surface density down to $R \leq 25.0 \text{ mag}$ and $K \leq 20.5 \text{ mag}$ is approximately 55 and 15 sources per square arcmin, respectively.

variations even with 8 m class telescopes challenging.

Currently, there are two millimeter interferometers in the world that are able to tackle the ambitious task of locating the dust emission to subarcsecond accuracy: the Owens Valley Radio Observatory (OVRO)⁸ and the IRAM Plateau de Bure Interferometer (PdBI; Guilloteau et al., 1992)⁹, the latter being more sensitive. Millimeter interferometry locates directly and unambiguously the dust emission. The detection experiment is made at 1.3 mm. Due to purely technical reasons other (sub)mm wavelengths are not yet available for sensitive interferometry.¹⁰ The detection experiment is very time-consuming with current instruments, with tens of hours typically needed for a single object in the small field of view (e.g., PdBI: $\varnothing \sim 25''$ at 1.2 mm).¹¹ Thus, the number of potential identifications is limited. Because of the tight radio/far-infrared relation in star-forming galaxies (e.g., De Jong, Klein, Wielebinski, & Wunderlich, 1985; Helou, Soifer, & Rowan-Robinson, 1985; Condon, 1992), radio interferometry is the next best option, with the advantage that the large VLA primary beam ($\varnothing \sim 30'$ at 1.4 GHz) covers a typical (sub)mm survey field entirely. The radio emission in star-forming regions, star-forming galaxies and infrared galaxies is mainly (non-thermal) synchrotron radiation from relativistic electrons which may be from supernova remnants (SNRs) and (thermal) free-free emission from HII-regions. Whereas the far-infrared emission is generated by dust that is heated through UV photons coming from young, massive stars. The validity of this relation in the local and in the high-redshift universe is shown by Yun, Reddy, & Condon (2001) and Garrett (2002), respectively. Of the brighter (sub)mm sources from present surveys, deep 1.4 GHz VLA maps will detect all but the highest-redshift objects (e.g., Carilli & Yun, 1999, 2000; Barger et al., 2000), where the risk of false associations of (sub)mm and radio sources is modest for the 1.4 GHz source counts at the relevant flux levels of tens of μJy (e.g., Richards, 2000). But it must be mentioned that in recent studies an identification via cm interferometry was sometimes ambiguous due to several μJy faint radio sources falling within the SCUBA beam (e.g., Dunlop et al., 2002; Neri et al.,

⁸OVRO is located 220 miles away from Los Angeles at the edge of the Sierra Nevada at an altitude of 1220 m. Six 10.4 m telescopes make up this mm interferometer. It operates at 1.3 and 2.7 mm.

⁹The PdBI lies at an altitude of 2552m in the French Alps. This mm interferometer consists of six antennas, each having a diameter of 15 m. It operates simultaneously at 1.3 mm (205 – 245 GHz) and 3 mm (82 – 115 GHz).

¹⁰The Submillimeter Array (SMA; Moran, 1998) on Mauna Kea, consisting of eight 6 m antennas, will allow in the near future interferometric observations at 850 μm .

¹¹The ALMA (e.g., Kurz, Guilloteau, & Shaver, 2002) interferometer will need only minutes for locating (sub)mm sources at similar depth.

2003). Thus radio interferometry is a complementary technique to locate submm sources with subarcsecond accuracy.

1.2.3 Redshift Determination

The redshift of a submm source can be determined both through direct spectroscopy and/or indirect methods (photometric redshifts). Spectroscopic redshifts based on submm/far-infrared observations alone cannot be achieved with the current instruments. Thus at the moment, optical/near-infrared spectroscopy is the only way to obtain accurate redshifts. With a future generation of broad-band receivers, CO spectral-line surveys will be possible. Consequently, the method of choice to constrain the redshift distribution is optical/near-infrared spectroscopy for the relatively bright blue sources in the population, combined with photometric redshift estimates for the fainter (in the optical/near-infrared bands) members of the population.

The spectroscopic observation of a securely identified¹² counterpart with $R \lesssim 25$ mag; $K \lesssim 21$ mag is within the reach of an 8 m class telescope, enabling a redshift to be determined. Follow-up detection of a CO line through mm interferometry at the spectroscopic confirmed redshift securely determines the redshift of the (sub)mm galaxy and verifies the targeted object in the optical/near-infrared as the source of submm dust emission. To date (April 2004), only 11(–12) SCUBA galaxies have reliable CO-confirmed redshifts (Frayer et al., 1998, 1999; Neri et al., 2003; Hainline et al., 2004, T. Greve et al. 2004, in preparation; J.-P. Kneib et al. 2004, in preparation).

The difficulty of spectroscopy due to the faintness of most (sub)mm counterparts implies that photometric redshift methods must be employed in order to obtain redshift estimates for significant numbers of submm and mm galaxies. For a small fraction of the submm population, optical/NIR photometric redshift methods can be applied, but their reliability is affected by the dusty/heavily-enshrouded nature of the (sub)mm sources.

Both Carilli & Yun (CY; 1999, 2000) and Dunne, Clements, & Eales (2000b) modeled the 1.4 GHz to 350 GHz spectral index for starburst galaxies as a crude redshift estimator.¹³ Both models use SEDs of low- z star-forming galaxies spanning a wide range of infrared luminosity ($L_{IR} \sim 10^{10} - 10^{12} L_{\odot}$) and take advantage of the opposite

¹²Throughout this thesis, “securely identified” means that the location of the (sub)mm source is accurately determined at a subarcsecond level.

¹³The two redshift indicators differ both in shape and normalization, effects mainly attributed to different sample size and sample selection.

k-corrections in the radio and submm fluxes of luminous infrared galaxies. Due to the scatter in the intrinsic source properties, e.g., infrared luminosity, dust emissivity, dust temperature; due to the use of only two wavelengths; as well as limited sample sizes, this method is inadequate for accurate redshift measurements, especially at $z > 1$. But it does help to distinguish between low- and high-redshift objects, and this indicator shows qualitatively that most mm sources must be at high redshift. Thus it is widely applied in studies of the (sub)mm source population. In case of nondetection in the radio regime or a contamination by AGN contribution, the estimated redshift has to be considered as a lower limit. In the recent years, new photometric redshift methods have been developed. These estimates try to fully include the rest-frame far-infrared part of the SED under the assumption of SEDs similar to local (U)LIRGs (Yun & Carilli, 2002; Wiklind, 2003; Aretxaga et al., 2003).

1.3 Aim of this Thesis

In this thesis, I will report on the follow-up of 1.2 mm sources detected in the MAMBO 1.2 mm survey. This survey is a collaboration between the Max-Planck-Institut für Radioastronomie (MPIfR), the Max-Planck-Institut für extraterrestrische Physik (MPE), and the National Radio Astronomy Observatory (NRAO). Using the MPIfR bolometer array MAMBO (Max-Planck-Millimeter Bolometer Array; Kreysa et al., 1998), we are carrying out at 1.2 mm a deep, wide-area survey on the IRAM 30 m telescope. The aim of the survey is the detection of a significant number of mm sources in several fields, followed by the identification of the counterparts at optical/near-infrared and radio wavelengths. Due to the large beam (10.7") of the IRAM 30 m telescope and the high density of optical/near-infrared sources, it is impossible to make proper source identification using the bolometer data alone. Therefore, to identify and finally characterize the mm sources, we use subarcsecond-accurate mm and cm interferometry in combination with deep optical/near-infrared imaging. The identification of MAMBO mm sources in the NTT Deep Field (NDF; Arnouts et al., 1999) and its flanking fields is the subject of my thesis.

Based on the identification work the primary aims of my thesis are:

- determine the location of the dust emission through the use of the PdBI/VLA,
- identify the optical/near-infrared counterparts of MAMBO 1.2 mm sources,
- determine the redshifts of 1.2 mm sources,
- characterize the global properties of the MAMBO source population,
- compare 1.2 mm and 850 μm surveys with similar depth.

The structure of this thesis is as follows: In chapter (2) I present the data sets obtained to identify and investigate the MAMBO 1.2 mm galaxies. This is followed by chapter (3) where the results of the interferometric identification and the source properties will be discussed. Throughout this thesis, I use J2000 coordinates and I adopt the cosmological parameters: $\Omega_{matter} = 0.3$, $\Omega_{\Lambda} = 0.7$, and $H_0 = 70 \text{ km s}^{-1} \text{ Mpc}^{-1}$.

Chapter 2

OBSERVATIONS AND DATA REDUCTION

2.1 Introduction

The principal aim of the MAMBO 1.2 mm survey is the detection of a significant number of 1.2 mm galaxies. Therefore, the design of the survey is to cover wide fields (each field more than 100 arcmin²) in deep integrations at 1.2 mm (rms down to $\sim 0.5\text{--}1.0$ mJy) with the 37-element Max-Planck-Millimeter Bolometer Array (MAMBO; Kreysa et al., 1998) on the IRAM 30 m telescope. For the more familiar $S_{850\ \mu\text{m}}$ scale the MAMBO survey depth at $S_{1.2\ \text{mm}} \approx 3$ mJy converts to ≈ 8 mJy for $z \sim 3$, but depends on SED and redshift. Thus, its depth is comparable with the UK 8 mJy SCUBA survey (Scott et al., 2002; Fox et al., 2002) at 850 μm but the selection is at a different wavelength. In this SCUBA survey the surface density of sources having a flux $S_{850\ \mu\text{m}} > 8$ mJy is $0.09_{-0.03}^{+0.02}$ arcmin⁻² (Scott et al., 2002). In contrast to the SCUBA bolometers, the MAMBO bolometers¹ operate at 1.2 mm. Given the higher level of water vapor, the conditions at Pico Veleta, the IRAM site, are more appropriate for observations at 1.2 mm than at 850 μm . The telescope performance is expressed in the *noise-equivalent flux density* (NEFD; mJy/\sqrt{Hz}) and depends on the detector-/background-noise, the aperture size and telescope/beam efficiency. For high-redshift (sub)mm galaxies the flux ratio 850 μm /1.2 mm is $\approx 2.5\text{--}3.0$, the telescope performance of SCUBA/MAMBO are $\text{NEFD}_{SCUBA\ 850\ \mu\text{m}} = 90\ \text{mJy}/\sqrt{Hz}$ (Archibald & Coulson, 2000) and $\text{NEFD}_{MAMBO\ 1.2\ \text{mm}} = 39\ \text{mJy}/\sqrt{Hz}$ (Thum, 2004).

¹Recently, a 117-element MAMBO bolometer was installed at the focus of the IRAM 30 m telescope.

To detect a SCUBA 8 mJy source at the same signal-to-noise ratio, a factor of 1.2 – 1.7 more MAMBO observing time is needed. Therefore, the MAMBO survey detects the brighter part of the (sub)mm population. Three fields are covered: the Lockman Hole, Abell 2125, and a region centered on, but larger than, the NTT Deep Field. The former two fields lie in the northern hemisphere, whereas the NTT Deep Field is located in the southern hemisphere. In the following, I will concentrate on the MAMBO survey of the NTT Deep Field and its flanking fields. We selected the area centered on, but larger than, the optical NTT Deep Field for the survey because of the availability of very deep optical/near-infrared multi-color imaging, and the accessibility from IRAM/ESO telescopes. A MAMBO map was obtained for the NTT Deep Field and its flanking fields down to an rms $\sim 0.5 - 1.0$ mJy, (F. Bertoldi et al. 2004, in prep.; see Fig. 2.1). The MAMBO observations of the NTT Deep Field are centered on the well-studied QSO BR1202–0725 (e.g., McMahon et al., 1994; Omont et al., 1996a,b). The bolometer map is a mosaic of individual $240'' \times 200''$ maps obtained in scanning mode, $4''\text{sec}^{-1}$ in altitude and in azimuth. As of early 2002 42 sources were listed in the MAMBO catalog of the NTT Deep Field. The quasar, at redshift $z = 4.69$, coincides with a significant amount of dust emission detected via millimeter observations (McMahon et al., 1994; Omont et al., 1996b). This was the first high-redshift source whose position was accurately located through mm interferometric observations (Omont et al., 1996a). The quasar is by far the brightest object in this map at 1.2 mm with $S_{1.2\text{ mm}} = 14.7 \pm 0.6$ mJy (see Fig. 2.1). This field was chosen because it is not centered on a massive, moderate-redshift cluster that provides amplification by gravitational lensing. The wider field covered by our WFI imaging includes the cluster [VFM98] 114 (Vikhlinin et al., 1998, center $12^h06^m33^s.5 - 07^\circ44'28''$) at a redshift of 0.12. None of the sources from the MAMBO survey is close to this region, however.

A second part of this program is the follow-up and thus, the proper identification of MAMBO 1.2 mm galaxies. Previous work has shown that for a substantial part of the SCUBA source population the counterparts are faint in the optical and/or near-infrared (e.g., Smail et al., 1999). Thus, it is important to gain deep optical and, in particular, deep near-infrared data ($K \sim 21$ mag) for the whole surveyed region. The latter data set is a key element for our identification work. The mm interferometric observations are close in wavelength λ to the mm bolometer ones, but due to the sensitivity of the PdBI only bright MAMBO 1.2 mm galaxies ($S_{1.2\text{ mm}} \geq 3$ mJy) can be observed. Thus,

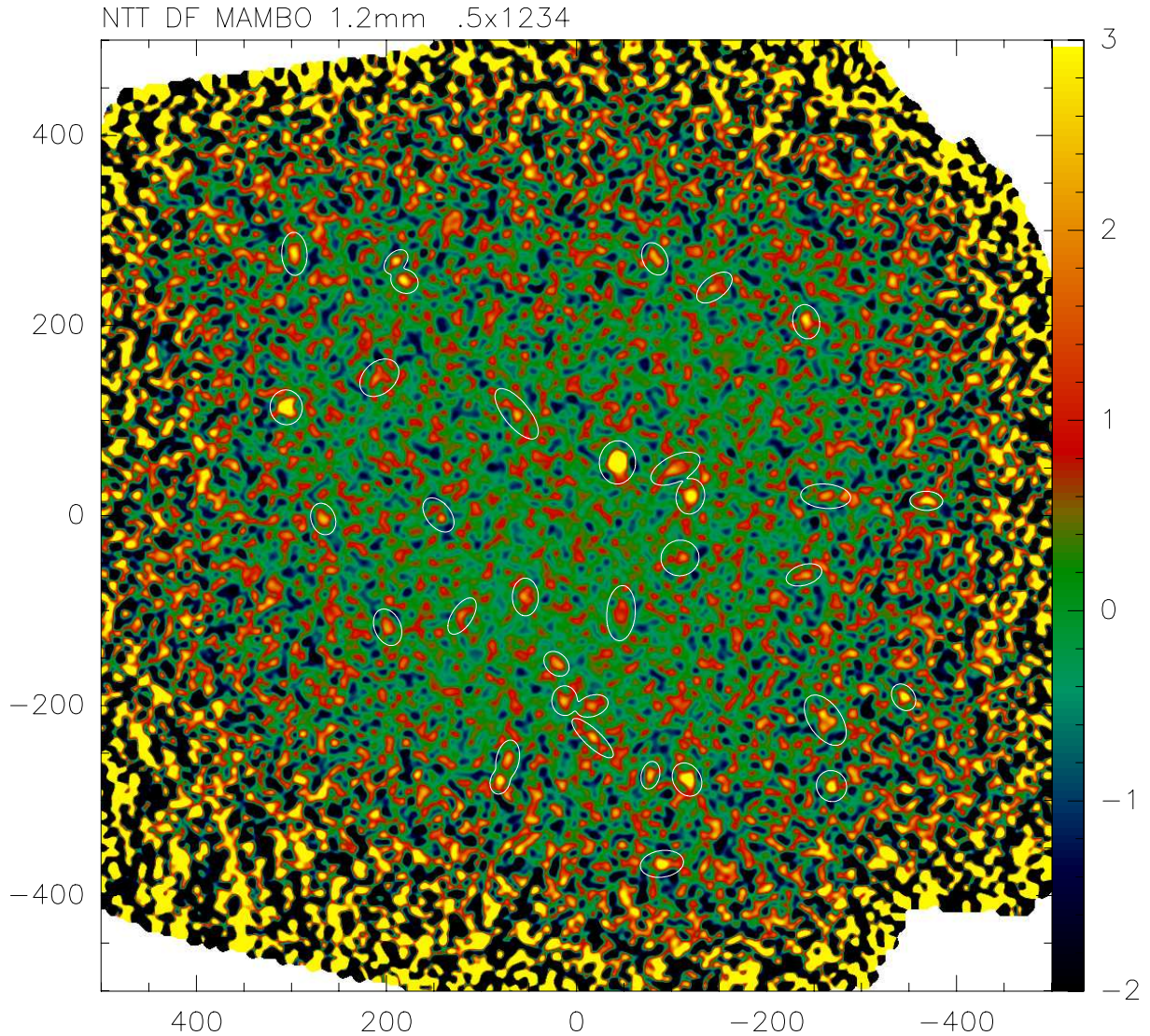


Figure 2.1 The MAMBO 1.2 mm mosaic map centered on the NTT Deep Field. The rms noise level is ≈ 0.5 mJy in the center and increases towards the map edges. The brightest source is the well-known QSO BR1202–0725 at a redshift $z = 4.69$. Approximately thirty sources (encircled) are securely detected (F. Bertoldi et al. 2004, in preparation).

cm interferometry is a complementary element for the secure identification of MAMBO counterparts in the optical/near-infrared (see also § 1.2.2). Furthermore, our follow-up program incorporates photometric observations of individual MAMBO 1.2 mm galaxies without a radio detection, in order to confirm at the 5σ level the fluxes of these sources detected in the MAMBO map at the lower levels ($3-5\sigma$) since its fluxes are uncertain due to systematic problems (errors and non-uniform noise). Finally, we observe suitable

targets at the PdBI to obtain subarcsecond-accurate positions.

The principal goals of the follow-up and therefore this thesis are to identify possible counterparts and to begin assembling spectral energy distributions to constrain the nature and redshift of these objects (for more detail see § 1.3). The identification work is based on the MAMBO catalog as of early 2002. Positions and fluxes measured by MAMBO are presented in § 2.5 and § 3.

The main difference to surveys done in the past by other groups is that this is the first systematic identification study of 1.2 mm-selected sources — with a strong involvement of the PdBI for the subarcsecond-accurate location of the dust emission. Only with the mm interferometer is the dust emission of the (sub)mm source directly detected.

In the following, I will describe the observations and reduction of our multi-wavelength data set as well as the relevant publicly available data. The data set is divided into four categories, (1) optical/near-infrared imaging, (2) mm/cm interferometric data, (3) optical spectroscopy, and (4) pointed mm observations of a subsample of MAMBO 1.2 mm galaxies that were not detected in the radio.

2.2 Optical/Near-Infrared Imaging

The optical/near-infrared imaging has to cover the whole region surveyed by MAMBO with an approximate size of 125 square arcmin. At the beginning of our identification work, near-infrared/optical images of a fraction (4 – 40 %, depending on the wavelength) of the NTT Deep Field were publicly available at ESO.

The near-infrared public data taken at the NTT with the near-infrared imager and spectrograph SOFI cover the inner 20 arcmin² of the MAMBO field down to $J = 23.9$ mag (3σ) and $K_s = 21.9$ mag (3σ) for a 2'' diameter aperture (http://www.eso.org/science/sofi_deep/). The deep optical public data were taken at the NTT with the imager SUSI with 3σ detection limits in a 2'' aperture of $B = 27.2$ mag, $V = 27.0$ mag, $r = 26.7$ mag, and $i = 26.3$ mag, but they span only a 5.3 arcmin² field (Arnouts et al., 1999, ; <http://www.eso.org/science/ndf/>). Finally, VLT science verification data were released in mid-2000 in the z-Gunn Filter (23.7 mag; 3σ) and the interference filter z-special (24.1 mag; 3σ) at 915 nm (http://www.eso.org/science/ut2sv/NDF_release.html) covering an area of ~ 49 square arcmin.

Since the existing publicly available data for the NDF only covered a minor region, we extended this data both in the optical and the near-infrared. We imaged larger fields including the full area covered by MAMBO in B, V, R, and I at the ESO/MPI 2.2 m telescope with the Wide-Field Imager (WFI; Baade et al. (1998, 1999)), in z-Gunn with FORS2 (Seifert et al., 2000) on UT4, and in J/K_s at the ESO NTT with the near-infrared imager/spectrometer SOFI (Moorwood, Cuby, & Lidman, 1998a) and for three PdBI detections with the NIR camera ISAAC (Moorwood et al., 1998b) at the VLT.

In addition, optical/NIR data were taken at the Calar Alto Observatory for the cluster Abell 2125. These data are used here only for identification of one Plateau de Bure detection, MM J154127+6615. Therefore, the description of this data set is rather short but included for completeness.

2.2.1 Optical Data

NTT Deep Field Due to the large size of the MAMBO field, we selected the Wide Field Imaging camera at the 2.2 m MPG/ESO telescope for the optical imaging. It consists of a 4×2 mosaic of 2k×4k CCDs. The field size of the WFI is 34′ × 33′, the pixel scale is 0.238″ pixel⁻¹ and the gap between the CCDs is 7″ horizontal and 23″ vertical. The data were taken during two observing runs in May 2000 and May 2001 within 15 half-nights. Taking into account deep imaging in previous surveys of faint submm sources, we aimed at reaching a 5σ depth of our final images of B ∼ 27 mag, V ∼ 26.5 mag, R ∼ 26.5 mag and I ∼ 25.5 mag. These chosen limits allow the detection of (candidate) counterparts suitable for 8 m class optical spectroscopy, for which the limit is approximately R ≈ 25 mag. In addition, magnitudes in several optical bands can be used to apply photometric methods for redshift estimation of (candidate) optical counterparts in the case where no spectroscopic information can be gained with the current generation of ground-based large-aperture telescopes. In total, we imaged in B, V, R, and I a large field including the full area covered by MAMBO. The WFI field was centered about 5′ from the NDF proper, to avoid a nearby bright star. During the observing care was taken to have for each filter at least several photometric science frames in order to carry out a reliable flux calibration. Dithered exposures were taken. This enables the construction of a superskyflat from the scientific data so that in the final images, no gaps due to the multi-chip nature of the WFI camera are seen.

Due to the large field of view, relatively large size of each file (~ 150 Mb) and their multi-chip nature, reduction of WFI data is time-intensive, disk space-consuming and quite complex. Therefore, we used the GaBoDS (Garching-Bonn Deep Survey; Schirmer et al., 2003, Erben et al. 2004, in preparation) pipeline of the Bonn weak-lensing group of Prof. P. Schneider which was developed for the reduction of WFI data. The WFI pipeline used for our reduction starts with splitting the multiple-chip image into eight single frames, each corresponding to one chip, which is important for the subsequent WFI data reduction. The basic optical image reduction steps (e.g., bias subtraction, flat-fielding) but also subsequent reduction steps are carried out on each single frame. In order to correct for pixel-to-pixel variation, the science frames were divided by normalized flat-fields. The WFI pipeline uses two flatfield types (twilight- and superskyflat). The twilight flat (using the twilight sky as illumination source) is best suited for median-scale variations, whereas the flat constructed from the science frames best represents large-scale variations (Hainaut, priv. comm.; see also Hainaut, West, Smette, & Marsden, 1994; Hainaut, Meech, Boehnhardt, & West, 1998). Science frames to which the twilight flat is applied have a residual sky background of 3 – 4 % (depending on the filter and the brightness of the sky), therefore, these frames were also divided by the normalized superskyflat to reduce the residuals to 1 – 2 %. In addition, an illumination and fringing pattern correction is applied to the science frames and all frames are scaled to the same (highest) gain.

After these steps, an independent astrometric solution for each array in the WFI and each science frame based on the USNO-A1.0 catalog (Monet et al., 1996) is performed. The astrometric calibration and astrometric accuracy are key elements in the reduction of WFI data, which is thus more complex than a standard single-chip-camera reduction. The standard “shift-and-add” method for the co-addition of frames cannot be applied for the whole mosaic because individual chips are tilted with respect to the focal plane, are rotated with respect to each other, and because of the gaps between the chips. Instead, a two-dimensional third-order astrometric solution has to be calculated for every chip and each exposure. To do this, all astronomical objects in each science frame are registered/identified and the distortion polynomial is calculated. Based on this astrometric solution, field-distortion effects — especially critical over the large field of view covered by the WFI — are removed. The co-adding of single frames into the final image is done by using the astrometric solution. The astrometry was accomplished using several hundred

stars from the USNO-A1 catalog spread across the $34' \times 33'$ field of view of the WFI. The rms deviation of USNO-A1 input coordinates from the adopted WFI coordinate solution is $0''.45$.

The WFI pipeline allows the user to interactively exclude images taken under cloudy conditions and/or bad seeing through relative photometric and profile measurements of several hundred stars per frame. In the co-adding procedure the inhomogeneous depth (non-uniform exposure time) of the final image is taken into account. This is caused by chip-dependent read noise and flatfields, and the gaps between the CCDs. To correct these effects, a weighting mask based on a normalized skyflat for each chip and frame is created and applied during the stacking of the science frames to the final image (e.g., see Fig. 5 in Schirmer et al., 2003). The individual weighting map also masks detected cosmic rays, satellite tracks, etc. Due to a wide range in quality of the science frames (diverse seeing and photometric conditions), we examined sub-sets of the data meeting different quality criteria in order to obtain the deepest possible co-added image.

Another critical element of the reduction of wide field imaging data is the relative photometric calibration of each exposure and of the chips between each other. Therefore, we determined the relative zero-points for two overlapping chips and normalized the relative zero-points of photometric images such that the mean is zero. The photometric zero-points for each filter were obtained through observations of broad-band standard stars (Landolt, 1992) for the WFI data taken during photometric conditions. We observed the Selected Area (SA) field SA 104 containing about 15 photometric standard stars spanning a wide range of magnitudes and colors. By averaging over the whole sample of photometric standard stars used, we determined the zero point of each filter of the WFI. In nonphotometric conditions the effective exposure time is not equal to the actual exposure time, and thus, the WFI data taken in nonphotometric conditions has to be tied to that scale. In order to carry out this procedure, the counts of several stars in the final image and the science frames taken under photometric conditions were measured and finally, the effective exposure time per frame and band was determined (real exposure time in parentheses): B = 345 s (500 s), V = 337 s (500 s), R = 294 s (450 s), and I = 297 s (400 s). The 3σ -detection limits of our final images are B = 27.4 mag, V = 26.6 mag, R = 26.2 mag, and I = 25.5 mag in a $2''$ diameter aperture, and the seeing of the final frames is $1.18''$ in B, $1.32''$ in V, $1.06''$ in R, and $0.92''$ in I, see also Tab. 2.1. To check the accuracy of our photometry, the SUSI data of the inner field were compared with our

data in the AB-magnitude system (Oke & Gunn, 1983), see Fig. 2.2. The B- and R-band data agree within 0.1 mag. For the V and the I band possible systematic offsets are detected at a 0.2 mag level. The V-band offset may be explained by the nonphotometric conditions during almost all the V-band observations. In the case of the I band, for the SUSI observation a filter of the Thuan-Gunn system (Thuan & Gunn, 1976) was used, which is different to the WFI I band. This could be responsible for the ~ 0.2 mag offset. In addition, the R-band data were compared with a deep R-band image taken at the VLT during an observing run for the optical spectroscopic follow-up of extremely red objects (EROs) and the photometric uncertainty is less than ± 0.1 mag (Lehnert, priv. comm.).

Recently, on the nights of April 6 and 7, 2003, deep z-band observations were carried out in “service mode” using the imaging spectrograph FORS2 on UT4 of the VLT. Conditions were photometric throughout the observations and the seeing was typically about $0.5''$. The field size of FORS2 is $6.8' \times 6.8'$. Therefore, to cover the whole surveyed MAMBO region (the K-band field) four separate pointings were selected. The data were taken as a sequence of dithered exposures with a net integration time of 1 hour for each pointing. The images were processed in the standard way but were flat-fielded using images generated by masking out all objects with surface brightnesses with 1 sigma of the background noise and then combined by taking the pixel median of all the frames without the images being aligned. Then, this flat-field frame was normalized to one and divided into each z-band image. The final calibration was determined through observations of the spectrophotometric standard LTT7987 (Hamuy et al. 1994) for the z-band filter. However, given the very sensitive red response of the FORS2 array, the z-band filter was calibrated by integrating the spectral energy distribution of LTT7987 (Hamuy et al., 1994) and of BD+17 4708 (Oke & Gunn, 1983), which is the absolute flux calibrator for the Gunn-z filter (Schneider et al., 1983). In making these estimates, both the response of the CCD and the filter transmission (both of which are available on the ESO web sites) were considered. The average noise across the frame is such that the 3σ detection limit in a $2''$ diameter aperture is $z_{BD+174708} = 26.38$ mag. The absolute flux distribution of LTT7987 provides a direct calibration of the images in the AB-magnitude system (Oke & Gunn, 1983) which yields $z_{AB} = z_{BD+174708} - 0.30$ mag.

Abell 2125 In March/April 2000 an observing run was conducted at Calar Alto in order to obtain imaging data for a part of the Abell 2125 field observed by MAMBO. Optical imaging was performed with the imager and spectrograph CAFOS (Meisenheimer, 1998). The diameter of the field of view is $16'$ and the pixel scale is $0.5'' \text{ pixel}^{-1}$. The cluster field was imaged in the R band in one pointing. The individual science frames were taken in dithering mode enabling the creation of a superskyflat. The science frames were bias-subtracted and flatfielded by the superskyflat constructed from the science images. Then they were combined and aligned to a final image. Photometric calibration was done similarly to that of the WFI data reduction. The detection limit is $R = 25 \text{ mag}$ (3σ). An astrometric solution was determined using several USNO-A1 stars in the field of view.

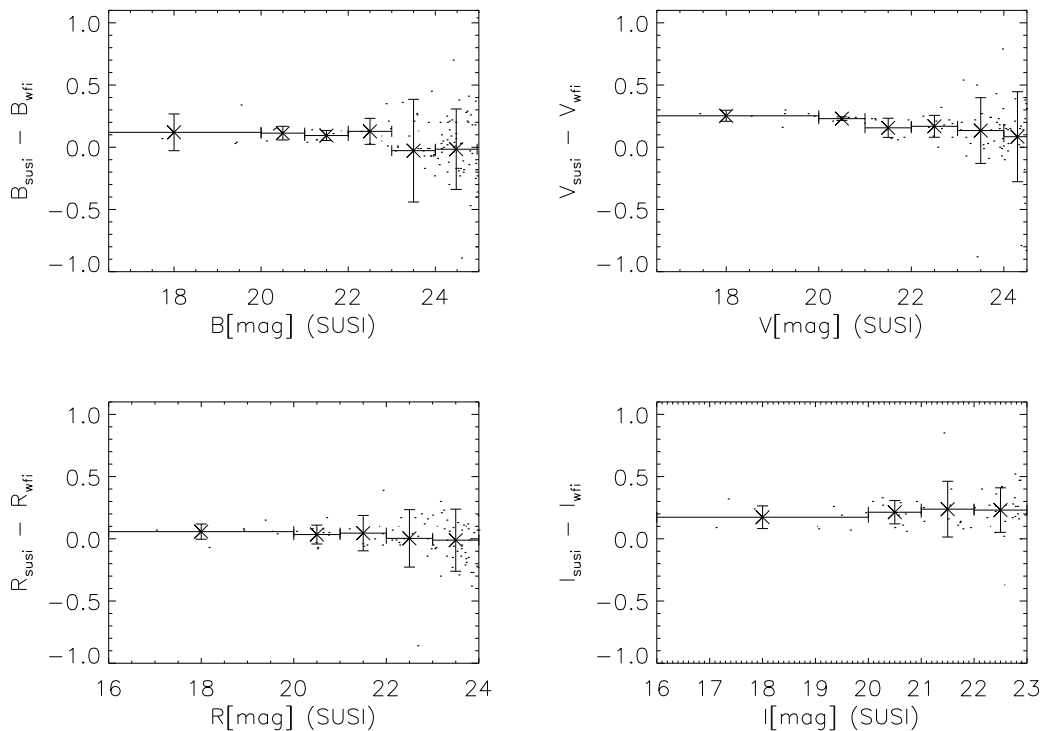


Figure 2.2 Comparison of the ESO SUSI data (<http://www.eso.org/science/ndf/>; Arnouts et al., 1999) and our WFI data. In each panel, the deviation between the magnitude (AB-system (Oke & Gunn, 1983)) of an astronomical object — both point and extended sources are used for this analysis — in the SUSI and the WFI frame is plotted versus the magnitude in the SUSI frame. For each magnitude bin the average deviation and the uncertainty is shown. Possible systematic offsets in the V and I band are detected.

2.2.2 NIR-Data

NTT Deep Field K_s -band observations were undertaken at the ESO NTT with the near-infrared imager/spectrometer SOFI in three nights in March 2001. All three nights were photometric with a seeing below $0.8''$ in the near-infrared. The pixel scale is $0.290'' \text{ pixel}^{-1}$ and the field size for individual SOFI frames is $4.9' \times 4.9'$. To cover the whole region surveyed by MAMBO we placed eight contiguous SOFI fields around the public K_s image to cover a total field of $13'3 \times 13'0$. SOFI frames were dithered between exposures using a dither box of $30''$. This procedure is important for the later subtraction of the sky background in the science frames. The near-infrared data were reduced using IRAF and the ECLIPSE package developed for reduction of ISAAC/SOFI data (Devillard, 1997), and followed the standard reduction steps for near-infrared imaging data. The SOFI field distortion, an effect that is especially important in the corners of the field of view in each individual science frame was corrected. This was done using observations of the globular cluster M 10 which were kindly provided by the ESO NTT team. To carry out this procedure, the whole SOFI field has to be covered by astronomical objects for which the astronomical position is known into the milliarcsecond range — objects observed by the astronomical satellite Hipparcos (van Leeuwen, 1996; Turon, 1999) are suitable for this, and globular clusters are among the best candidates to undertake this experiment. The position of the individual cluster members were obtained from the Hipparcos catalog (e.g., Turon et al., 1995) and a distortion matrix was determined. This matrix was applied to each individual reduced NDF science frame. Then, for each of the eight fields a final image was created.

Finally, the aim was to create a K-band mosaic based on the nine fields. To do this correctly, the ideal case is to use an image where the astrometric solution is well-known and accurate. For this alignment procedure and a final distortion correction, the optical WFI data were used. Thus, the K-band images were aligned, residual distortions corrected, and rescaled to match the final optical WFI images, using the relative positions of about 100 sources per final K-band combined image (of which there were nine, surrounding and including the public NDF K-band image). Any systematic offsets are much less than one pixel or $\sim 0.2''$. Furthermore, we determined the systematic offset between the radio and the optical frames. This was done by comparing the K-band (tied to USNO-A1 through the WFI images) and VLA frames using 33 well-detected VLA sources ($\geq 4.5\sigma$) that had

K-band counterparts down to $K_s = 21.9$ mag within the likely positional uncertainty of each VLA source (adopting as uncertainty the larger of $1''$ and $3 \times \text{FWHM}/(2 \times \text{S/N})$; Fomalont, 1999). The mean difference between the near-infrared and VLA position is $0''.19 \pm 0''.07$ in RA and $0''.23 \pm 0''.05$ in DEC. Due to a high flux limit for the VLA sources ($\geq 4.5\sigma$) these errors are small.

The photometric zero-point was obtained through observations of the NICMOS standard stars (Persson et al., 1998) for the K_s images taken with SOFI during photometric conditions. Due to the fact that on all three observing nights conditions were photometric, no scale correction had to be applied. To assure a correct photometric solution for all 9 fields, a photometric analysis was performed. It comprised two steps: (1) measuring the photometric uncertainty between individual, contiguous fields, and (2) comparing our photometry with publicly available data. The deviation between our contiguous fields is ± 0.1 mag. This uncertainty is consistent with expectations for NIR-observations due to the changing atmosphere. Then, we compared our data with publicly available ones. We find a significant deviation of ≈ 0.5 mag between the public ESO central field and our fields. Using the Two Micron All Sky Survey (2MASS; see <http://www.ipac.caltech.edu/2mass/>), we compared the photometry for the public ESO central field and for our fields with the 2MASS data. Down to $K \sim 15.1$ mag, the 2MASS magnitudes are reliable within < 0.1 mag. The agreement between our data and the 2MASS is within ± 0.1 mag and again, we detected a deviation between the ESO data and the 2MASS at ≈ 0.5 mag in the same direction. Therefore, we corrected the magnitudes in the central field by -0.5 mag. The detection limits of the nine SOFI fields are between $K_s = 21.9 - 22.0$ mag. Thus, we assumed for the whole K-band mosaic a detection limit of 21.9 mag for our source catalog and analysis.

None of the three PdBI-detected MAMBO galaxies in the NDF has a K-band counterpart down to the SOFI limit (see § 3.1 for a detailed discussion of the identification of the PdBI detections.). Therefore, targeted ultra-deep K-band ($K_s \sim 22.7$ mag in a $1.5''$ aperture) observations at the VLT with the near-infrared imager and spectrograph ISAAC of these blank fields were carried out in April 2002 during one night in excellent photometric and seeing ($\sim 0.3'' - 0.4''$) conditions. The pixel scale is $0.148'' \text{ pixel}^{-1}$ and the field of view is $2.5' \times 2.5'$. Due to the small field size and the low surface density of mm galaxies, one pointing per source for 1-2 hours was performed. The data reduction was done in a similar way to that described above. The three VLT images were aligned on

the K-band mosaic. The detection limit in a $1.5''$ aperture is ≈ 22.7 mag. The data were used to revise the SOFI photometry. The SOFI (using our calibration) and the ISAAC data sets agree within 0.1 mag (Lehnert, priv. comm.).

Between March 14 and 16, 2003, J-band imaging was obtained with SOFI at the ESO-NTT. Similar to the K_s -band observations, eight contiguous fields around the public central field were observed at the same pixel scale and field of view. The data reduction and the construction of the $13.3' \times 13.0'$ mosaic was done as for that in the K band. The photometric calibration of the J-band mosaic was performed by using 2MASS observations of the NTT Deep Field. The detection limit at a 3σ level is 24.0 mag for a $2''$ aperture.

Abell 2125 During the 2000 Calar Alto observing run K' data were taken with the near-infrared imager OMEGA Prime (Thompson & Bizenberger, 1999) at the 3.5 m telescope. Due to bad weather conditions, we observed only the inner part of the Abell 2125 field ($\sim 6' \times 6'$) down to 21.2 mag at a 5σ level. The data reduction was performed as described above. A distortion matrix was not created since no suitable data for this procedure were available. By observing near-infrared standard stars (Persson et al., 1998) under photometric conditions, the photometric zero-point was determined. The majority of the K' science frames were taken under nonphotometric conditions, and thus, the calculated photometric zero-point was tied to this scale. The astrometry of the final image was performed by using several of the USNO-A1 stars lying in the observed field.

2.2.3 Combination of the Imaging Data Sets of the NTT Deep Field

The source detection and extraction is done using the astronomical software *SExtractor* (Sources Extractor; Bertin & Arnouts, 1996) of a noise-scaled co-addition of the BVRIzJK images. *SExtractor* provides a wide variety of parameters for optimizing detection of astronomical sources in images (e.g., number of contiguous pixels, detection threshold, seeing, zero-point). In Fig. 2.3, the setup applied for the source extraction is presented. The quality of the catalog, i.e. its robustness and completeness is tested manually by varying the important source extraction parameters like DETECT_MINAREA, DETECT_TRESH, DEBLEND_NTHRESH and by a visual inspection of the source catalog output, especially the surrounding of the MAMBO 1.2 mm sources. Fig. 2.4 illustrates

the source extraction performed by *SExtractor* based on our setup presented in Fig. 2.3. A major part of the visual inspection of our source detections — checking for completeness — is achieved by blinking these two panels. In addition, source counts in different bands and for different source populations e.g., extremely red objects or optical red galaxies, were compared with the literature and agreed within expected uncertainties. We aimed

```

# Default configuration file for SExtractor V1.2b14 -> 2.0
# EB 23/07/98
# (*) indicates parameters which can be omitted from this config file.

#----- Catalog -----
CATALOG_NAME      NTDF_K_mc.cat # name of the output catalog
CATALOG_TYPE      ascii # "NONE", "ASCII_HEAD", "ASCII", "FITS_1.0"
                   # or "FITS_LDAC"
PARAMETERS_NAME   default.param # name of the file containing catalog contents

#----- Extraction -----
DETECT_TYPE       CCD # "CCD" or "PHOTO" (*)
FLAG_IMAGE        flag.fits # filename for an input FLAG-image
DETECT_MINAREA    10 # minimum number of pixels above threshold
DETECT_THRESH     1.0 # <sigmas> or <threshold>, <ZP> in mag.arcsec-2
ANALYSIS_THRESH   1.0 # <sigmas> or <threshold>, <ZP> in mag.arcsec-2

FILTER            Y # apply filter for detection ("Y" or "N")?
FILTER_NAME       gauss_3.0_5x5.conv # name of the file containing the filter

DEBLEND_NTHRESH   32 # Number of deblending sub-thresholds
DEBLEND_MINCONT   0 # Minimum contrast parameter for deblending

CLEAN             Y # Clean spurious detections? (Y or N)?
CLEAN_PARAM       1.0 # Cleaning efficiency

MASK_TYPE         NONE # type of detection MASKing: can be one of
                   # "NONE", "BLANK" or "CORRECT"

#----- Photometry -----
PHOT_APERTURES    9 # MAG_APER aperture diameter(s) in pixels
PHOT_AUTOPARAMS   2.5, 3.5 # MAG_AUTO parameters: <Kron_factor>, <min_radius>
SATUR_LEVEL       50000.0 # level (in ADUs) at which arises saturation
MAG_ZEROPoint    22.17 # magnitude zero-point
MAG_GAMMA         4.0 # gamma of emulsion (for photographic scans)
GAIN              0.0 # detector gain in e-/ADU.
PIXEL_SCALE       0 # size of pixel in arcsec (0=use FITS WCS info).

#----- Star/Galaxy Separation -----
SEEING_FWHM       0.98 # stellar FWHM in arcsec
STARNNW_NAME      /opt/seextractor2.1.6/config/default.nnw # Neural-Network_Weight table filename

#----- Background -----
BACK_SIZE         64 # Background mesh: <size> or <width>,<height>
BACK_FILTERSIZE   3 # Background filter: <size> or <width>,<height>
BACKPHOTO_TYPE    LOCAL # can be "GLOBAL" or "LOCAL" (*)
BACKPHOTO_THICK   24 # thickness of the background LOCAL annulus (*)

#----- Check Image -----
CHECKIMAGE_TYPE    APERTURES # can be one of "NONE", "BACKGROUND",
                   # "MINIBACKGROUND", "-BACKGROUND", "OBJECTS",
                   # "-OBJECTS", "SEGMENTATION", "APERTURES",
                   # or "FILTERED" (*)
CHECKIMAGE_NAME    check_Kalign_mc.fits # Filename for the check-image (*)

#----- Memory (change with caution!) -----
MEMORY_OBJSTACK   2000 # number of objects in stack
MEMORY_PIXSTACK   100000 # number of pixels in stack
MEMORY_BUF_SIZE    1024 # number of lines in buffer

#----- Miscellaneous -----
VERBOSE_TYPE      NORMAL # can be "QUIET", "NORMAL" or "FULL" (*)

#----- New Stuff -----

```

Figure 2.3 Example of the setup applied for the extraction of objects with *SExtractor* in the K_s band.

to detect sources with a minimum number of pixels (10 pixels in our case, at least as large as the seeing disk with each pixel 1σ above the local background) down to a detection limit of 3σ . The individual parameters were adjusted until this goal was achieved. The magnitude is determined in a $2''$ wide aperture (MAG_APER). Due to the seeing of the final images ($\sim 1''$), the chosen aperture size is appropriate for faint galaxy photometry.

The source position is determined from the multi-color image. Wavelength-dependent morphology can lead to small offsets of the peaks in certain bands from these average positions. Thus, we measure the magnitude or upper limit for each source in the individual bands on the previously determined position. Finally, the individual catalogs are combined into one. We excluded sources from this catalog classified to be stars by *SExtractor* (CLASS_STAR). This catalog contains more than 14000 sources and is used for all following data analysis. In Tab. 2.1, an overview of our multi-wavelength data set described in the subsections before is given.

The estimate of the astrometric uncertainty is crucial given the high density of faint potential counterparts to mm sources. Both the PdBI and VLA positions are obtained in the radio reference frame. The positions of the PdBI and VLA detections for

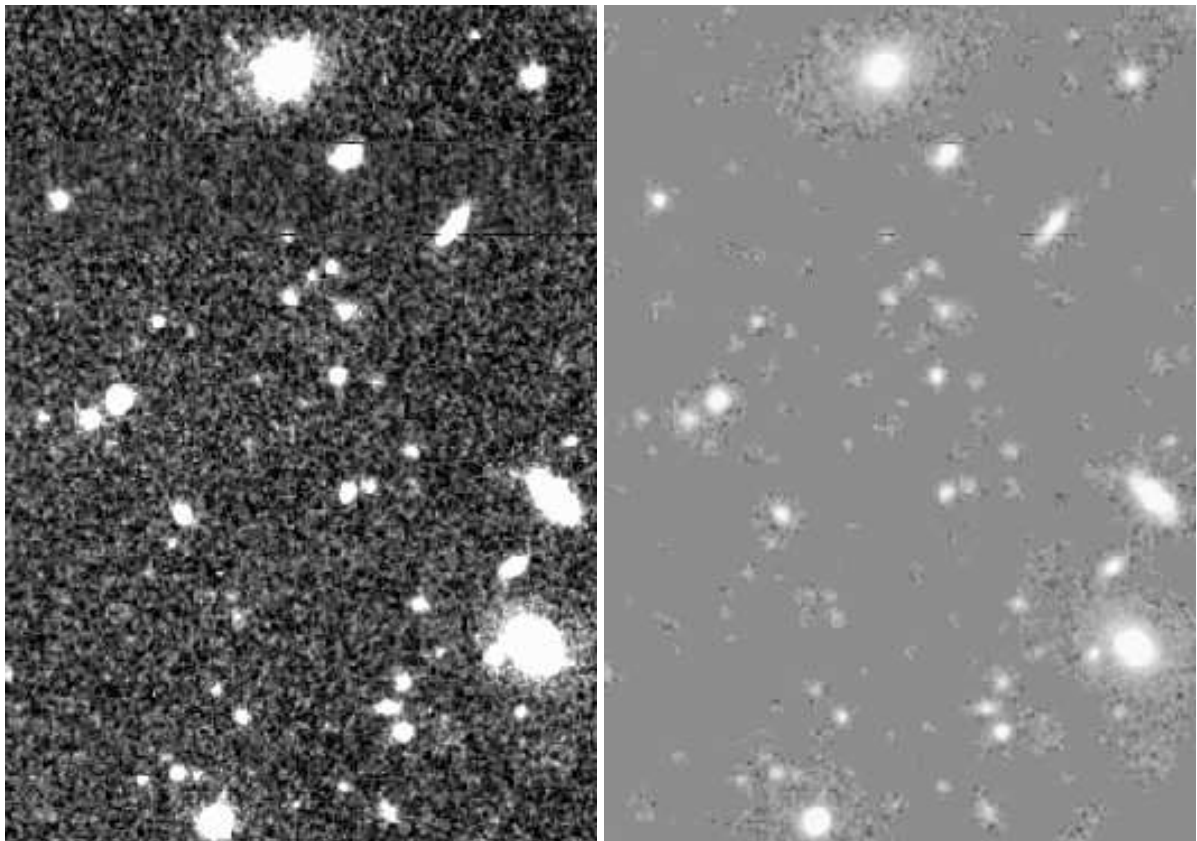


Figure 2.4 *Left Panel:* Part of the NTT Deep Field in the K band. *Right Panel:* Objects and its local background extracted by *SExtractor* in the part of the NDF displayed in the left panel using the setup presented in Fig. 2.3.

Table 2.1. Summary of the multi-wavelength follow-up observations of the NDF

Band (1)	Field Size (2)	det. Limit (3)	Seeing (4)	Instrument (5)	Comment (6)
m_B	$34' \times 33'$	27.4 mag	$1.18''$	WFI	
m_V	$34' \times 33'$	26.6 mag	$1.32''$	WFI	
m_R	$34' \times 33'$	26.2 mag	$1.06''$	WFI	
m_I	$34' \times 33'$	25.5 mag	$0.92''$	WFI	
m_z	$13.3' \times 13.0'$	26.4^\dagger mag	$0.50''$	FORS2	
m_J	$13.3' \times 13.0'$	24.0 mag	$0.80''$	SOFI	central field public data (ESO)
m_{K_s}	$13.3' \times 13.0'$	21.9 mag	$0.98''$	SOFI	central field public data (ESO)
m_{K_s}	3 fields a $2.5' \times 2.5'$	22.7^* mag	$0.30\text{--}0.40''$	ISAAC	pointing on PdBI detections
$S_{1.2mm}$	~ 125 sq. arcmin	1.5–3.0 mJy		MAMBO	
$S_{1.26mm}$	4 fields a $25'' \times 25''$	1.5–3.6 mJy		PdBI	four PdBI observations
$S_{1.4GHz}$	$\sim \emptyset 32'$	$39 \mu\text{Jy}$		VLA	

Note. — Col. (1) — Band in which flux is measured.

Col. (2) — Field size.

Col. (3) — Optical/near-IR magnitudes were measured except for the ISAAC imaging in a $2''$ diameter aperture, and are except for the z band on the ‘Vega’ system. \dagger : For the z band, we performed the photometric measurements in the BD+17 4708 system. $*$: For the ISAAC imaging, we used a $1.5''$ diameter aperture. Both optical/near-IR and radio/mm limits are 3σ .

Col. (4) — Seeing.

Col. (5) — Name of instrument.

Col. (6) — Comments.

MM J120546–0741.5, MM J120539–0745.4 and MM J154127+6615 (Table 2.2 and Bertoldi et al. (2000)) are consistent within their errors which are $0.4''\text{--}0.5''$ for PdBI, and $\sim 1''$ for the large-beam VLA data of these faint sources. The systematic errors contribute significantly to the PdBI uncertainty in the cases of MM J120517–0743.1 and J154127+6615 (e.g., Downes et al., 1999), whereas random errors are the most important source of uncertainty in the 1.4 GHz positions. The mean offset between the near-infrared and the VLA frame is $0''.19 \pm 0''.07$ in RA and $0''.23 \pm 0''.05$ in DEC (see § 2.2.2 for more detail). Optical/near-infrared positions used below have been corrected for the small systematic offset, i.e. they should be in the radio coordinate system to a good approximation.

In order to estimate the uncertainty of measured offsets between PdBI positions and near-infrared/optical objects, we have to take several possible uncertainties into account. Due to the phase calibration of the mm frame based on bright radio calibrators, we assume that there is no systematic offset between these two frames. Thus, we conclude that the differences between the VLA and PdBI positions are consistent with the relatively low S/N of the VLA detections. The uncertainty between the radio and the optical/near-infrared frames consists of the systematic offset between the radio and the optical/near-infrared frames and the random uncertainties both of the radio and optical/near-infrared positions. Thus, the total error is dominated by the random errors of the individual measurements and is typically $< 1''$.

2.3 Interferometry

To obtain subarcsecond-accurate positions — the key element of the identification work — we carried out observations both at the Plateau de Bure mm interferometer and the Very Large Array cm interferometer.

2.3.1 1.2 mm Interferometry

At the time of proposing a PdBI follow-up (September 2000), neither radio interferometric nor MAMBO mm photometric mode observations were available to select targets for mm interferometry. Therefore, the PdBI source selection was only based on the bolometer map and on optical/NIR information. We considered only sources for which inspection of the partial data set shows the MAMBO detection to be reliable and proposed to observe interesting and/or peculiar mm sources selected from the cluster Abell 2125 and the NDF. Five sources were observed, four being in the NDF and one in the field of Abell 2125, the securely radio-identified source J151427+6615 (Bertoldi et al., 2000). These are some of the brightest sources in the MAMBO bolometer mm map. The observations were carried out with the PdBI in winter 2000/2001 in order to determinate absolute source positions, test for possible multiplicity or spatial extent, and confirm the MAMBO fluxes. The observations were performed in the 5D configuration, with the receivers tuned to 238.46 GHz. The phase center was at the nominal MAMBO bolometer position and we integrated between nine and 38 hours per source, reaching an rms of

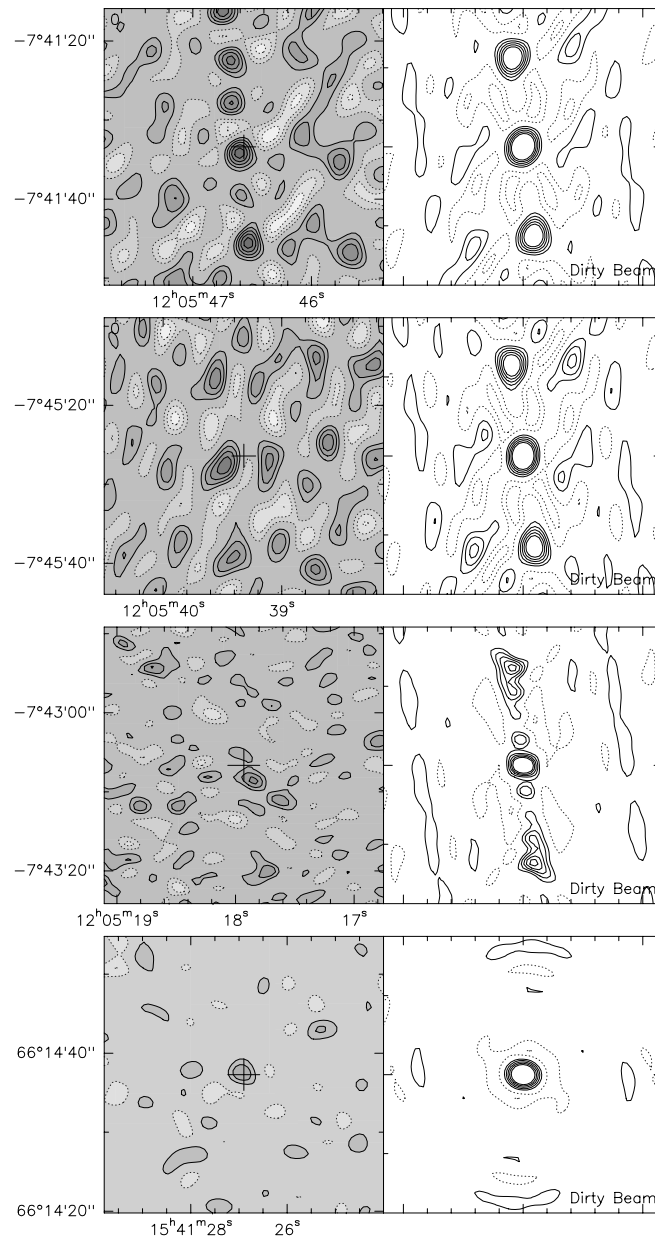


Figure 2.5 “Dirty” 1.26 mm interferometric maps for the four PdBI detections. From top to bottom: MM J120546–0741.5, MM J120539–0745.4, MM J120517–0743.1, and MM J154127+6615. Each image is $35'' \times 35''$ and oriented such that north is at the top and east is to the left. The plus indicates the phase center, placed at the position of the mm source originally estimated from the bolometer map. The contour levels are spaced by 1 mJy and the solid and dotted lines represent positive and negative contours respectively. The dirty beams are shown to the right, where the three NDF sources show considerable side lobes because of their equatorial declination. The beam profiles for these three sources are similar because of the similar declination and UV coverage.

Table 2.2. PdBI positions and fluxes of the five MAMBO 1.2 mm galaxies

Object (1)	Obs. Time (2)	RA (J2000) (3)	DEC (J2000) (4)	Flux (5)
MM J120546–0741.5	9	12 ^h 05 ^m 46 ^s .59±0 ^s .02	−07°41′34″.3±0″.37	6.1±1.2
MM J120539–0745.4	14	12 ^h 05 ^m 39 ^s .47±0 ^s .02	−07°45′27″.0±0″.33	6.4±1.0
MM J120517–0743.1	38	12 ^h 05 ^m 17 ^s .86±0 ^s .02	−07°43′08″.5±0″.24	2.6±0.5
MM J120518–0742.6	30	-	-	<1.9 (3 σ)
J154127+6615	20	15 ^h 41 ^m 26 ^s .96±0 ^s .02	66°14′37″.62±0″.20	3.2±0.5

Note. — Col (2) — Units of observing time are hours. Col. (3) — Units of right ascension are hours, minutes and seconds. Col. (4) — Units of declination are degrees, arcminutes, and arcseconds. Col. (5) — Units of flux are mJy.

0.5 – 1.2 mJy. We used 3C273, 1124–186, 1637+574 and 1458+718 to calibrate the temporal variation of amplitude and phase. 3C273, 3C345, 3C454.4 were used to calibrate the IF bandpass. The absolute flux scale was determined with observations of MWC349, CRL618 and 3C273, and has an uncertainty of $\sim 20\%$. We calibrated and reduced the data at IRAM, Grenoble using the GAG software packages CLIC and GRAPHIC. The final naturally weighted dirty maps are shown in Fig. 2.5 along with the dirty beams. The FWHM of the beam for MM J120546–0741.5 is $3.4'' \times 2.8''$ with PA = -21° at 1.26 mm; beams for the other NDF sources are similar. The beam for the Abell 2125 source is $3.0'' \times 2.5''$ with PA = 84° at 1.26 mm.

Four sources are detected at the $> 5\sigma$ level. We derived the positions and total 1.26 mm flux densities listed in Table 2.2 from point-source fits to the calibrated visibilities in the UV plane. The positional accuracy quoted in Table 2.2 is the sum in quadrature of the statistical error of the point source fit with an astrometric systematic uncertainty of $0.2''$ (e.g., Downes et al., 1999). The signal-to-noise ratio of our data does not enable us to put strong constraints on the source size at 1.26 mm. No detection is resolved in our $\sim 3''$ beam data, however. The PdBI map of MM J120546–0741.5 suggests a possible second source near $12^h05^m46^s.7 - 7^\circ41'28''$ but its significance is only $\sim 3 - 4\sigma$ and no additional supporting evidence is given by a radio or optical/NIR counterpart. Observations at 95 GHz (3.16 mm) were obtained in parallel. None of the sources is detected at this frequency, consistent with dust emission. The only nondetection was the source

MM J120518–0742.6 where no tentative signal was detected after 30 hours of observations on the nominal bolometer map position at $12^h05^m18^s.7 - 7^\circ42'39''.7$.

2.3.2 1.4 GHz Interferometry

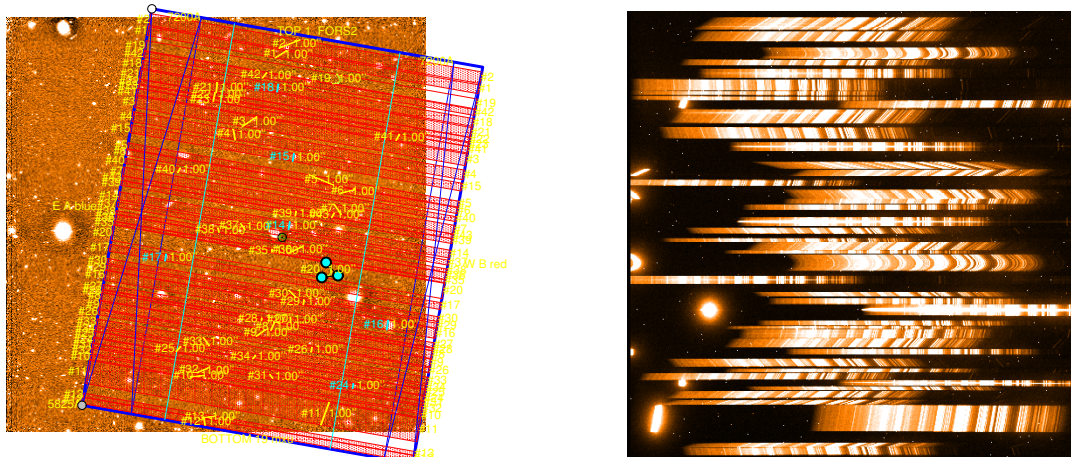
The NTT Deep Field was observed at 1.4 GHz with the VLA in April and May, 2001, for 15 hours in the B configuration (10 km maximum baseline). Standard wide-field imaging mode was employed (50 MHz total bandwidth with two polarizations and 16 spectral channels). The source 3C 286 was used for absolute gain calibration and 1224+035 was used for phase and bandpass calibration. The data were also self-calibrated using sources in the NDF itself. Images were synthesized and deconvolved using the wide-field imaging capabilities in the AIPS task IMAGR, and the primary beam correction was applied to the final image. The FWHM of the Gaussian CLEAN beam was $7'' \times 5''$ with a PA = 0° . The rms noise in the final image is between 13 and 15 μJy over the $15' \times 15'$ region covered by MAMBO. The variation of the rms noise of the map was not only caused by the usual beam attenuation and UV plane coverage, but was also due to residual calibration errors because of a relatively large number of bright sources (2 sources of $\gtrsim 60$ mJy/beam) and one spatial grouping of fainter but still relatively bright sources to the northeast of the center of the map. These residual calibration errors manifested themselves as uneven noise in a series of stripes in the final map. About one-third of area of the final VLA map was affected by this striping. We describe in § 3.2.1 how this was dealt with in identifying radio counterparts to the MAMBO 1.2 mm detections. A catalog for the whole observed NDF at 1.4 GHz down to $\geq 5\sigma$ (66 μJy) was generated with AIPS.

2.4 Spectroscopy

For the central part ($7' \times 7'$) of the NDF where deep z-band imaging data were available in the VLT public archive, we carried out multi-object spectroscopy. Unfortunately, at the time of the observing run no radio map of the NTT Deep Field was available. Therefore, our aim was to observe all z-band candidate counterparts within the MAMBO beam of all the MAMBO 1.2 mm galaxies and to detect emission lines ($\text{Ly}\alpha$, [OII], $\text{H}\beta$, [OIII] and $\text{H}\alpha$) in order to determine the redshifts of the observed objects. The obser-

vations were carried out on two nights in April 2001 at the VLT Kueyen using FORS2 and its mask-exchange unit (MXU; Schink et al., 2000). By using the low-resolution grism GRIS-150I in combination with the blocking filter GG435, we covered the spectral range $4450 \text{ \AA} - 8800 \text{ \AA}$. Based on the strongest emission lines ($\text{Ly}\alpha$, $[\text{OII}]$, $\text{H}\beta$, $[\text{OIII}]$ and $\text{H}\alpha$), this spectroscopic window covers a redshift range from $z = 0 - 1.3$ and $z = 2.6 - 6.2$. Unfortunately, there is a region between $z = 1.3$ and $z = 2.6$ where none of these lines would be detected in our observing window. But observed spectroscopic redshifts of counterparts of SCUBA galaxies demonstrated that a non-negligible part of this population has redshifts lying in our observed redshift range (e.g., Soucail et al., 1999; Ivison et al., 2000a; Ledlow et al., 2002; Chapman, Blain, Ivison, & Smail, 2003b). We observed four masks, and the total integration time was three hours for each mask. The observing conditions were mostly photometric and the seeing varied between $\sim 0.6'' - 0.8''$. Up to 90 slits can be put in one mask. Based on the z-band image, the mask layout was designed with the FORS Instrumental Mask Simulator (*FIMS*; <http://www.eso.org/observing/p2pp/OSS/FIMS/FIMS-tool.html>). As the masks are cut by a laser, not only straight slits can be used. In addition, inclined and curved slits can be designed which allows greater flexibility to observe more than one object at the same time. The slit width was $1''$ and the length varied between $\sim 3''$ and $\sim 20''$. Due to the absence of a radio map, all candidate z-band counterparts within the MAMBO beam were observed and where it was possible, sources adjacent to the MAMBO beam were observed as well. In the meantime since the observing run, new bolometer data were acquired and a new NDF MAMBO source catalog was constructed. A few sources were removed from the old catalog and several new sources were extracted from the new MAMBO bolometer map. Therefore, only 14 of the 18 MAMBO mm galaxies lying within this field were observed. Included in this sample are mm sources that were identified through radio interferometry, MM J120526-0746.6, MM J120522-0745.1 and MM J120530-0741.6, and have faint optical counterparts ($z = 25.1, 23.6$ and 25.7 mag, respectively). Due to the low surface density of MAMBO mm sources, large parts of the masks are not filled up by slits. Therefore, we put these extra slits on objects either having an interesting morphology e.g., edge-on galaxies or galaxies with extreme z-k colors ($z-K > 3$). There were 33 to 51 slits in each of our masks (see Fig. 2.6), for a total of 158 slits covering 242 astronomical objects in the four masks.

The data reduction was performed using IRAF. Due to the variety of slit shapes and



(a) Mask1 overlaid on the z-Gunn Image of the NTT Deep Field.

(b) Two-dimensional spectra of Mask-1.

Figure 2.6 MXU Mask-1.

orientations e.g., parallelograms, the dithering technique could not be applied during the observations. The integration time per frame was 20 to 30 minutes. Each science frame was bias-subtracted. Then, each two-dimensional spectrum was cut out from the science frames and individually reduced. Based on wavelength calibration data, each spectrum (spectroscopic flatfield, science frame) was rectified, flatfielded, background subtracted and then, the individual frames for each spectrum were combined (see Fig. 2.7). For the spectroscopic flux calibration the spectroscopic standard star LTT7987 (Hamuy et al., 1994) was observed and the two-dimensional spectra were flux calibrated. Finally, one-dimensional spectra were extracted from the two-dimensional, flux-calibrated ones. 184 of 242 observed astronomical objects (76 %) have either a continuum and/or emission line(s).

The optical/NIR counterpart ($I = 24.0$ mag) of MM J120530–0741.6 was at the edge of a slit and no useful spectral information was extracted from the two-dimensional spectral frame. For the counterpart of MM J120522–0745.1 ($I = 23.3$ mag) a very weak, low signal-to-noise continuum was extracted but no emission line was detected. No continuum was detected for the counterpart ($I = 24.9$ mag) of MM J120526–0746.6. Based on our photometric redshift estimates obtained with *hyperz*, we estimated for MM J120522 – 0745.1 a redshift $z_{phot} = 1.25^{+0.06}_{-0.06}$. Taking into account this z_{phot} , only

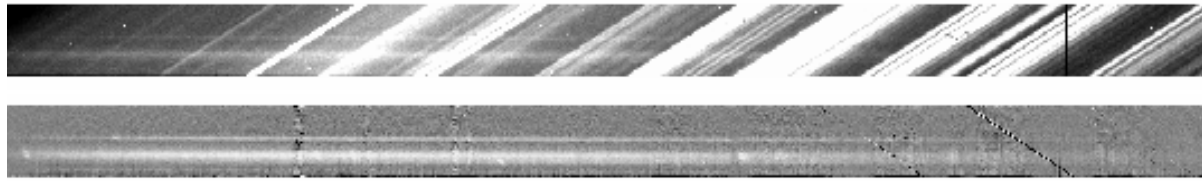


Figure 2.7 *Top Panel:* Two-dimensional raw spectrum taken with an inclined slit in order to observe two objects at the same time. *Bottom Panel:* Two-dimensional spectrum of the same region of the sky as in the top panel, after flatfielding, rectification, wavelength calibration, background subtraction and co-adding. The continuum of two objects with several emission lines can be seen.

one strong emission line, $[\text{OII}]_{3727 \text{ \AA}}$, would have been expected to fall in our observing window of $4400 - 8800 \text{ \AA}$, but it would be in a noisy region due to skylines and background emission.

Now, we compare our nondetections with the spectroscopic identification done by Chapman, Blain, Ivison, & Smail (2003b). They reported 10 redshifts for radio-identified SCUBA galaxies, whose redshifts were confirmed through CO-interferometric observation in several cases by Neri et al. (2003) and Greve et al. (2004, in preparation). Seven out of 10 have strong $\text{Ly}\alpha$ emission whose flux densities range between 1 and $60 \mu\text{Jy}$. Only for three SCUBA sources — SMM J163704.3+410530, SMM J131201.2+424208 and SMM J105155.7+572312 — would emission, or absorption lines have fallen in our observing window. Coarse rms estimates for these sources give a range between 0.07 and $0.5 \mu\text{Jy}$ and the signal-to-noise for the continuum varies from two to 10. The rms in our spectrum is around $0.1 - 0.2 \mu\text{Jy}$ for a three hour integration with FORS2. Based on our rms and the instrumental resolution, we estimated the flux density we would have measured for a 3σ emission-line detection in the range $\sim 2.5 - 5 \mu\text{Jy}$. None of the three submm galaxies whose spectral features are in our observing windows would have been detected with our configuration and the applied integration time of 3 hours. This analysis suggests that the nondetections result from both the achieved depth of our observations and the lack of spectral features in our observing window (assuming redshifts presented by Chapman, Blain, Ivison, & Smail, 2003b).

Using the near-infrared spectrometer NIRSPEC (McLean et al., 1998) at KECK-II, we conducted long-slit spectroscopy of radio-identified counterparts of MAMBO galaxies

in March 2001 and May 2002². In the second run, we observed the $K = 20.5$ mag faint counterpart of MM J154127+6616 ($z_{CY} \sim 2.5$; Bertoldi et al., 2000). For detection of the principal emission lines ($Ly\alpha$, [OII], [OIII] and $H\alpha$), the selected K' band yields a redshift range = $1.8 - 5.8$. The radio-mm redshift estimate suggests that we would have a good chance to detect $H\alpha$ in this observing window. To center the slit on the target object an acquisition image of several minutes with the infrared slit-viewing camera (SCAM, with $45'' \times 45''$ field of view) has to be taken, but such a faint object cannot be detected in such a short amount of time. Thus the slit was centered on a relatively bright object that is detected clearly in a few minutes in the acquisition image. For the centering source ($K' = 18.1$ mag), we know the position angle ($PA = 9.7^\circ$) and the distance relative to our target, $22''$; thus, we could orient the $42''$ long and $0.76''$ wide ($R \sim 1500$) slit in such a way that both the target and the centering object are in the slit. In addition, this helps to control the stability of the slit position during the observations and to facilitate the data reduction. Due to poor weather conditions, we observed only for a total of 30 minutes under nonphotometric conditions, four frames of 450 s each.

The data were reduced in a standard manner (e.g., flatfielding, skysubtraction, wavelength calibration etc.) with the IRAF NIRSPEC tool WMKONSPEC (<http://alamoana.keck.hawaii.edu/inst/nirspec/wmkonspec/>). Neither continuum nor an emission line was detected for the K -band counterpart of the MAMBO source. Using the centering source, whose continuum was clearly visible in single exposures and finally detected at $\sim 10\sigma$ level, we estimated the depth of our observation. We compare our nondetections of $H\alpha$ in MM J154127+6616 with the results of Frayer et al. (2003), who detect $H\alpha$ in SMM J04431+0210 ($z = 2.51$; $K = 19.4$ mag) with the same configuration but more exposure time (130 minutes) at $15.8 \pm 1.0 \cdot 10^{-17} \text{ erg s}^{-1} \text{ cm}^{-2}$ with an intrinsic line width 520 km/s. Up to now, this is the only spectroscopic determination of a redshift in the NIR, reflecting how challenging and complicated this experiment is. At $2.16 \mu\text{m}$ we reach a continuum rms of $K \sim 20$ mag. Furthermore, we estimate that we would have measured a flux of $\sim 6.0 \cdot 10^{-17} \text{ erg s}^{-1} \text{ cm}^{-2}$ for a 3σ $H\alpha$ emission-line detection with an intrinsic width of 520 km/s, as reported by Frayer et al. (2003). The magnification factor for Abell 2125 that we estimate is ~ 1.3 (Ledlow 2003, priv. comm.) and the amplification of the cluster region where SMM J04431+0210 lies is 4.4

²In the recent catalogues of Abell 2125, the object observed in the March 2001 run no longer has a MAMBO detection. In addition, instrumental problems hampered this run significantly and no spectral feature was detected. Therefore, here we focus on the May 2002 run.

(Smail et al., 2002a). Our spectroscopic target is 1.1 mag fainter than the K-band counterpart of SMM J04431+0210. Thus, taking into account the magnification factors and the faintness of our source, we would only have detected the source if the H α equivalent width of our observed object had been greater than that of SMM J04431+0210.

2.5 Millimeter Photometry Mode Observations

A significant fraction of MAMBO sources — 24 of 42 sources in the NDF — are without apparent radio counterparts down to 40 μ Jy at 1.4 GHz. These sources are potentially very important, because the radio-mm spectral index by CY suggests that such sources with $S_{1.2\text{ mm}} = 2.5$ mJy and nondetection at 1.4 GHz down to 40 μ Jy may be at redshifts $z > 2.6^3$. Thus, we have compiled a list of those objects with a flux at $S_{1.2\text{ mm}} \geq 2.5$ mJy, that are typically detected at the level 3 to 5σ . Because we cannot be sure about their fluxes given the possibility of spurious sources and the uncertainties (e.g., non-uniform noise in the bolometer map, pointing errors, systematic errors) involved in reducing and calibrating the MAMBO imaging data, we carry out on-off observations (photometric mode of MAMBO) in order to confirm the source fluxes at a sufficiently high level of 5σ for a flux density of ~ 3 mJy. Only sources with $S_{1.2\text{ mm}} \geq 2.5$ mJy have a chance to be firmly detected at the PdBI in a reasonable number of observing tracks (one track ≈ 10 hours). The overall goal of this program is to search for very high-redshift mm sources, at least $z > 2.6$ where this can only be achieved through the PdBI. We are well aware of the uncertainties in the source positions that we derive from the MAMBO maps. Comparing the positions of the mm sources with radio counterparts to their radio positions, we find a typical scatter of about $3''$ (see Fig. 3.5 in § 3.2.1). The on-off observations do not yield very accurate fluxes for these sources, but they give at least lower limits. The on-off observing technique is based on the chop-nod mode and the pointing is done at the central pixel of the array. The photometric mode is more sensitive than the mapping mode. The on-off observations were carried out at the nominal MAMBO bolometer map position. In several cases the on-off pointing at the

³See <http://www.aoc.nrao.edu/~ccarilli/250.mod>. The CY radio-mm spectral index is modeled on a sample of 17 low- z star-forming galaxies observed at 850 μ m by Lisenfeld, Isaak, & Hills (2000), having infrared luminosities between $L_{IR} \sim 10^{10} - 10^{12} L_{\odot}$. A dust temperature of approximately 35–40 K is assumed. This is a subsample of bright IRAS galaxies observed at CO(1–0) by Sanders, Scoville, & Soifer (1991) and is not complete.

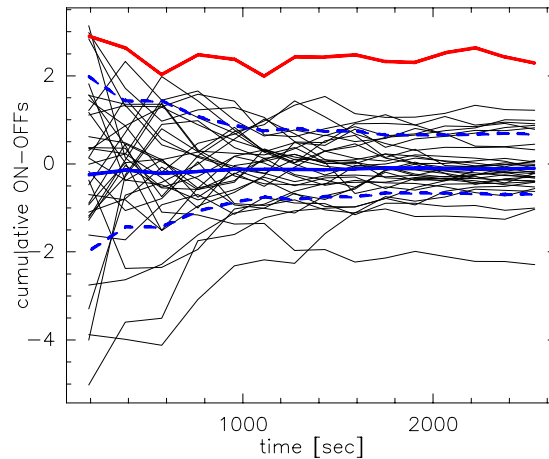


Figure 2.8 Presentation of $\approx 70\%$ of the on-off data taken on MM J120539-0741.0. The flux density is plotted versus the on-off integration time. The blue, solid line is the measured signal of 2.3 ± 0.5 mJy on the on-target channel. The dashed lines represent the rms dispersion of the signal and the thin lines are the cumulative signal on the individual bolometer elements.

nominal MAMBO position did not confirm its flux in the map; therefore we targeted one or two unusual objects seen nearby in our deep optical/near-IR images or faint μ Jy radio sources outside the error circle of the nominal MAMBO bolometer position.

The on-off observations were carried out in winter 2001/2002 with the 37-(and in few cases the 117-) element bolometer MAMBO. In total, 11 sources were observed in both the NTT Deep Field and the $z = 0.24$ cluster Abell2125. Each observation consists of several scans. These scans are subdivided in 12 to 16 subscans of 10-second targeted on-off observations. After every subscan, the telescope is chopped. Thus, the former “off” beam becomes the “on” beam, reducing the systematic error significantly. Taking into account overheads, an observing sequence lasts ~ 20 to 30 minutes. The chopping frequency is 2 Hz and the secondary mirror is chopped by $32''$. The data reduction was performed with the data reduction package MOPSI (Zylka, 1998) and flux calibration was based on the observations of planets and yielded 4500 counts/Jansky. The results of the observations are presented in Tab. 2.3. One source — MM J120539-0741.0 — was detected at 5σ level, $S_{1.2\text{ mm}} = 2.6 \pm 0.5$ mJy, see Fig. 2.8. In addition, two sources — MM J120545-0738.8 and MM J153232+6612.8 — were detected at $\sim 2.5\sigma$ level with fluxes of 2.6 and 0.9 mJy. In Fig. 2.9, we plot the map flux versus the on-off flux. In general, the on-off flux is lower than the map flux. Accounting for the assumed errors,

Table 2.3. MAMBO on-off observations

Pointing (1)	Source (2)	RA (J2000) (3)	DEC (J2000) (4)	MAMBO (5)	Subscans (6)	on-off Flux (7)	Map Flux (8)	Comments (9)
NDF-06p1 (<i>new22</i>)	MM J120543-0743.5	12:05:43.92	-07:43:30.6	37	100	-0.6±0.9	2.9±0.7(3.0±0.7)	nom. MAMBO pos.
NDF-06p2 (<i>new22</i>)	MM J120543-0743.6	12:05:43.54	-07:43:36.5	37	80	-1.7±1.4	2.9±0.7	radio (46), outside
NDF-09p1 (<i>new33</i>)	MM J120539-0741.0	12:05:39.95	-07:41:02.1	37	340	2.7±0.5	3.6±0.7(1.9±0.6)	nom. MAMBO pos.
NDF-09p2 (<i>new33</i>)	MM J120540-0741.0	12:05:40.09	-07:41:00.5	37	80	1.8±1.3	3.6±0.7	red counterpart
NDF-23 (<i>new19</i>)	MM J120529-0744.8	12:05:29.61	-07:44:52.5	37	100	1.3±1.2	2.5±0.7(2.3±0.5)	nom. MAMBO pos.
NDF-48p1 (<i>new09</i>)	MM J120508-0747.0	12:05:08.37	-07:47:02.7	37	180	0.5±1.1	3.3±0.7(3.2±0.9)	nom. MAMBO pos.
NDF-a20 (<i>new12</i>)	MM J120518-0746.7	12:05:18.78	-07:46:44.4	37	80	-1.6±1.4	2.7±0.7 (1.8±0.7)	nom. MAMBO pos.
NDF-a27p1 (<i>new40</i>)	MM J120545-0738.8	12:05:45.96	-07:38:51.6	37	260	2.6±1.0	3.7±0.7 (3.7±0.8)	nom. MAMBO pos.
NDF-a27p2 (<i>new40</i>)	MM J120545-0738.8	12:05:45.72	-07:38:52.5	37	128	1.9±1.0	3.7±0.7	radio (40), inside
NDF-a27p3 (<i>new40</i>)	MM J120545-0738.9	12:05:45.50	-07:38:58.0	37	100	1.7±1.3	3.7±0.7	radio (59), outside
A2125-I	MM J154137+6608.0	15:41:37.99	66:08:02	37	252	0.5±0.7	3.0±0.8	nom. MAMBO pos.
A2125-I	MM J154137+6608.0	15:41:37.99	66:08:02	117	64	1.1±1.3	3.0±0.8	nom. MAMBO pos.
A2125-II	MM J154120+6612.0	15:41:20.44	66:12:03	37	196	1.1±0.7	3.0±0.8	nom. MAMBO pos.
A2125-II	MM J154120+6612.0	15:41:20.44	66:12:03	117	80	1.3±1.75	3.0±0.8	nom. MAMBO pos.
A2125-III	MM J154120+6617.9	15:41:20.70	66:17:57	37	196	-0.5±0.7	2.5±0.8	nom. MAMBO pos.
A2125-III	MM J154120+6617.9	15:41:20.70	66:17:57	117	112	-0.8±3.4	2.5±0.8	nom. MAMBO pos.
A2125-IV	MM J154204+6620.0	15:42:04.42	66:20:03	37	336	0.2±0.7	2.7±0.8	nom. MAMBO pos.
A2125-V	MM J153232+6612.8	15:42:32.90	66:12:53	37	448	0.9±0.4	2.5±0.8	nom. MAMBO pos.

Note. — Col. (1) — MAMBO on-off Target (Pointing). To be complete, for the NDF source we give in parentheses (and italics) the name according the catalog as of early 2002 which is the base for the identification done in this work.

Col. (2) — MAMBO source.

Col. (5) — Number of the MAMBO bolometer elements.

Col. (6) — Number of subscans á 10 seconds.

Col. (7) — Units of 1.2 mm flux density in mJy in on-off mode.

Col. (8) — Units of 1.2 mm flux density in mJy in the bolometer map. Unfortunately, for the individual targets no flux error in the map is known. Thus, these flux errors are means of all detected sources both in the NDF and the Abell 2125 of the catalog as early 2002. In parenthesis, we give the flux and the error of the catalog (new-sources) as of early 2002 for comparison.

Col. (9) — Number in () is flux of the targeted radio source in μ Jy at 1.4 GHz. Inside/outside means that the selected pointing position is inside/outside the error circle estimate of the nominal MAMBO position.

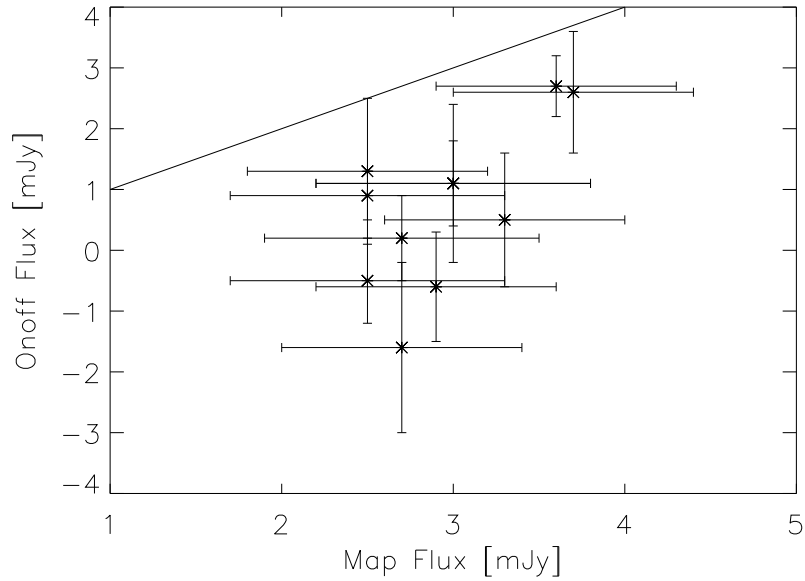


Figure 2.9 Map flux versus on-off flux for the sample presented in Tab. 2.3. In cases where several pointings for one source were performed, the most significant result was taken. On the solid line, map flux is equal to the on-off flux. In general the map flux is higher than the on-off flux.

the on-off and the map-fluxes were compared for the 11 sources. Only in four of 11 cases are the fluxes consistent within the assumed errors. Adjusting the map errors in order to make them consistent with the measured on-off values implies that for all seven MAMBO sources the S/N is $< 2.5\sigma$. This analysis indicates that probably a significant fraction of MAMBO sources without a radio detection in the bolometer map are not real 1.2 mm detections. For comparison, Eales et al. (2003) observed 14 1.2 mm sources that were selected from MAMBO bolometer maps and had interferometric detections, in the MAMBO on-off mode. Eales et al. (2003) find that in general there is a good agreement between MAMBO survey and photometric flux. This result strengthens our finding that the missing flux in the photometric mode in a significant number of cases is not due to pointing/positional uncertainties but rather due to not spurious survey detections.

Chapter 3

IDENTIFICATION RESULTS

In this chapter I present the optical/near-infrared identifications of MAMBO 1.2 mm galaxies based on mm and/or cm interferometry and discuss the implications. The chapter is divided in three parts: (1) describing the PdBI identifications, (2) presenting the securely identified VLA sources in the NTT Deep Field, and (3) summarizing the identification results and conclusions from this work for the whole (sub)mm source population.

3.1 Identification of the PdBI Detections

The identification of MAMBO 1.2 mm galaxies began with the successful detection and subarcsecond location of four of five MAMBO galaxies with mm interferometry, probing directly their dust emission. The fluxes of these four PdBI detections in the observed bands are listed in Tab. 3.1 and 3.2.

3.1.1 NTT Deep Field

MM J120546–0741.5 The mm and radio interferometric observations locate MM J120546–0741.5 at a position near the center of the MAMBO beam (0.9" and 1.3" distance from the nominal MAMBO position, respectively), see Fig. 3.1. The faint K-band counterpart ($K = 21.9 \pm 0.3$ mag) was detected at the mm interferometric position in a 1.5" aperture in ISAAC imaging, see Fig. 3.2. The K-band counterpart is rather compact (size of $\sim 1''$). No other optical nor near-infrared sources are detected within the 11" MAMBO beam. Unfortunately, the seeing-limited resolution of our ground-based images does not allow us to make detailed statements about the morphology of these

objects, e.g., to reveal a possible multi-component structure detected in brighter optical counterparts of submm galaxies (e.g., Ivison et al., 2002). An excellent case for this is the well-known Lyman break galaxy Westphal MMD-11 (e.g., Chapman et al., 2000; Shapley et al., 2001; Chapman, Shapley, Steidel, & Windhorst, 2002a), detected at $850 \mu\text{m}$ at the 3σ level ($5.5 \pm 1.4 \text{ mJy}$), where high-resolution HST imaging revealed multiple optical/near-infrared components within a region of size of $\sim 1''$.

MM J120539–0745.4 For MM J120539–0745.4, there are three significant optical/near-IR sources within the MAMBO beam (see Fig. 3.1), so an identification lacking interferometric observations probably would have chosen one of them as the most likely counterpart. Strikingly, the mm/cm interferometric observations demonstrate MM J120539–0745.4 to be a blank field both in SOFI and the deeper ISAAC images (to limits listed in Table 3.1), with separations from the nearest optical/near-IR sources that are well above our estimated astrometric uncertainty (see Fig. 3.1 and Fig. 3.2). The three optical/NIR sources are offset with respect to the PdBI position by $2.4''$ to the south-west ($K_s = 20.5 \text{ mag}$), $2.5''$ to the south-east ($K_s = 21.1 \text{ mag}$), and $2.9''$ to the north-east ($K_s = 20.5 \text{ mag}$). The photometric analysis shows that these three nearby sources are probably not physically related to each other (SW $z_{\text{phot}} = 1.70$, SE $z_{\text{phot}} = 0.92$, NE $z_{\text{phot}} = 0.46$). In the NE component 16c, we weakly detected [OII], $H\beta$ and [OIII] at a redshift of 0.55, close to its z_{phot} .

MM J120517–0743.1 As in the case of MM J120546–0741.5, a compact, $1''$ K-band counterpart was detected at $K = 22.5 \pm 0.3 \text{ mag}$ (Lehnert et al. 2004, in preparation) in ultradeep ISAAC imaging (see Fig. 3.1 and 3.2).

3.1.2 Abell 2125

J154127+6615 Before the mm interferometric observations were performed, the existence and location of this source were determined by mm on-off and VLA observations, presented by Bertoldi et al. (2000). Similar to the cases of MM J120546–0741.5 and MM J120539–0745.4, the mm/cm interferometric positions are consistent within the error estimates. Neither in the radio nor in the mm is the source resolved, and the radio gives the limit of the maximum size of $< 1.3''$. Based on the interferometric observations, the MAMBO source is classified as a blank field in optical and near-infrared images

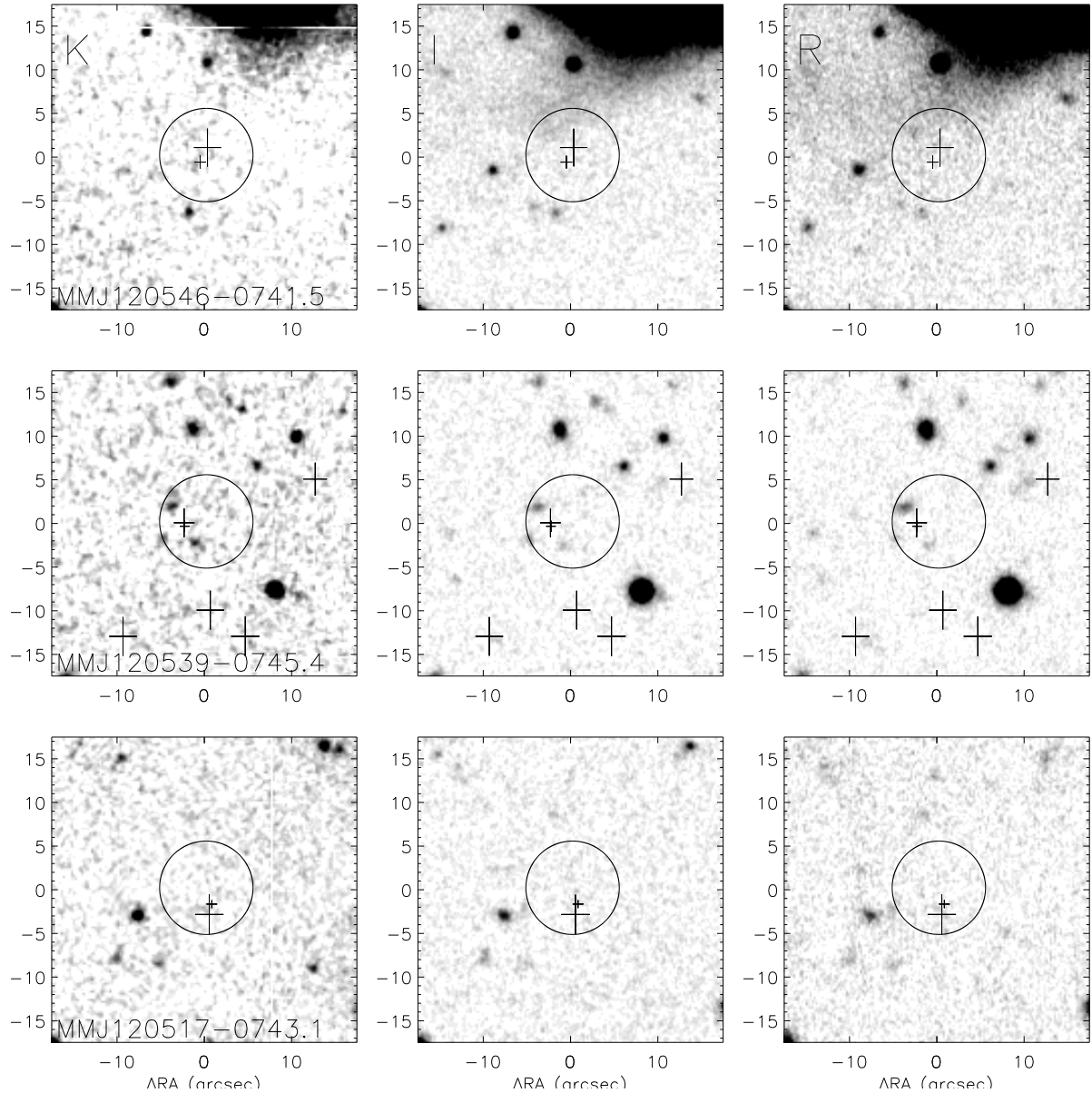


Figure 3.1 K-, I-, and R-band images (left to right) for the fields of the three MAMBO sources, from top to bottom MM J120546–0741.5, MM J120539–0745.4, and MM J120517–0743.1. Each image is $35'' \times 35''$ and oriented such that north is at the top and east is to the left. The large circles represent the size of the MAMBO beam ($\sim 11''$ diameter). Small crosses indicate the position and 2σ errors of the PdBI detection, and the larger crosses indicates the positions and 2σ errors obtained from VLA 1.4 GHz interferometry. No near-infrared or optical counterparts are detected in these deep images, down to a limit of $K_s = 21.9$.

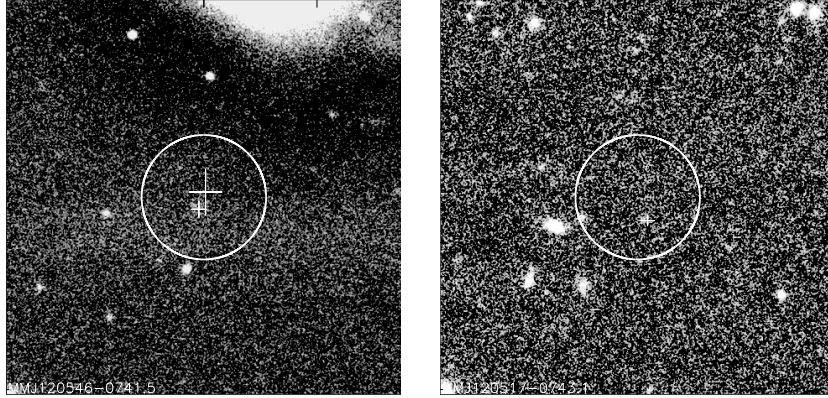


Figure 3.2 Ultradeep VLT-ISAAC K-band images of the fields of the two PdBI detections MM J120546–0741.5 and MM J120517–0743.1, left and right panel, respectively. At the mm interferometric positions, near-infrared counterparts were detected for both of them. The K-band counterparts are extremely faint ($K = 21.9 \pm 0.3$ mag and 22.5 ± 0.3 mag, respectively). Symbols are identical to Fig. 3.1.

down to $R = 24.9$ mag and $K = 21.2$ mag (see also Fig. 3.3). Assuming a magnification factor of 1.3 (Ledlow 2003, priv. comm.), the intrinsic K-band detection limit would be $K = 21.5$ mag. A most likely redshift of $z = 2.4_{-0.8}^{+1.3}$ based on the radio-mm spectral index is estimated.

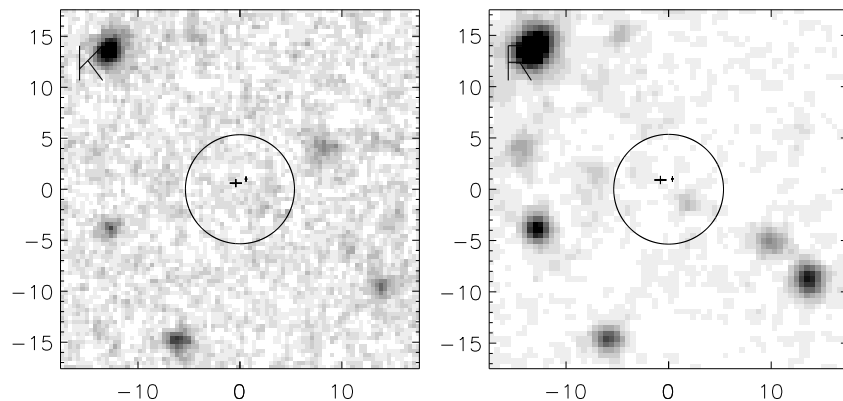


Figure 3.3 K- and R-band images (left to right) for the field of the MAMBO source J154127+6615. Size of each image and orientation is as in Fig. 3.1. The symbols are as in Fig. 3.1. No near-infrared or optical counterparts are detected in either band.

Table 3.1. Fluxes of the three NDF mm galaxies with PdBI detections

Band	Unit	MM J120546–0741.5	MM J120539–0745.4	MM J120517–0743.1	Comment
(1)	(2)	(3)	(4)	(5)	(6)
m_B	mag	>27.4	>27.4	$\approx 26.1^*$	WFI
m_V	mag	>26.6	>26.6	$\approx 25.3^*$	WFI
m_R	mag	>26.2	>26.2	$\approx 25.4^*$	WFI
m_I	mag	>25.5	>25.5	>25.5	WFI
m_Z	mag	>26.4	>25.9	25.9	FORS2
m_J	mag	>24.0	>24.0	>23.9	SOFI (p)
m_{K_s}	mag	21.9 ± 0.3	>22.7	22.5 ± 0.3	ISAAC
$S_{1.2\text{ mm}}$	mJy	6.5 ± 0.8	3.5 ± 0.8	4.4 ± 0.8	MAMBO
$S_{1.26\text{ mm}}$	mJy	6.1 ± 1.2	6.4 ± 1.0	3.9 ± 0.9	PdBI
$S_{3.16\text{ mm}}$	mJy	<0.84	<0.39	<0.60	PdBI
$S_{1.4\text{ GHz}}$	μJy	44 ± 13	56 ± 13	40 ± 13	VLA

Note. — Col. (1) — Band in which flux is measured.

Col. (2) — Units of the flux density measurements.

Col. (3)-(5) — Measurements for the three objects. Optical/near-IR magnitudes were measured in a $2''$ diameter aperture and are on the “Vega” system. Only magnitudes of the ISAAC observations are given in a $1.5''$ diameter aperture. The z-band magnitudes are given in the BD+17 4708 system. Limits are 3σ . *: Detection is tentative.

Col. (6) — Comments. (p) = Limits for MM J120517–0743.1 from public NTT deep field data, http://www.eso.org/science/sofi_deep/index.html.

Table 3.2. Fluxes of the Abell 2125 PdBI detection

Band	Unit	MM J154127+6615	Comment
(1)	(2)	(3)	(4)
m_R	mag	>24.9	CAFOS
m_J	mag	>23.5	APO-GRIM (Bertoldi et al., 2000)
m_{K_s}	mag	>21.2	OMEGA-Prime
$S_{1.2\text{ mm}}$	mJy	4.0 ± 0.5	MAMBO on-off mode (Bertoldi et al., 2000)
$S_{1.26\text{ mm}}$	mJy	3.2 ± 0.5	PdBI
$S_{3.16\text{ mm}}$	mJy	<0.54	PdBI
$S_{1.4\text{ GHz}}$	μJy	81 ± 13	VLA (Bertoldi et al., 2000)

Note. — Col. (1) — Band in which flux is measured.

Col. (2) — Units of the flux density measurements.

Col. (3) — Measurements for MM J154127+6615. Optical/near-IR magnitudes were measured in a $2''$ diameter aperture, and are on the “Vega” system. Limits are 3σ .

Col. (4) — Comments.

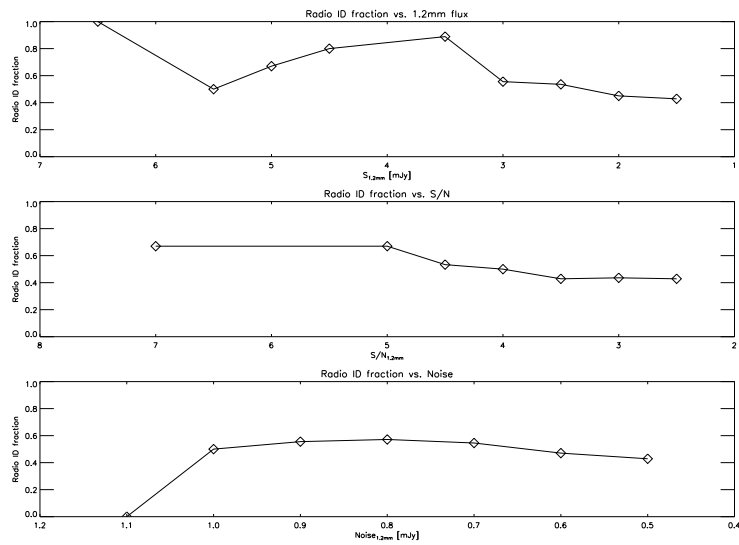
3.2 Identification of the VLA Detections

3.2.1 Association of MAMBO Sources with Radio Sources

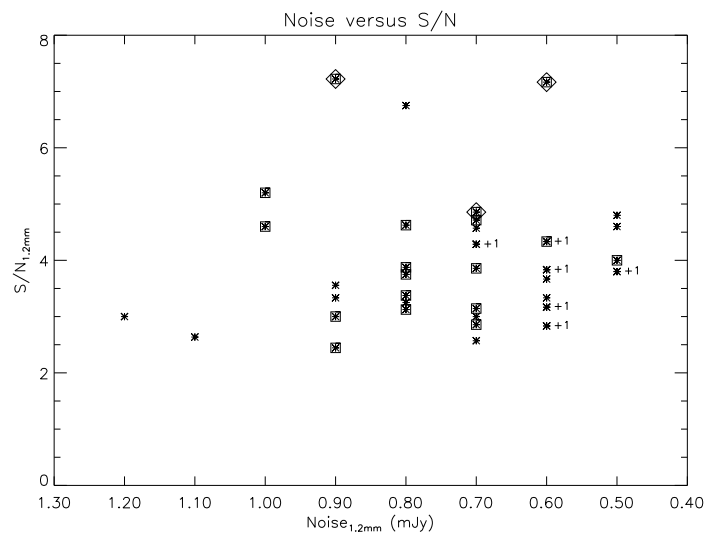
In order to obtain more accurate positions for the MAMBO sources through the use of their radio continuum emission, we have searched the 1.4 GHz VLA data for peaks of at least $40 \mu\text{Jy}$ ($\sim 3\sigma$) in the region where the MAMBO sources are located, out to radii of about $10'$ from the phase center. Table 3.3 lists the MAMBO sources in the catalog as of early 2002 that have radio sources with peak positions less than $7''$ from the nominal MAMBO map position. This radius is more than half of the FWHM of the MAMBO beam and should not exclude real associations even in the case of slight systematic offsets. The table, like all our subsequent analyses, does not include the well-detected quasar BR1202–0725, which drove the original selection of the public ESO NDF, and thus cannot be considered an unbiased representative of the mm galaxy population. A more complete description of the MAMBO data analysis will be given in F. Bertoldi et al. (2004, in preparation). At $5'' \times 7''$ resolution, our B-configuration data do not put interesting constraints on the extent of the radio emission of the detected galaxies. Table 3.3 also lists the corrected Poissonian probability that an association is a chance coincidence, derived using the approach of Downes, Peacock, Savage, & Carrie (1986) which corrects the simple Poissonian probability of an observed association for the possibility of associations of different nature but similar probability. In deriving these probabilities we adopt the raw counts of $\geq 40 \mu\text{Jy}$ peaks in the region of our VLA image covered by the MAMBO data, which are significantly above the true 1.4 GHz source counts for a flux close to the detection limit. Using true radio source counts (e.g., Richards, 2000) would thus have underestimated the chance of a false association. The probabilities listed, together with the fact that 42 sources from the original MAMBO list were searched for nearby radio peaks, suggest that several of the associations may be chance. This statistical analysis, however, does not adequately consider that the excess of $\sim 40 \mu\text{Jy}$ peaks boosting the rate of chance coincidences is largely due to peaks in the VLA map that cluster in certain regions because of uneven noise and striping caused by residual calibration errors. Considering this enables us to identify those associations that are more likely to be spurious by inspection of the distribution of $\geq 40 \mu\text{Jy}$ peaks in the radio map. The quality of an associated radio source is indicated in Table 3.3, with “uncertain” assigned to sources with an excess of similar brightness peaks near the suggested radio source, and in particular with alignments of peaks due to striping. We also consider as uncertain radio peaks that

do not remain above $40 \mu\text{Jy}$ in a radio image where larger-scale variations are partially removed by subtracting a $20''$ median-smoothed version of the radio image, as well as two faint radio peaks near sources No. 10 and 25 that are only above $40 \mu\text{Jy}$ in this image to which we refer as the “background-subtracted” image below. Of the identifications that we consider “good” below, all but source 13 are either above 4σ in the original radio map, or confirmed by PdBI mm interferometry.

Uncertainties in bolometer maps always raise the question of how reliable the (sub)mm sources are and which source detection is. One approach to tackle this is a detailed statistical analysis of the bolometer map. Another approach is to use the identification through mm and/or cm interferometry. Here we employ such an analysis to derive conclusions about the reliability of the whole MAMBO 1.2 mm sample in the NTT Deep Field. Ivison et al. (2002) performed a similar analysis for the whole UK 8 mJy SCUBA survey, and ultimately removed six spurious sources out of 36 sources from the list of Scott et al. (2002). All sources that lie in the noisiest regions of the SCUBA maps ($\sigma_{850 \mu\text{m}} \geq 3.5 \text{ mJy}$) — four of them being the brightest sources in the Lockman Hole — have no radio counterparts. This suggests that they are probably spurious sources. Thus, (sub)mm sources without an interferometric identification could be candidates for spurious sources in the worst case. We use our interferometric identification to investigate in detail the reliability of our mm detection. In Fig. 3.4(a) we plot the cumulative distribution of radio identification rate versus 1.2 mm flux, S/N and the 1.2 mm noise, from top to bottom. Using these diagnostic plots we search for trends among mm sources without a radio counterpart in order to derive conclusions about their reliability. The plot of cumulative identification rate versus 1.2 mm flux shows that the brightest submm source is identified contrary to the case of the SCUBA map of the Lockman Hole. In the flux bins from 5.5 to 3.5 mJy, the cumulative identification rate is $\sim 60 - 80 \%$ and for the fainter sources around $\sim 40 \%$, implying that fainter mm sources can also be reliable detections but with lower probability. In addition, the identification rate does not depend on the signal-to-noise ratio. One source near the edge of the map has a noise of 1.15 mJy, and is not identified in the radio. At a source S/N of 2.6, the cumulative radio ID rate is $\sim 40 \%$. We conclude that indeed this source could be spurious. From 1.0 down to 0.5 mJy, we report no trend between S/N and the noise as the cumulative radio identification rate ranges between 0.4 – 0.6, see Fig. 3.4(b). We conclude that sources located in the noisiest regions of our bolometer map, i.e. at the edges, cannot be considered automatically as candidates for spurious mm detection (cf. Ivison et al., 2002).



(a) Cumulative distribution of the radio-mm identification rate versus 1.2 mm flux (top), S/N (middle), and σ (bottom).



(b) σ versus S/N of all 42 NTT Deep Field MAMBO 1.2 mm galaxies. The radio-identified sources are enclosed by a box and the PdBI detections are enclosed by a diamond. +1 at the right side of a symbol indicates that another mm source has the S/N and σ . No trend is evident.

Figure 3.4 Tests of the reliability of the (sub)mm source detections.

The mean offset between the nominal MAMBO and VLA positions for all 18 sources is $\Delta_{mm-radio} = 3.3 \pm 0.3''$, ranging from $2.8 \pm 0.4''$ to $3.7 \pm 0.4''$ for good and uncertain sources. Figure 3.5 displays the mm–radio offsets corresponding to the identifications listed in Table 3.3. The dominance of real associations is clear.

The separations found are consistent with a typical MAMBO position error of about $3''$, and confirm the radius of $7''$ as a sensible choice for searching for associated radio sources. In the radio, the position uncertainty depends on the flux (see § 2.2.3 and Fomalont, 1999). Thus, we investigated whether the uncertainty of the bolometrically determined position depends on the 1.2 mm flux, based on the radio identification work. This analysis is presented in the left panel of Fig. 3.6. In the flux range from 2 – 3 mJy there is a wide spread of mm–radio offsets. We see a tentative trend such that at higher flux densities ($S_{1.2\text{ mm}} \geq 4\text{ mJy}$) the position uncertainty decreases with increasing flux. Both for the “good” and “uncertain” sources, no systematic offset between the 1.2 mm and the 20 cm position is measured ($\alpha_{1.2\text{ mm} - 20\text{ cm}} = -0.42 \pm 0.41''$ and $\delta_{1.2\text{ mm} - 20\text{ cm}} = -0.38 \pm 0.41''$, see also the right panel of Fig. 3.6). This shows that systematic position uncertainties are not present in the MAMBO map, do not affect the chosen search radius, and do not depend on the reliability of the sources.

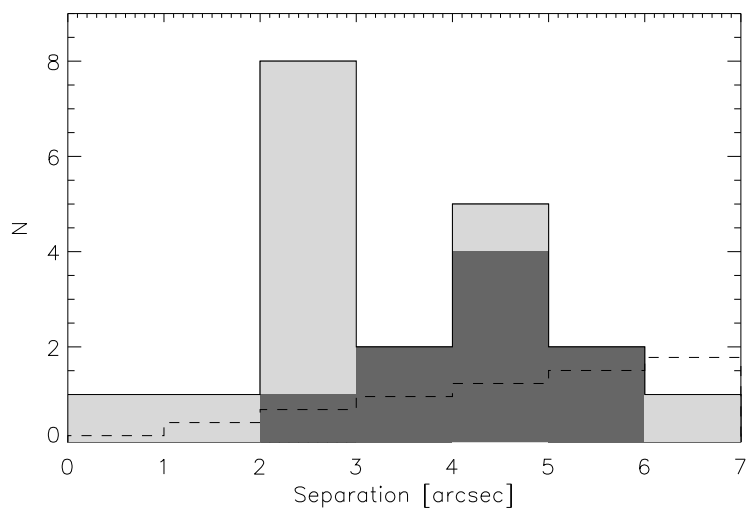


Figure 3.5 Histogram of separations between mm positions from the MAMBO map and VLA positions of associated radio sources. Light and dark gray indicate the “good” and “uncertain” sources from Tab. 3.3. The dashed histogram indicates the expected number of unrelated background radio peaks.

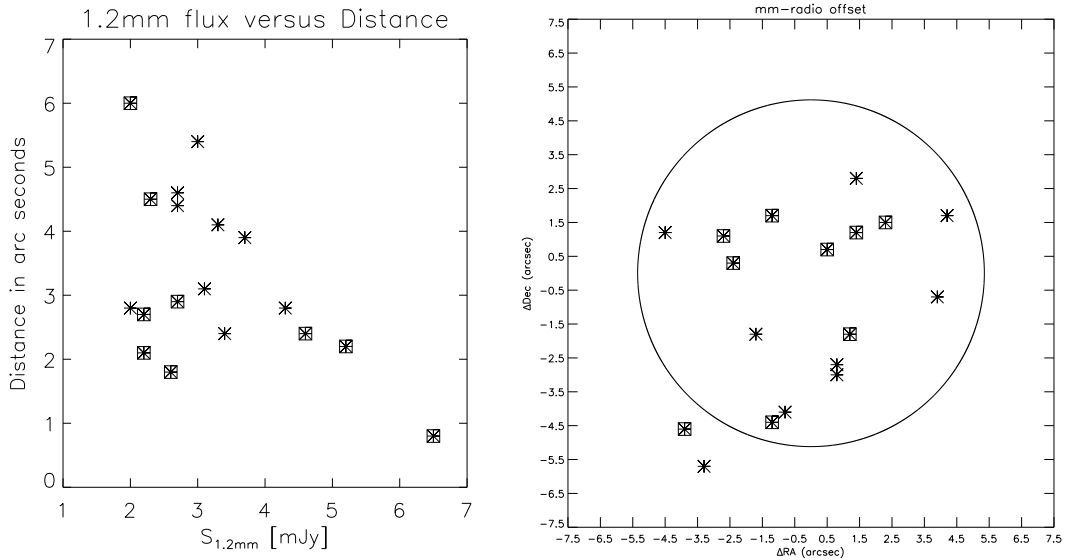


Figure 3.6 *Left Panel:* Radio-mm offset versus 1.2 mm flux. “Good” radio sources are marked by a box. *Right Panel:* Offset between mm and radio positions of 18 radio-identified MAMBO sources. The mm position is at the coordinate (0,0). The circle represents the MAMBO beam. “Good” radio sources are marked with a box. No systematic offset between “good” and “uncertain” sources is seen.

To summarize, for 18 out of 42 MAMBO sources in the NDF, interferometric positions are available. We consider 11 of these 18 reliable, either through good radio peaks or through direct PdBI mm interferometry. Interestingly, the PdBI data confirm the reality of two of the more uncertain radio sources, increasing confidence in the rest of these objects. The remaining MAMBO sources without radio associations could be at high redshifts (with correspondingly fainter radio fluxes), or have MAMBO fluxes considerably boosted by noise (see discussion in § 2.5). Given the signal-to-noise ratios, this is possible as is the existence of a number of spurious entries in the original MAMBO list.

Table 3.3. NDF MAMBO sources and associated 1.4 GHz radio sources

Source	MAMBO 1.2 mm properties				VLA 1.4 GHz properties								
	No	RA (J2000)	DEC (J2000)	$S_{1.2\text{ mm}}$ mJy	RA (J2000)	DEC (J2000)	$S_{1.4}$ μ Jy	$\alpha_{mm-radio}$ arcsec	$\delta_{mm-radio}$ arcsec	Sep arcsec	P	Q	Comment
(1)	(2)	(3)	(4)	(5)	(6)	(7)	(8)	(9)	(10)	(11)	(12)	(13)	(14)
MM J120507-0748.1	03	12:05:07.96	-07:48:11.9	4.6±1.0	12:05:08.12±0.03	-07:48:11.6±0.6	88	-2.4	+0.3	2.4	0.009	g	
MM J120508-0743.1	26	12:05:08.36	-07:43:06.8	2.7±0.7	12:05:08.66±0.06	-07:43:05.6±1.2	42	-4.5	+1.2	4.6	0.107	u	
MM J120509-0740.0	34	12:05:09.75	-07:40:02.5	3.3±0.6	12:05:09.80±0.05	-07:40:06.6±1.1	47	-0.8	-4.1	4.1	0.072	u	
MM J120510-0747.0	10	12:05:10.97	-07:47:00.4	3.1±0.8	12:05:10.88±0.06	-07:46:57.6±1.3	41	+1.4	+2.8	3.1	0.074	u	
MM J120516-0739.4	36	12:05:16.21	-07:39:27.1	2.2±0.6	12:05:16.06±0.03	-07:39:25.6±0.5	459	+2.3	+1.5	2.7	0.002	g	
MM J120517-0743.1	25	12:05:17.93	-07:43:06.9	4.3±0.6	12:05:17.88±0.06	-07:43:09.6±1.3	40	+0.8	-3.0	2.8	0.070	u	
					12:05:17.86±0.02	-07:43:08.5±0.2							PdBI pos.
MM J120519-0749.5	01	12:05:19.98	-07:49:33.8	5.2±1.0	12:05:19.90±0.04	-07:49:35.6±0.7	72	+1.2	-1.8	2.2	0.009	g	
MM J120520-0738.9	39	12:05:20.45	-07:38:56.7	2.7±0.8	12:05:20.63±0.03	-07:38:55.6±0.5	336	-2.7	+1.1	2.9	0.003	g	
MM J120522-0745.1	18	12:05:22.86	-07:45:10.0	2.0±0.5	12:05:23.12±0.03	-07:45:14.6±0.6	90	-3.9	-4.6	6.0	0.035	g	
MM J120524-0747.3	08	12:05:24.86	-07:47:20.9	2.0±0.6	12:05:24.81±0.05	-07:47:23.6±1.1	47	+0.8	-2.7	2.8	0.042	u	
					12:05:24.54±0.05	-07:47:20.6±1.1	48	+4.8	+0.3	4.8	0.082	u	
MM J120526-0746.6	13	12:05:26.85	-07:46:41.8	2.6±0.6	12:05:26.76±0.06	-07:46:40.6±1.3	41	+1.4	+1.2	1.8	0.035	g	
MM J120530-0741.6	29	12:05:30.17	-07:41:41.2	2.3±0.6	12:05:30.25±0.03	-07:41:45.6±0.6	85	-1.2	-4.4	4.5	0.024	g	
MM J120530-0747.7	07	12:05:30.85	-07:47:43.9	3.0±0.8	12:05:31.07±0.06	-07:47:39.6±1.3	40	-3.3	-5.7	5.4	0.134	u	
MM J120531-0748.1	04	12:05:31.41	-07:48:07.2	2.7±0.9	12:05:31.13±0.05	-07:48:05.5±1.0	53	+4.2	+1.7	4.4	0.058	u	
MM J120534-0738.3	42	12:05:34.81	-07:38:20.2	>2.2±0.9*	12:05:34.89±0.04	-07:38:18.5±0.9	61	-1.2	+1.7	2.1	0.012	g	
					12:05:34.49±0.06	-07:38:17.6±1.3	41	+4.8	+2.6	5.5	0.130	u	
MM J120539-0745.4	16	12:05:39.37	-07:45:24.7	3.4±0.7	12:05:39.48±0.05	-07:45:26.5±1.0	55	-1.7	-1.8	2.4	0.020	u	
					12:05:39.47±0.02	-07:45:27.0±0.3							PdBI pos.
MM J120545-0738.8	40	12:05:45.98	-07:38:51.8	3.7±0.8	12:05:45.72±0.06	-07:38:52.5±1.3	40	+3.9	-0.7	3.9	0.102	u	
MM J120546-0741.5	31	12:05:46.56	-07:41:33.2	6.5±0.9	12:05:46.53±0.06	-07:41:32.5±1.2	42	+0.5	+0.7	0.8	0.009	g	
					12:05:46.59±0.02	-07:41:34.3±0.4							PdBI pos.

Note. — Col. (1) — MAMBO source.

Col. (2) — Short number on the original MAMBO NDF source list.

Col. (3)-(4) — J2000 coordinates of the source in the MAMBO data.

Col. (5) — MAMBO 1.2 mm flux density. *: The source MM J120534-0738.3 appears to be extended and may be multiple or smeared. For consistency with the other sources, we list its peak flux which is effectively a lower limit to the true flux. The source was included because of a reliable detection in total flux and a 1.4 GHz counterpart.

Col. (6)-(7) — J2000 coordinates of the associated radio source.

Col. (8) — VLA 1.4 GHz peak flux density. The average rms of the radio map is 13 μ Jy. See also Col. (13) for possible effects of striping residuals caused by bright sources contained in the radio map (see §3.2.1).

Col. (9) — Separation in RA between the 1.2 mm and the 1.4 GHz position.

Col. (10) — Separation in DEC between the 1.2 mm and the 1.4 GHz position.

Col. (11) — Separation between MAMBO position and VLA position.

Col. (12) — Probability that the association is a chance coincidence.

Col. (13) — Quality flag for good (g) and uncertain (u) radio sources. To declare the quality of a radio source good, two criteria have to be fulfilled: (1) Source does not disappear in the “background-subtracted” radio map, and (2) there is no eye-catching clustering of greater than 40 μ Jy peaks in the adjacent region.

Col. (14) — Comments.

3.2.2 Notes on Individual Objects

In this subsection, the 18 radio-identified MAMBO galaxies will be discussed case by case. In addition, the optical and/or near-infrared counterparts of mm sources will be presented. We consider as possible counterparts optical/NIR objects that are less than twice the interferometric positional error (see Tab. 3.3), away from the interferometric position. BzK color composites of the objects are shown in Fig. 3.7. In Fig. 3.8 – 3.25, we present BVRIZJK images and RzK color composites for the fields of the radio-identified MAMBO galaxies.

In Tab. 3.4, the position¹ and the BVRIZJK photometric data for objects close to interferometric radio positions are listed with a combination of the short MAMBO number and a letter increasing in alphabetic order with the distance from the interferometric radio position. The short MAMBO numbers are consistent with the NTT-MMnn numbers listed in Eales et al. (2003) where a comparison between 850 μm and 1.2 mm flux for MAMBO sources was performed. Again, we have derived the corrected Poissonian probabilities for a chance coincidence computed according to Downes, Peacock, Savage, & Carrie (1986), considering a search radius of twice the radio positional error. Table 3.4 lists these probabilities for the objects inside the 2σ search circle, adopting the K-band number counts of Totani et al. (2001b). Deriving probabilities in this way ignores color information and thus implicitly assumes a similar color distribution of counterparts and field population. In reality the colors differ (§ 3.3.1), i.e. we are overestimating the probability of a particular object being a random coinciding member of the field population.

For convenience, salient properties of the counterparts are collected in Table 3.5, and full color information can be extracted from Table 3.3. Redshifts from the radio/submm spectral index are based on the flux densities from Table 3.3 and the relation of Carilli & Yun (1999, 2000). For several objects we present arguments on the potential role of lensing by individual foreground galaxies. These are simple plausibility arguments based on the observed K magnitudes and photometric redshifts, using after K-correction the K-band Faber-Jackson relation of Pahre, Djorgovski, & de Carvalho (1998) to estimate the velocity dispersion and the isothermal sphere approximation (e.g., Peacock, 1999, his eq. 4-14) to estimate the Einstein ring radius.

As described in § 2.2.3, the source catalog was created with the source detection

¹Wavelength-dependent morphology can lead to small offsets of the peaks in certain bands from these average positions.

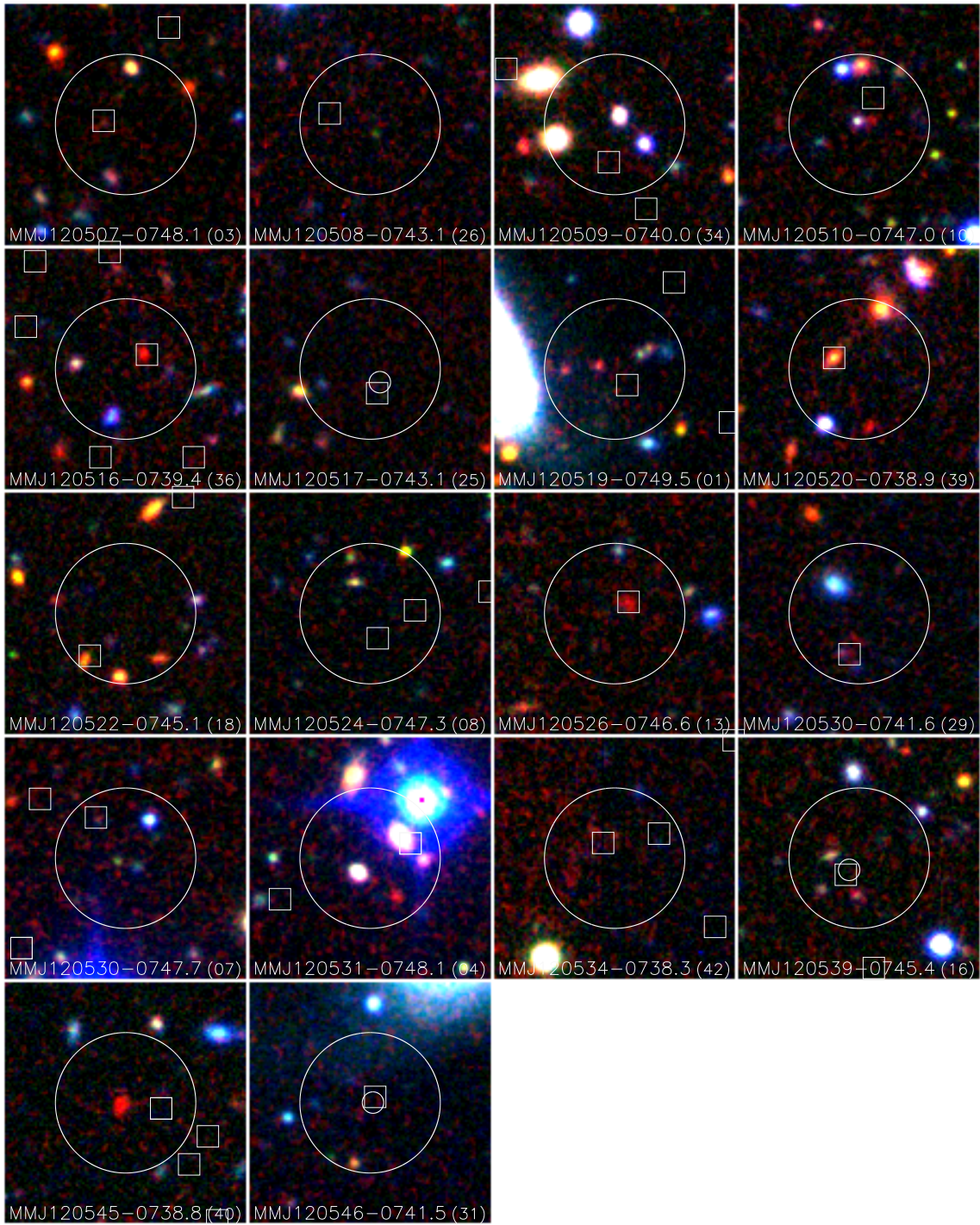


Figure 3.7 BzK color composites of the NDF MAMBO sources with interferometric positions. Large $7''$ -radius circles are drawn around the nominal MAMBO positions. VLA 1.4 GHz peaks are indicated by squares, PdBI mm interferometric sources by small circles.

algorithm *SExtractor*. From this catalog, we extracted objects near the interferometric radio position, which are presented in Tab. 3.4. We have verified the reality of objects in Table 3.4 that are fainter than the 10σ completeness limit and close to the detection limit by visual inspection of the images in the various bands. We have retained objects that are reliably detected individually in either B, z, or K, since these images are particularly deep and include the extreme wavelengths at which very blue or red objects would first be detectable. For the measurements in the individual bands, we indicate in Table 3.4 cases in which we consider the *SExtractor* aperture magnitudes more uncertain, since the object is only tentatively (indicated by “ \approx ”) or not at all (indicated by “!”) picked up by the eye in the visual inspection.

MM J120507–0748.1 (No. 03, g(ood) radio source) The faint, red counterpart 03a coincides with the $88 \mu\text{Jy}$ radio source. A $\sim 1''$ NW/SE double-peak morphology for 3a may be indicated in the K_s image but is not certain. The optical/near-IR photometric redshift $z \sim 2.1$ is consistent with the redshift estimate based on the radio-mm spectral index ($z_{CY} \sim 2.4$). The higher estimate of $z = 4.25$ from the submm/mm ratio (Eales et al., 2003) is very uncertain and consistent with these lower values within the errors.

MM J120508–0743.1 (26/ u(ncertain) radio source) A faint, uncertain radio source lies $4.6''$ from the nominal MAMBO position. No optical/near-infrared counterpart coincides with this radio source.

MM J120509–0740.0 (34/u) No optical/near-infrared counterpart is detected at the position of the faint, uncertain VLA counterpart. In the vicinity, an agglomeration of bright, normal galaxies is seen. The photometric redshifts of these objects ($z_{phot} \approx 0.4 - 0.5$) are consistent with these galaxies perhaps being part of a group. At distances of $> 4.8''$ from the interferometric position, lensing by these individual galaxies is unlikely. Similarly, such a small group is not likely to produce a strong lensing effect (e.g., Hoekstra et al., 2001). Eales et al. (2003) fail to significantly detect this object at $850 \mu\text{m}$, which is a 5σ 1.2 mm source in the MAMBO map and was seen at similar flux (but only 2.2σ) in an independent short MAMBO on-off observation (Eales et al., 2003). The very low $850 \mu\text{m}/1.2 \text{ mm}$ flux ratio, together with the nondetection of an optical/near-infrared counterpart, may suggest a very high redshift.

Table 3.4. Optical/near-infrared objects close to the interferometric positions

Source	RA (J2000)	DEC (J2000)	Sep arcsec	B mag	V mag	R mag	I mag	z mag	J mag	K mag	z_{phot}	P
(1)	(2)	(3)	(4)	(5)	(6)	(7)	(8)	(9)	(10)	(11)	(12)	(13)
03A	12:05:08.07	-07:48:11.7	0.8	≈ 27.1	> 26.5	!25.9	> 25.5	≈ 26.1	!23.3	21.48	$2.11^{+0.26}_{-0.61}$	0.030
03b	12:05:07.97	-07:48:08.7	3.7	> 27.4	> 26.5	!25.8	≈ 25.3	25.48	> 24.0	≈ 21.9	$3.64^{+0.84}_{-0.50}$	
03c	12:05:08.03	-07:48:17.5	6.1	24.93	24.49	24.11	23.42	23.94	22.00	20.36	$1.48^{+0.11}_{-0.09}$	
03d*	12:05:08.34	-07:48:16.7	6.1	> 27.4	> 26.5	≈ 25.3	≈ 25.0	> 26.4	> 24.0	> 22.0	$3.86^{+0.56}_{-0.39}$	
03e	12:05:07.89	-07:48:05.9	6.7	24.75	23.90	22.82	22.09	22.61	20.78	19.27	$0.41^{+0.03}_{-0.01}$	
26a	12:05:08.48	-07:43:02.7	4.0	≈ 26.7	!26.3	!25.3	!24.8	≈ 25.6	> 24.0	> 22.0	$0.56^{+0.13}_{-0.17}$	
26b	12:05:08.29	-07:43:05.9	5.5	!26.9	!25.6	!25.8	≈ 24.8	≈ 26.2	> 24.0	> 22.0	$2.91^{+0.31}_{-0.23}$	
26c	12:05:08.30	-07:43:07.5	5.7	!27.1	> 26.5	25.04	23.88	24.80	23.30	> 22.0	$0.67^{+0.07}_{-0.11}$	
26d	12:05:08.99	-07:43:00.2	7.3	25.22	24.97	24.22	≈ 24.6	24.50	≈ 22.6	20.96	$2.29^{+0.04}_{-0.07}$	
26e	12:05:08.51	-07:42:58.6	7.4	25.62	≈ 25.5	!25.4	> 25.5	≈ 25.7	> 24.0	> 22.0	$1.28^{+1.55}_{-0.07}$	
34a	12:05:09.51	-07:40:04.5	4.8	22.88	22.69	21.83	21.45	22.28	20.73	19.56	$0.51^{+0.02}_{-0.01}$	
34b	12:05:09.69	-07:40:01.5	5.3	23.48	22.92	21.88	21.25	21.77	20.13	18.65	$0.46^{+0.02}_{-0.01}$	
34c	12:05:10.16	-07:40:04.0	5.9	22.76	21.60	20.59	19.82	20.42	18.59	17.14	$0.40^{+0.01}_{-0.01}$	
34d	12:05:09.29	-07:40:07.0	7.6	24.92	24.59	23.56	23.02	23.63	22.19	21.03	$0.53^{+0.03}_{-0.04}$	
34e	12:05:10.33	-07:40:08.5	8.1	25.50	≈ 25.5	24.60	23.77	24.24	≈ 22.6	21.08	$1.27^{+0.06}_{-0.07}$	
10a1	12:05:10.95	-07:46:60.0	2.6	24.43	24.26	23.40	23.08	23.48	22.04	20.24	$0.54^{+0.03}_{-0.04}$	0.130
10A2	12:05:10.85	-07:47:00.0	2.4	!25.9 ^o	$\approx 25.6^o$	$\approx 25.0^o$!24.8 ^o	!25.6 ^o	> 24.0	20.58	$2.49^{+0.01}_{-0.05}$	0.136
10b	12:05:10.94	-07:46:54.0	3.6	24.41	23.92	23.29	22.56	23.04	20.65	19.17	$2.09^{+0.06}_{-0.05}$	
10c	12:05:11.06	-07:46:54.5	4.1	22.96	22.42	21.72	21.37	22.08	20.65	20.17	$0.41^{+0.01}_{-0.01}$	
10d	12:05:10.65	-07:46:54.8	4.3	25.44	25.13	24.15	23.21	23.96	22.16	20.94	$0.60^{+0.09}_{-0.07}$	
10e	12:05:10.51	-07:46:60.0	6.0	25.66	≈ 25.9	25.08	≈ 24.6	≈ 25.8	!23.5	!21.9	$0.55^{+0.16}_{-0.11}$	
36A	12:05:16.05	-07:39:25.2	0.4	!27.1	> 26.5	> 26.2	≈ 24.9	25.71	22.33	20.11	$1.70^{+0.12}_{-0.20}$	0.006
36b	12:05:15.87	-07:39:27.3	3.4	25.31	25.14	24.98	24.17	25.06	22.85	≈ 21.4	$1.55^{+0.24}_{-0.12}$	
36c	12:05:16.07	-07:39:21.0	4.6	26.40	> 26.5	> 26.2	> 25.5	> 26.4	> 24.0	> 22.0	$0.78^{+1.90}_{-0.78}$	
36d	12:05:15.62	-07:39:24.8	6.6	> 27.4	> 26.5	≈ 25.3	> 25.5	≈ 25.9	> 24.0	> 22.0	$4.04^{+0.38}_{-0.63}$	
36e	12:05:16.54	-07:39:26.5	7.2	24.65	24.63	23.72	23.11	23.40	21.41	20.19	$1.40^{+0.01}_{-0.02}$	
25A	12:05:17.89	-07:43:08.6	0.4	≈ 26.1	≈ 25.3	≈ 25.4	> 25.5	25.87	> 24.0	22.5 [•]	$2.91^{+0.12}_{-0.14}$	0.020
25b	12:05:18.24	-07:43:08.5	5.7	25.26	25.14	24.73	24.21	24.61	22.79	> 22.0	$1.41^{+0.07}_{-0.11}$	
25c	12:05:17.36	-07:43:11.2	7.8	26.22	25.90	25.02	25.11	25.90	> 24.0	> 22.0	$3.60^{+0.08}_{-0.17}$	
25d	12:05:18.40	-07:43:09.3	8.1	25.04	24.52	23.42	22.41	22.80	21.02	19.38	$0.61^{+0.03}_{-0.03}$	
25e	12:05:18.24	-07:43:14.7	8.4	25.55	25.44	24.70	23.97	24.61	22.30	20.73	$2.01^{+0.25}_{-0.59}$	
01b	12:05:20.08	-07:49:33.6	3.4	25.59 [†]	$\approx 25.5^{\dagger}$	24.49 [†]	24.63 [†]	24.96 [†]	23.28	20.31	$0.50^{+0.04}_{-0.05}$	
01c	12:05:19.74	-07:49:32.0	4.2	24.84	23.93	23.25	22.88	23.46	21.93	20.35	$0.35^{+0.01}_{-0.01}$	
39A	12:05:20.59	-07:38:55.4	0.6	25.43	25.14	24.17	22.73	23.19	20.99	19.04	$1.32^{+0.04}_{-0.01}$	0.005
39d	12:05:20.22	-07:38:55.0	6.2	26.24	> 26.5	25.17	> 25.5	25.70	≈ 23.3	> 22.0	$2.23^{+0.16}_{-0.25}$	
39e	12:05:20.66	-07:39:02.6	7.1	22.75	22.07	21.26	20.74	21.50	19.77	19.20	$0.35^{+0.20}_{-0.02}$	
39f	12:05:20.24	-07:38:49.9	8.1	24.76	24.54	23.49	22.12	22.43	20.14	18.35	$1.37^{+0.02}_{-0.01}$	0.003
18A	12:05:23.13	-07:45:14.9	0.3	≈ 26.9	> 26.5	24.87	23.34	23.59	21.56	19.61	$1.25^{+0.06}_{-0.06}$	
18b	12:05:23.30	-07:45:15.8	2.9	!27.1	≈ 26.2	≈ 25.8	!25.3	≈ 25.6	> 24.0	> 22.0	$3.10^{+0.40}_{-0.54}$	
18c	12:05:22.93	-07:45:13.0	3.2	25.75	≈ 26.3	≈ 26.1	24.37	25.38	≈ 23.4	21.40	$1.29^{+0.10}_{-0.25}$	
18d	12:05:22.88	-07:45:16.8	4.3	25.29	24.55	23.55	22.60	22.85	20.64	18.69	$2.40^{+0.03}_{-0.02}$	
18e	12:05:23.36	-07:45:11.5	4.6	≈ 26.9	> 26.5	≈ 25.1	> 25.5	≈ 26.2	> 24.0	> 22.0	$3.77^{+0.12}_{-0.23}$	
08a	12:05:24.65	-07:47:20.5	3.8	≈ 27.2	> 26.5	≈ 25.8	≈ 25.0	≈ 25.6	> 24.0	> 22.0	$0.66^{+0.20}_{-0.29}$	
08b	12:05:25.06	-07:47:19.5	5.6	> 27.4	> 26.5	> 26.2	≈ 24.8	25.58	!23.8	> 22.0	$5.25^{+0.40}_{-0.76}$	
08c	12:05:24.94	-07:47:17.6	6.3	25.18	24.66	23.91	22.89	23.45	21.81	20.48	$0.74^{+0.04}_{-0.06}$	
08d	12:05:24.30	-07:47:22.5	7.6	26.59	> 26.5	> 26.2	> 25.5	!26.0	> 24.0	> 22.0	$1.23^{+0.29}_{-0.70}$	
08e	12:05:24.75	-07:47:15.9	7.7	26.09	≈ 26.1	> 26.2	> 25.5	> 26.4	> 24.0	> 22.0	$0.91^{+0.10}_{-0.91}$	
13A	12:05:26.78	-07:46:41.0	0.5	≈ 26.5	> 26.5	!25.6	!24.9	!25.7	≈ 23.1	20.44	$2.26^{+0.21}_{-0.59}$	0.014
13c	12:05:26.96	-07:46:45.3	5.6	≈ 26.8	> 26.5	25.30	24.84	25.63	!23.4	> 22.0	$0.50^{+0.12}_{-0.50}$	
13d	12:05:26.78	-07:46:34.9	5.7	24.87	24.52	23.91	23.51	23.80	22.33	21.40	$1.36^{+0.08}_{-0.04}$	
13e	12:05:26.29	-07:46:39.4	7.1	25.17	24.90	23.66	23.11	23.77	22.21	20.99	$0.53^{+0.03}_{-0.02}$	
29A	12:05:30.26	-07:41:45.4	0.2	25.48	25.17	24.46	24.01	25.06	22.60	20.68	$2.26^{+0.10}_{-0.10}$	0.003
29b	12:05:30.17	-07:41:46.8	1.8	25.33	24.84	24.44	24.44	25.25	22.88	21.40	$2.34^{+0.07}_{-0.09}$	
29c	12:05:30.13	-07:41:44.2	2.3	!27.3	> 26.5	!25.6	> 25.5	> 26.4	> 24.0	21.23	$2.70^{+0.34}_{-0.34}$	
29d	12:05:29.91	-07:41:46.4	5.2	26.11	≈ 26.0	> 26.2	> 25.5	26.01	> 24.0	> 22.0	$1.23^{+1.69}_{-1.23}$	
29e	12:05:30.00	-07:41:51.2	6.9	26.59	≈ 26.1	≈ 25.8	24.80	25.68	≈ 23.1	> 22.0	$1.72^{+0.34}_{-0.21}$	

MM J120510–0747.0 (10/u) Near the nominal bolometer position lies a small-separation ($1.5''$) galaxy pair consisting of a fairly compact blue object (10a1) and a red object (10a2). The interferometric position of the uncertain VLA source (seen only in the background-subtracted radio image) is about $2.4''$ (1.9σ) north of 10a2 and slightly more distant from 10a1. It is thus marginally possible that one of the objects in this pair is the counterpart of the MAMBO source. Photometric redshifts suggest that the blue object is in the foreground rather than physically associated with the red object; there are no secondary solutions for the photometric redshift that would put both at the same redshift. We tentatively identify the source with object 10a2. The high photometric redshift, consistent with the radio/mm estimate, is more uncertain than its nominal error, given the faintness and the need to decompose the two components of 10a. At the observed K-band magnitude and estimated photometric redshift of 10a1, the estimated Einstein ring radius is only about $0.30''$, making strong lensing of 10a2 at $1.5''$ very unlikely. The same is true for other plausible redshifts. We note that because 10a1 appears fairly compact and blue, spectroscopic observations to look for evidence of an AGN may be worthwhile. In the case of a powerful AGN, its current photometric redshift estimate would be uncertain.

MM J120516–0739.4 (36/g) This object has the strongest radio counterpart of a NDF 1.2 mm source that coincides with a relatively bright and extremely red ($R-K > 6.0$) source. The discrepancy between the redshift estimate from the radio/mm spectral index (~ 0.8) and the photometric redshift (~ 1.7) may suggest that the radio emission is boosted by an AGN.

MM J120517–0743.1 (25/u) A faint radio counterpart is not seen in the original VLA image, but appears in the background-subtracted version. It coincides with the position determined via mm interferometry. Recently, a faint K-band counterpart (22.5 mag) at the PdBI/VLA position was detected in ultradeep imaging performed with ISAAC at the VLT. Similarly, the new z-band image indicates an extended source at the PdBI position with a maximum or companion to the southwest. In B, V, and R, very faint extended emission is suggested at the same position but only deeper imaging can confirm the reality of these structures. The photometric redshift is 2.91, in good agreement with the radio/mm redshift estimate and the mm/submm estimate of Eales et al. (2003).

Table 3.4 (cont'd)

Source	RA	DEC	Sep	B	V	R	I	z	J	K	z_{phot}	P
(1)	(J2000) (2)	(J2000) (3)	arcsec (4)	mag (5)	mag (6)	mag (7)	mag (8)	mag (9)	mag (10)	mag (11)	(12)	(13)
07a	12:05:31.01	-07:47:39.9	0.9	26.06	≈ 25.6	≈ 25.2	> 25.5	25.34	> 24.0	> 22.0	$0.35^{+0.34}_{-0.35}$	0.108
07b	12:05:31.19	-07:47:37.1	3.1	> 27.4	> 26.5	25.33	!25.2	25.61	≈ 23.3	≈ 21.9	$2.49^{+0.17}_{-0.18}$	
07c	12:05:30.87	-07:47:44.2	5.5	≈ 26.4	!26.0	24.66	23.64	24.25	22.14	21.53	$0.47^{+0.09}_{-0.47}$	
07d	12:05:31.30	-07:47:34.7	6.0	26.23	25.29	24.81	!24.9	26.05	> 24.0	> 22.0	$3.67^{+0.06}_{-0.09}$	
07e	12:05:30.64	-07:47:39.9	6.3	23.39	22.81	22.12	21.74	22.48	21.04	20.51	$0.41^{+0.01}_{-0.01}$	0.005
04a	12:05:31.17	-07:48:04.7	1.0	22.39*	21.64*	21.14*	20.27*	20.89	19.02	17.36	$0.25^{+0.03}_{-0.04}$	
04b	12:05:31.01	-07:48:07.1	2.3	23.43*	23.32*	23.23*	22.31	23.09	21.14	19.51	$1.39^{+0.06}_{-0.01}$	
04d	12:05:31.21	-07:48:11.0	5.5	25.97	!26.1	> 26.2	≈ 25.3	25.41	22.30	20.33	$1.83^{+0.01}_{-0.05}$	
04e	12:05:31.47	-07:48:08.6	5.9	23.52	22.80	21.81	21.10	21.68	20.08	18.57	$0.41^{+0.05}_{-0.02}$	
42a	12:05:34.93	-07:38:17.4	1.3	> 27.4	> 26.5	> 26.2	≈ 24.9	!25.7	!22.9	20.94	$1.52^{+0.24}_{-0.34}$	0.060
42b	12:05:34.96	-07:38:19.7	1.5	26.28	≈ 25.7	!25.4	!25.3	> 26.4	> 24.0	!21.5	$2.83^{+0.67}_{-0.24}$	0.082
42c	12:05:34.77	-07:38:17.7	2.0	> 27.4	26.24	> 26.2	> 25.5	!25.5	> 24.0	21.33	$3.10^{+0.34}_{-0.44}$	
42d	12:05:35.06	-07:38:22.0	4.2	> 27.4	> 26.5	> 26.2	!25.4	> 26.4	> 24.0	21.04	$4.21^{+0.79}_{-1.67}$	
16a	12:05:39.61	-07:45:27.9	2.3	25.54	25.30	24.85	23.63	24.32	≈ 23.8	21.11	$0.93^{+0.13}_{-0.08}$	
16b	12:05:39.35	-07:45:28.7	2.4	25.47	25.27	24.78	23.88	24.95	22.21	20.50	$1.70^{+0.19}_{-0.12}$	
16c	12:05:39.54	-07:45:24.3	2.9	25.20	24.58	23.59	23.06	23.59	21.97	20.45	$0.46^{+0.02}_{-0.02}$	
16d	12:05:39.19	-07:45:22.7	6.0	26.21	≈ 26.3	≈ 26.0	24.62	25.16	≈ 23.5	≈ 21.9	$1.13^{+0.26}_{-0.17}$	
16e	12:05:39.93	-07:45:25.0	7.1	26.05	!26.4	≈ 25.4	≈ 25.0	25.65	> 24.0	> 22.0	$0.58^{+0.18}_{-0.10}$	
40a	12:05:45.69	-07:38:50.5	2.1	26.33	≈ 26.1	≈ 25.9	!25.0	!26.1	!23.7	!21.7	$1.61^{+0.92}_{-0.25}$	0.168
40b	12:05:45.98	-07:38:51.8	3.9	> 27.4	> 26.5	> 26.2	!25.3	≈ 25.8	22.19	19.57	$1.52^{+1.24}_{-0.25}$	
40c	12:05:45.55	-07:38:48.4	4.8	≈ 26.7	> 26.5	≈ 25.2	!25.2	25.40	> 24.0	> 22.0	$0.54^{+0.09}_{-0.10}$	
40d	12:05:45.69	-07:38:59.1	6.6	25.24	24.63	23.92	23.60	23.99	!23.2	21.41	$3.41^{+0.05}_{-0.08}$	
31a	12:05:46.69	-07:41:30.3	4.3	25.80	25.04	≈ 24.8	≈ 23.8	25.12	!23.6	≈ 21.8	$2.87^{+0.11}_{-0.17}$	
31b	12:05:46.94	-07:41:33.3	5.3	25.52	25.70	25.33	≈ 24.7	25.08	≈ 23.1	> 22.0	$1.35^{+0.15}_{-0.08}$	
31c	12:05:46.65	-07:41:39.5	5.3	25.72	25.23	24.48	23.30	23.75	22.29	20.37	$1.11^{+0.05}_{-0.03}$	
31d	12:05:46.82	-07:41:38.9	5.7	≈ 26.8	> 26.5	25.01	23.82	24.58	≈ 23.0	> 22.0	$0.70^{+0.09}_{-0.08}$	

Note. — Col. (1) — Optical/near-infrared source identification. Counterparts to mm sources are marked in bold face with a capital letter.
Col. (2-3) — J2000 coordinates of optical/near-infrared source.

Col. (4) — Separation between optical position and best interferometric position.

Col. (5-11) — Source magnitudes in a $2''$ aperture. All magnitudes are on the Vega system except for the z magnitudes which are on the BD system. \approx : Detection is tentative. !: Source is not reliable but aperture magnitude measured by *SExtractor*.

Col. (12) — Photometric redshift.

Col. (13) — Probability of a chance coincidence with an object of the given K magnitude at the given separation.

o: magnitude contaminated by 10a1.

●: Detected with ISAAC at the VLT (Lehnert et al. 2004, in preparation).

†: magnitude contaminated by nearby foreground galaxy.

*: magnitude contaminated by nearby star.

★: 03d is not detected in one of our three priority bands — B, z and K — but its R and I detections look reliable; thus it is not removed from the original source catalog.

MM J120519–0749.5 (01/g) Among the “blank-field” sources not showing an optical/NIR counterpart within 2σ of the interferometric position, this is the blank-field object with the strongest radio counterpart that is also a secure radio source ($72 \mu\text{Jy}$). Eales et al. (2003) report a 4.3σ $850 \mu\text{m}$ detection of this object, and infer a low $850 \mu\text{m}/1.2 \text{ mm}$ flux ratio. This suggests a very high redshift which under the SED assumptions is marginally consistent with the radio/mm redshift estimate. The objects a, d, and e, which are marginally detected by *SExtractor*, seem to be due to noise or structure in the extended emission from the large foreground object and were not included in Table 3.4.

MM J120520–0738.9 (39/g) The radio counterpart is the second strongest in our sample and coincides with an extremely red object ERO ($R-K = 5.2$). In the K band, it shows weak NW/SE extensions, with possible variations at shorter wavelengths. The high-quality photometric redshift (1.32) and the radio/mm estimate agree well, placing the object near the low end of the redshift distribution of our mm sources. Object 39f, $7.6''$ to the northwest, has a very similar photometric redshift.

MM J120522–0745.1 (18/g) The bright radio source which is $6''$ southwest from the nominal bolometer position coincides with an elongated moderate photometric redshift ERO ($R-K = 5.3$), here we adopt it as the counterpart of the MAMBO source, noting the relatively large positional offset.

MM J120524–0747.3 (08/u) Two faint and uncertain radio sources lie within the MAMBO beam. Both are blank fields in the optical/near-infrared. We adopt the μJy radio source closer to the nominal MAMBO position but consider the chance of a misidentification to be significant, both as a result of the radio sources being uncertain and the difficulty of deciding between them (Neri et al., 2003, cf. also the case of SMM09431+4700).

MM J120526–0746.6 (13/g) A faint radio source from a good region of the VLA image coincides with an ERO ($R-K = 5.4$). The K morphology appears distorted/curved. Both photometric redshift and radio/mm spectral index put the source at $z \approx 2.5$. This counterpart has a very large J–K (and z–K) color; we discuss this in § 3.3.1.

MM J120530–0741.6 (29/g) The interferometric position of the strong $85 \mu\text{Jy}$ radio source is in a group of three objects. Object 29a, coincident with the radio position, is a

very red object with $I-K = 3.3$ according to Ivison et al. (2002). At $1.5''$ to the southwest there is a bluer source 29b, and $1.5''$ to the northwest from 29a the extremely red object 29c ($I-K > 4.3$). The photometric redshifts of the three objects are consistent with all being at $z \sim 2.4$, in reasonable agreement with the radio/mm estimate of ~ 1.8 . The three objects could be physically associated, with separations (for a redshift of ≈ 2) between about 13 and 23 kpc. We nominally identify the MAMBO source with 29a, but note that all three objects are part of a complex structure with strongly varying colors reflecting different obscurations, a unique object in our sample.

MM J120530–0747.7 (07/u) A faint blue object coincides with a faint, uncertain radio source close to the edge of the search circle.² It is the only candidate counterpart that is not detected in the K band and is the bluest in our sample. The photometric redshift of 0.35 grossly differs from the radio/mm estimate (~ 2.8), raising the possibility of an incorrect identification of a foreground dwarf. The low mass of the relatively faint foreground object ($M_K \gtrsim -19$) makes a lensing effect less likely. The probability of ~ 0.1 for a chance coincidence (in this case based on the B magnitude and the B counts of Pozzetti et al., 1998) is consistent with finding such a case in our sample.

MM J120531–0748.1 (04/u) The identification in the optical/near-infrared is not obvious. The faint and uncertain radio source is $4.4''$ from the nominal MAMBO position, behind and $1.0''$ from the center of an extended optical/near-infrared bright source (04a) with a photometric redshift estimate of 0.25. This is far below the radio/mm estimate. Galaxy-galaxy lensing could hence play a significant role in MM J120531-0748.1 — the radio position and the closest position on the estimated Einstein ring differ by less than 1σ of the radio positional error. The putative lensed object must have $K \gtrsim 18$. The morphology could be similar to that of SMM J04431+0210 (Smail et al., 1999; Frayer et al., 2003), but with a smaller separation making strong lensing more likely.

MM J120534–0738.3 (42/g) This is the second of two cases in which two radio sources are detected within our search radius. The identification of the radio counterpart seems relatively clear, however, since a robust brighter radio source is only $2.1''$ from the MAMBO position while the second is more distant ($5.5''$) and is both fainter and

²At the chosen scaling when making the color images, the red channel appears noisier than the blue and green channels. Thus, we see enhanced “red” noise in the color image.

of uncertain reliability. We adopt the first one, which is located inside a group of three faint objects (42a-c) that are $1.3 - 2.0''$ (1.6 to 3σ) from the radio position. An identification with 42a ($z_{phot} = 1.52_{-0.34}^{+0.24}$) or 42b ($z_{phot} = 2.83_{-0.24}^{+0.67}$) is possible; the radio/mm redshift estimate ($z_{CY} \sim 2.1$) is consistent with the photometric redshifts of either source. We adopt in the following an identification with the closest object 42a but consider an identification with b (or a blank field) possible. Source No. 42 appears extended in the MAMBO map; the peak flux (Tab. 3.3) thus underestimates the total flux. The source is in a border region between two K-band fields which may affect the quality of the K image and the photometric redshifts.

MM J120539–0745.4 (16/u) While the radio counterpart is faint, its position is confirmed by the PdBI mm detection whose coordinates we adopt as the best position. It is still a blank field in deeper images ($K > 22.7$ mag; see § 3.1 for detailed discussion).³

MM J120545–0738.8 (40/u) A $40 \mu\text{Jy}$ uncertain radio source is located $3.9''$ west of the nominal bolometer position. The faint object 40a is within 1.6σ of the radio positional error from the radio position. Directly at the MAMBO position and 4σ from the radio peak, however, a compact elliptically shaped extremely red object (40b) with a photometric redshift $z=1.52_{-0.25}^{+1.24}$ and a best-fitting burstlike SED is seen. An identification with this object may also be possible because its radio/mm index could still be consistent with the suggested photometric redshift range, given the noise level of the VLA map. The observed radio peak would then be unrelated. Additional MAMBO on-off observations in winter 2001/2002 could not conclusively resolve this ambiguity but showed the strongest signal at the position of the ERO. Only deeper radio interferometry or mm-interferometry can clarify this ambiguity; in the following we adopt an identification with the ERO which is another high J–K object.

MM J120546–0741.5 (31/g) This source is a blank field at the depth of the images presented here. In deep VLT imaging a K-band counterpart ($K_s = 21.9$ mag) is detected (see § 3.1 for more detail). Eales et al. (2003) detect the source at $850 \mu\text{m}$ and suggest a submm/mm redshift estimate consistent with the radio/mm estimate or with significantly higher redshifts.

³The noise peaks in the K band seen in the color image are due to overlapping regions between two separate pointings in our K-band mosaic.

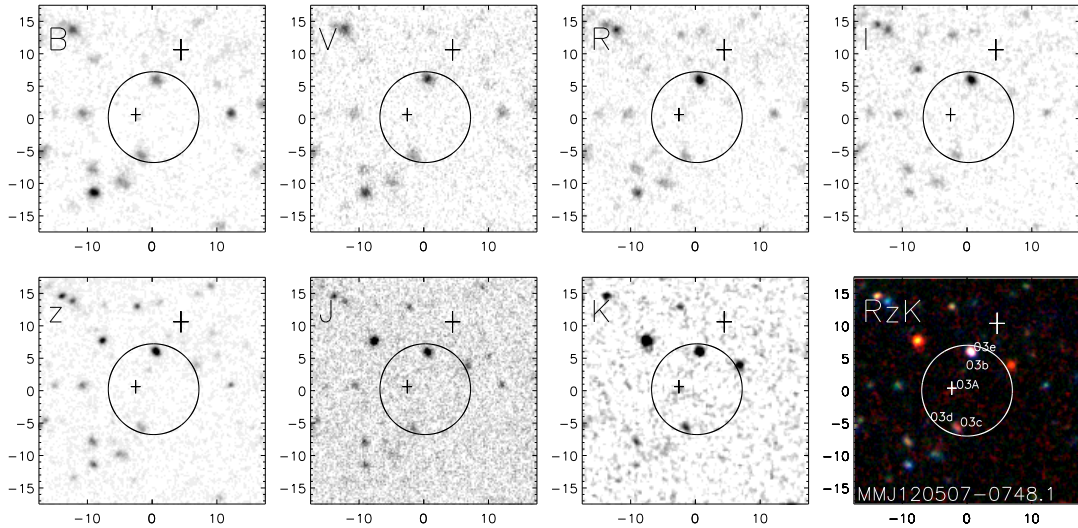


Figure 3.8 B, V, R, I, z, J and K images and RZK color composite for the field of MM J120507–0748.1. The counterpart of this 1.2 mm galaxy is 03A. Each image is $35'' \times 35''$ and oriented such that north is at the top and east is to the left. Large $7''$ -radius circles are drawn around the nominal MAMBO positions. Small crosses indicate the position and 2σ errors of the PdBI detection, and the larger crosses indicates the positions and 2σ errors obtained from VLA 1.4 GHz interferometry. In the RZK color composite, the PdBI mm interferometric sources are indicated by small circles.

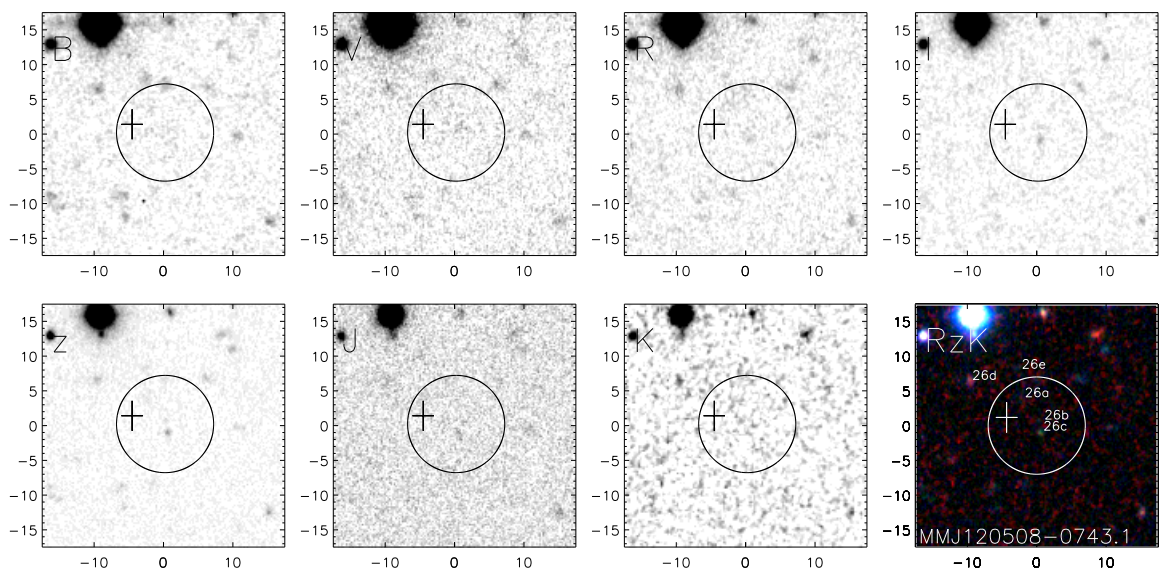


Figure 3.9 MM J120508–0743.1 is a blank field in the optical/near-infrared.

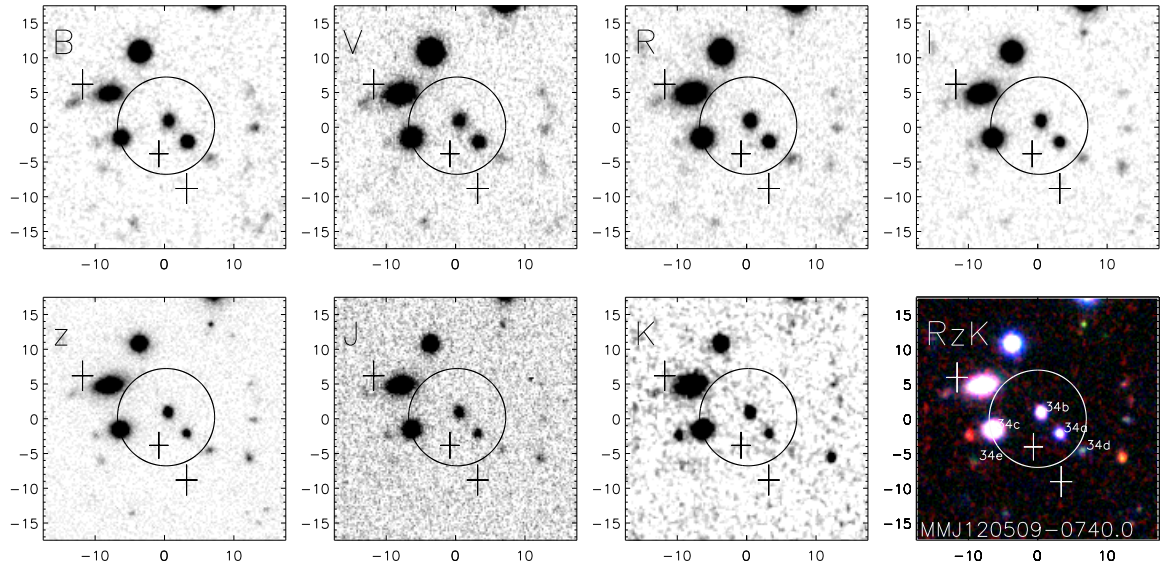


Figure 3.10 MM J120508–0740.1 is a blank field in the optical/near-infrared.

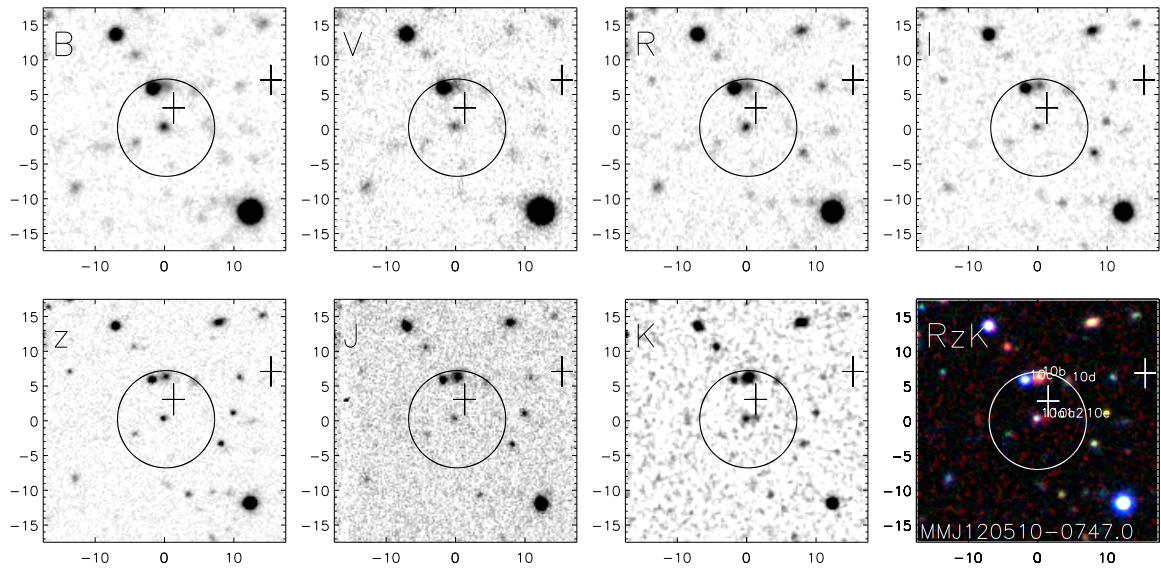


Figure 3.11 MM J120510–0747.0: Object 10A2 is tentatively identified as the origin of the mm emission.

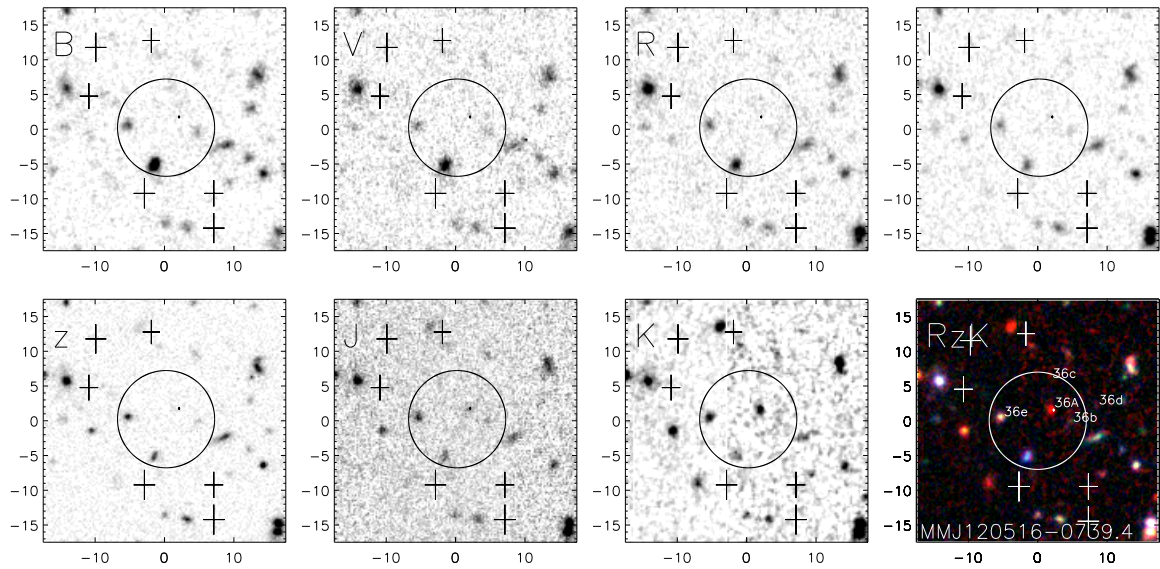


Figure 3.12 MM J120516–0739.4: ERO 36A is the counterpart of this 1.2 mm source.

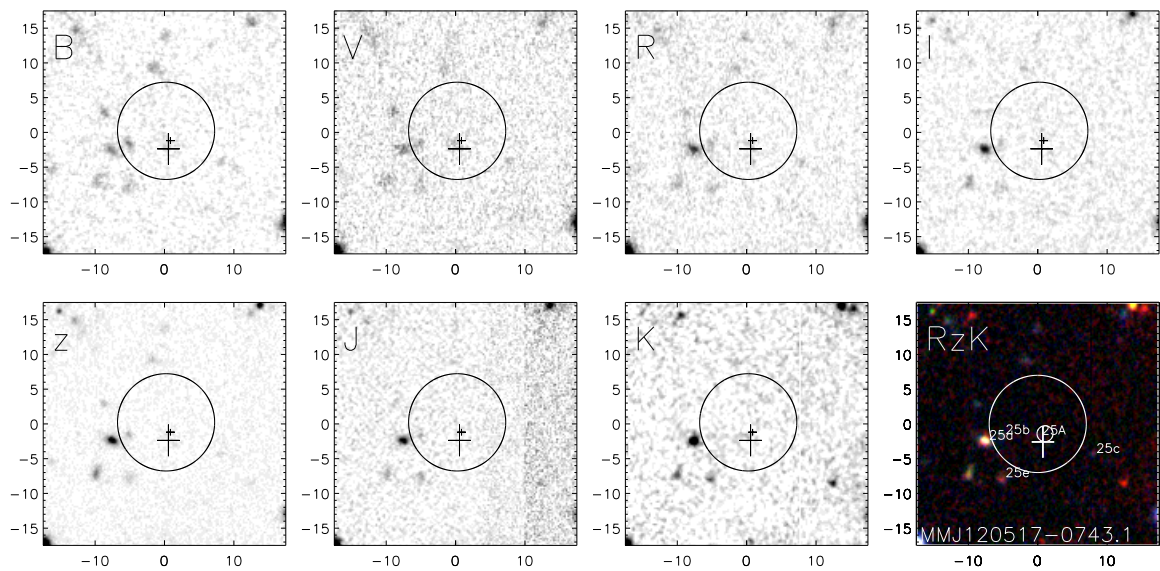


Figure 3.13 MM J120517–0743.1: Faint K-band counterpart (25A) is detected in VLT imaging.

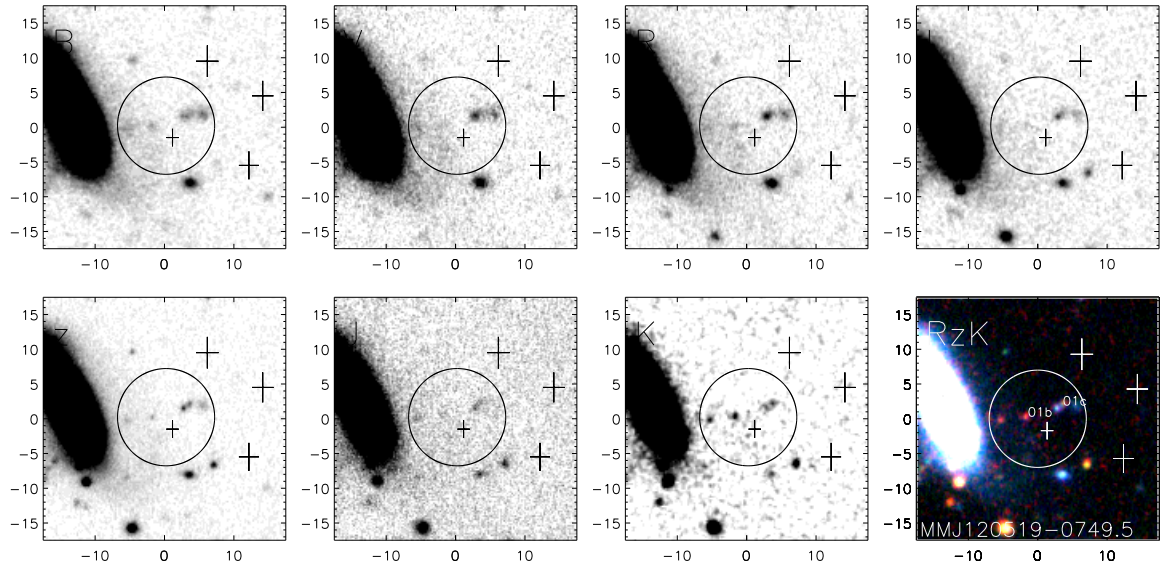


Figure 3.14 MM J120519–0749.5: Blank field.

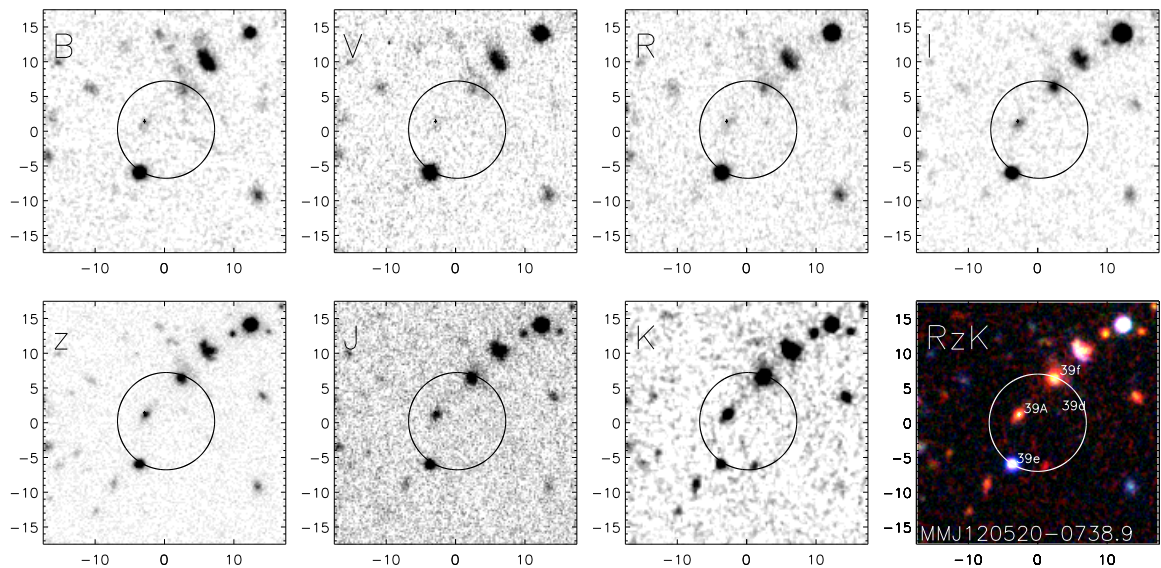


Figure 3.15 MM J120520–0738.9: The ERO 39A is the counterpart.

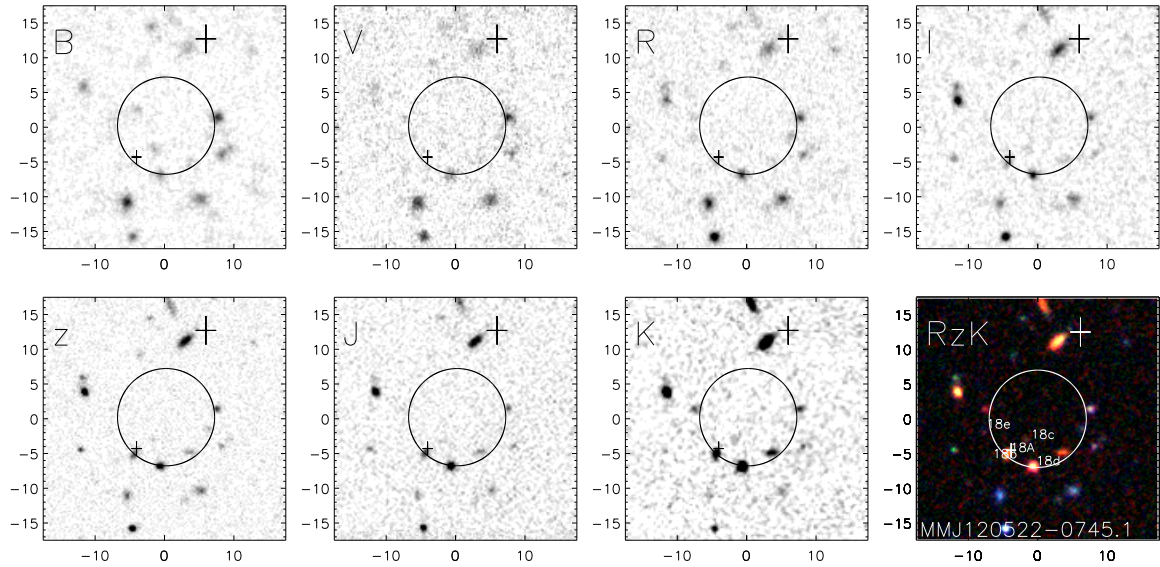


Figure 3.16 MM J120522–0745.1: We adopt object 18A as the counterpart, but note the relatively large offset.

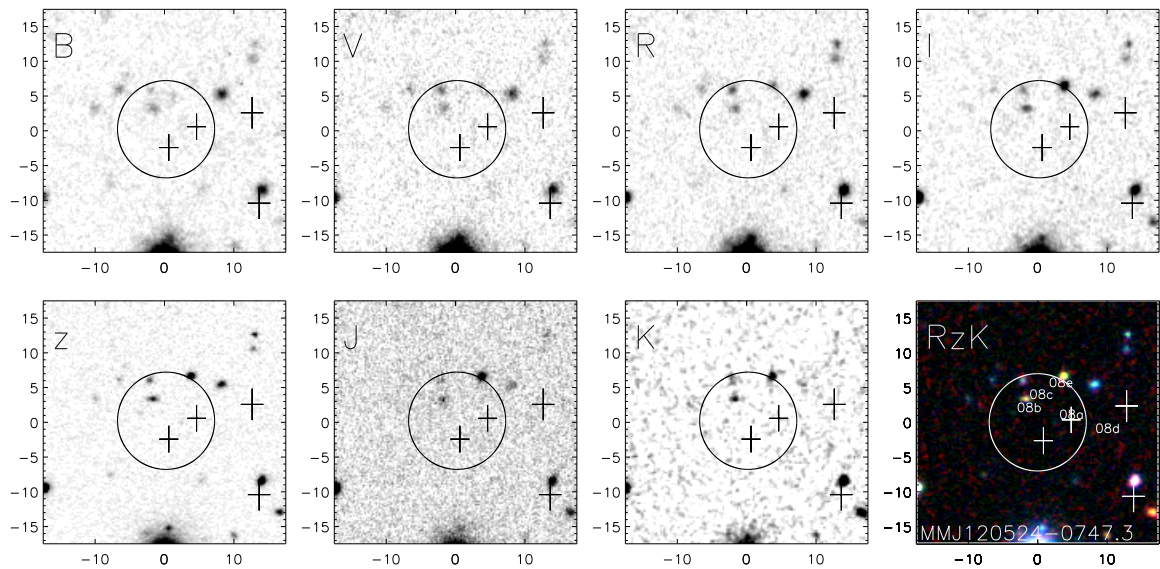


Figure 3.17 MM J120524–0747.3: The radio source closer to the nominal MAMBO position is adopted as the counterpart and is a blank field in the optical/near-infrared.

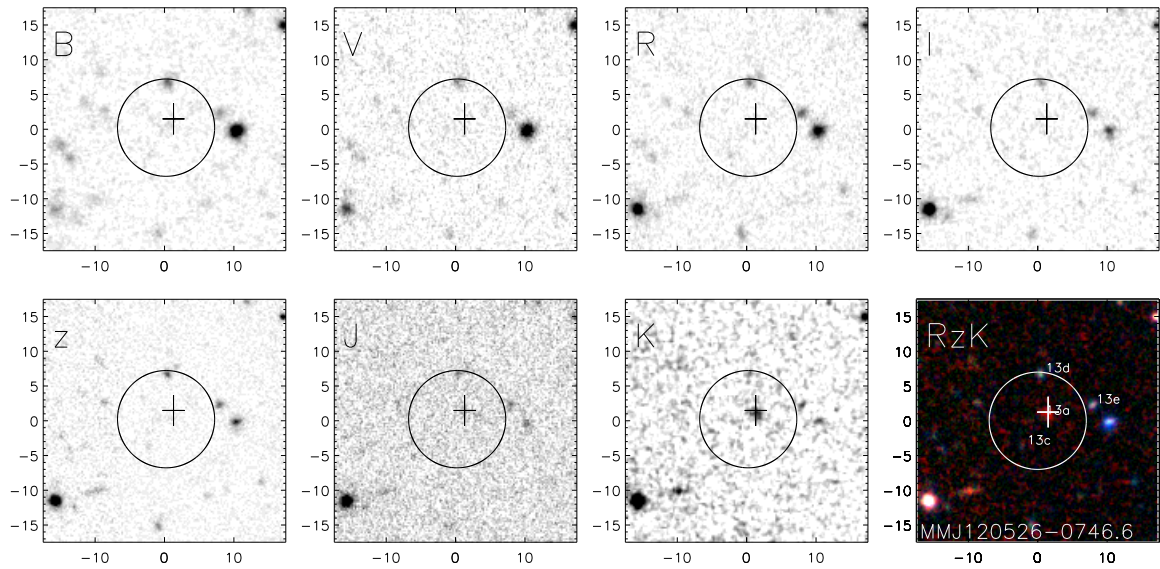


Figure 3.18 MM J120526–0746.6: Distorted ERO 13A is the counterpart of this MAMBO galaxy.

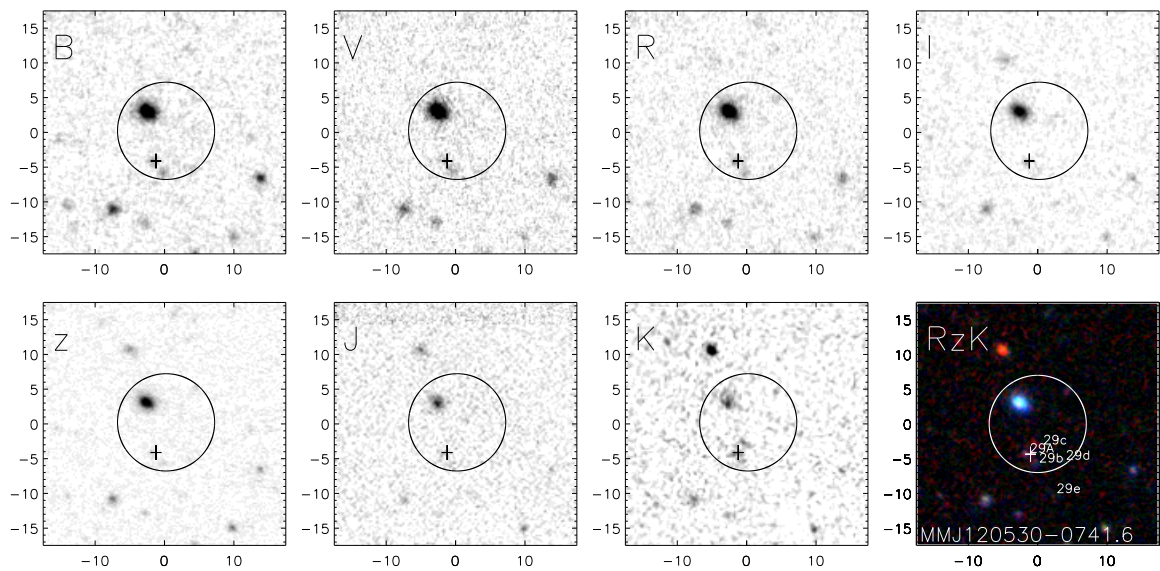


Figure 3.19 MM J120530–0741.6: The three objects 29A, 29b and 29c may be physically associated. We adopt 29A as the mm emitter.

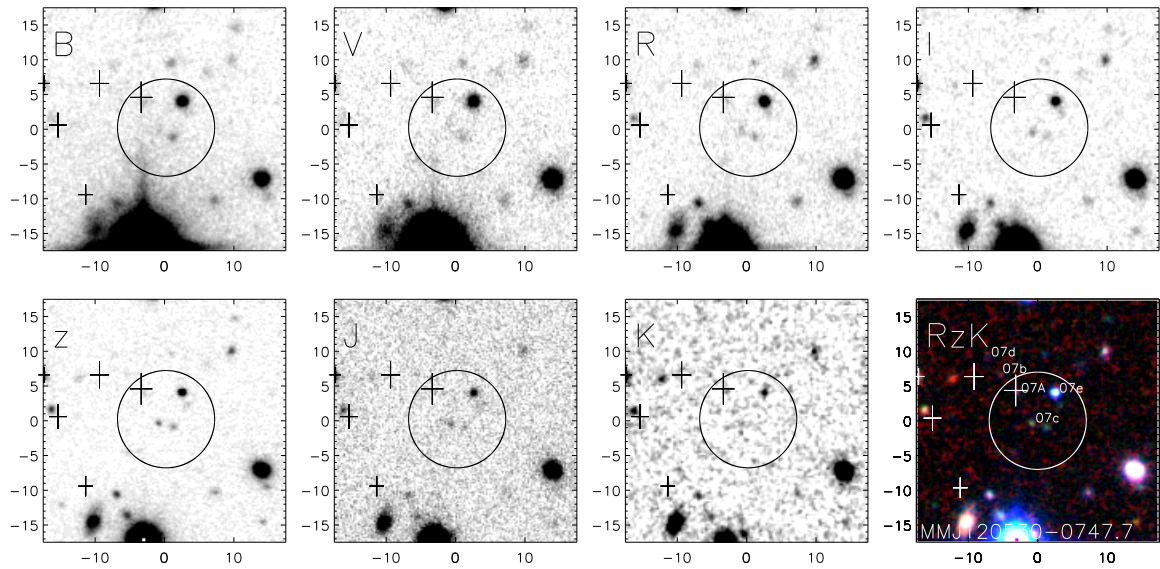


Figure 3.20 MM J120530–0747.7: Discrepant optical/NIR and radio/mm photometric redshift estimates suggest that the blue object 07A is not the mm counterpart.

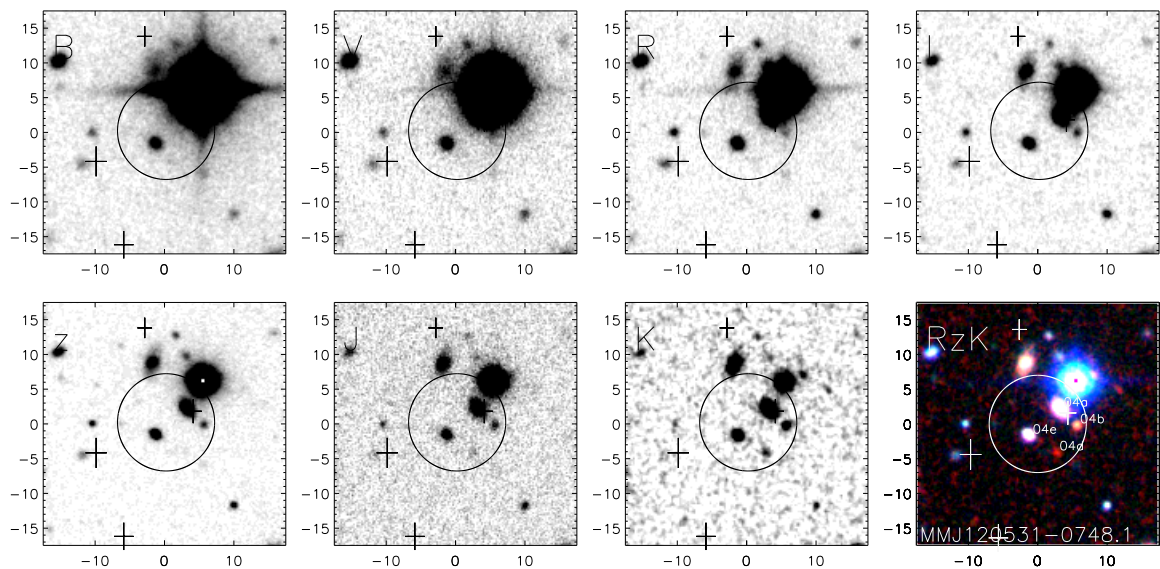


Figure 3.21 MM J120531–0748.1: Lensing by 04a probably plays a significant role and therefore the putative lensed object must be $K \geq 18$ mag.

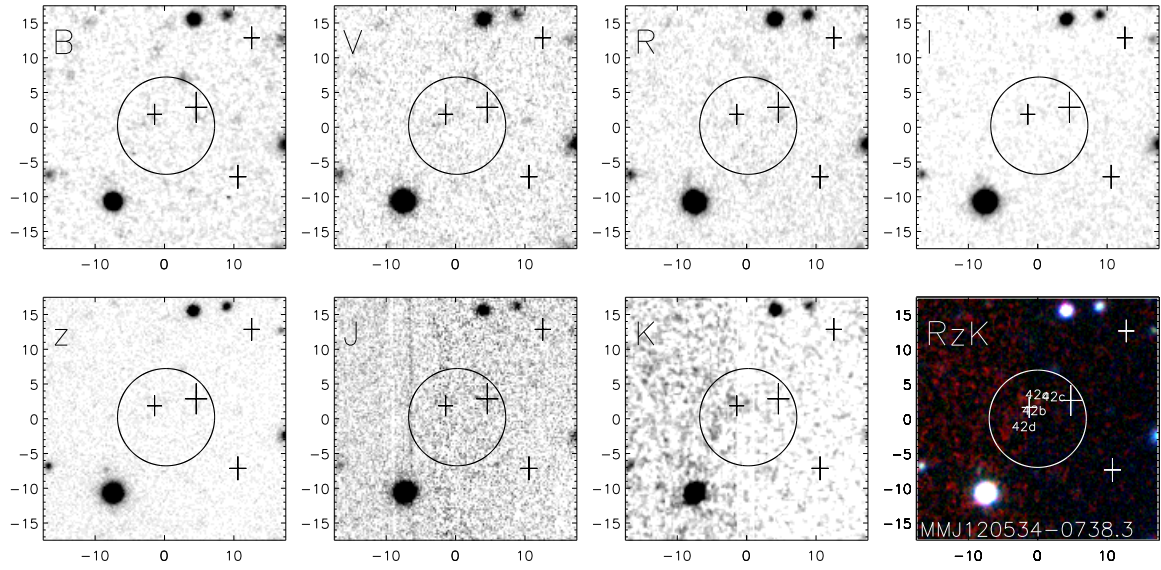


Figure 3.22 MM J120534-0738.3: Object 42A is proposed as the counterpart in the optical/near-infrared.

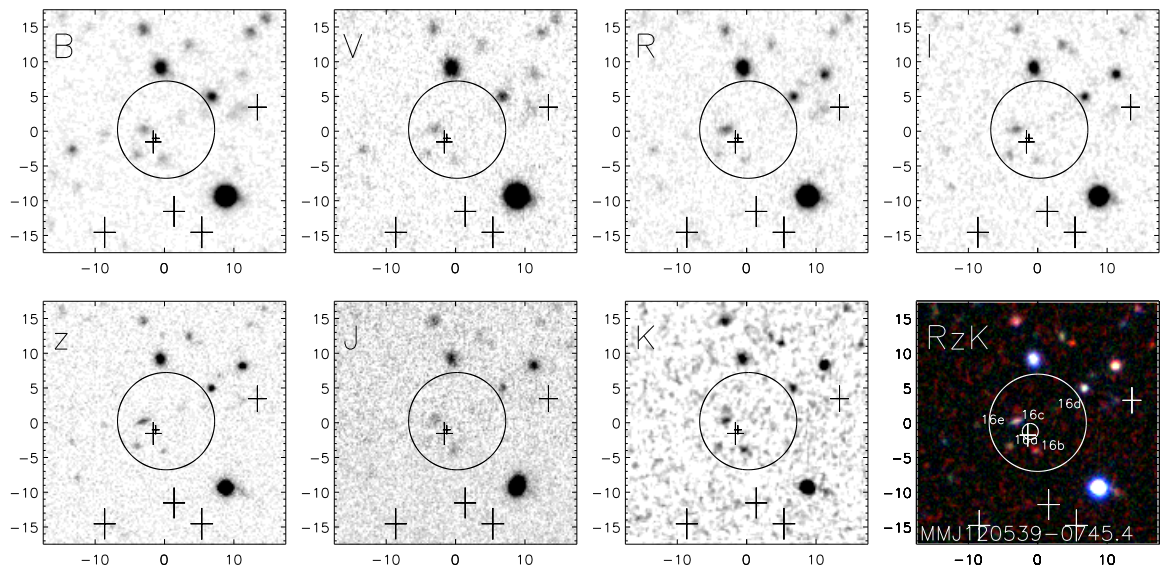


Figure 3.23 MM J120539-0745.4: Blank field.

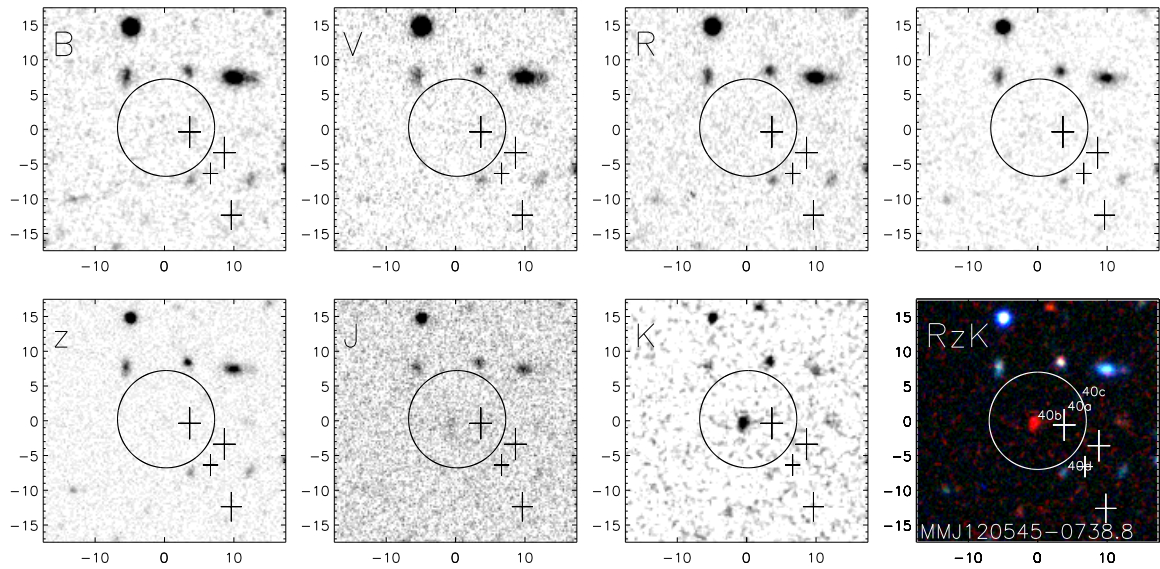


Figure 3.24 MM J120545–0738.8: We tentatively identify the MAMBO source with the ERO 40b. The radio source could be unrelated.

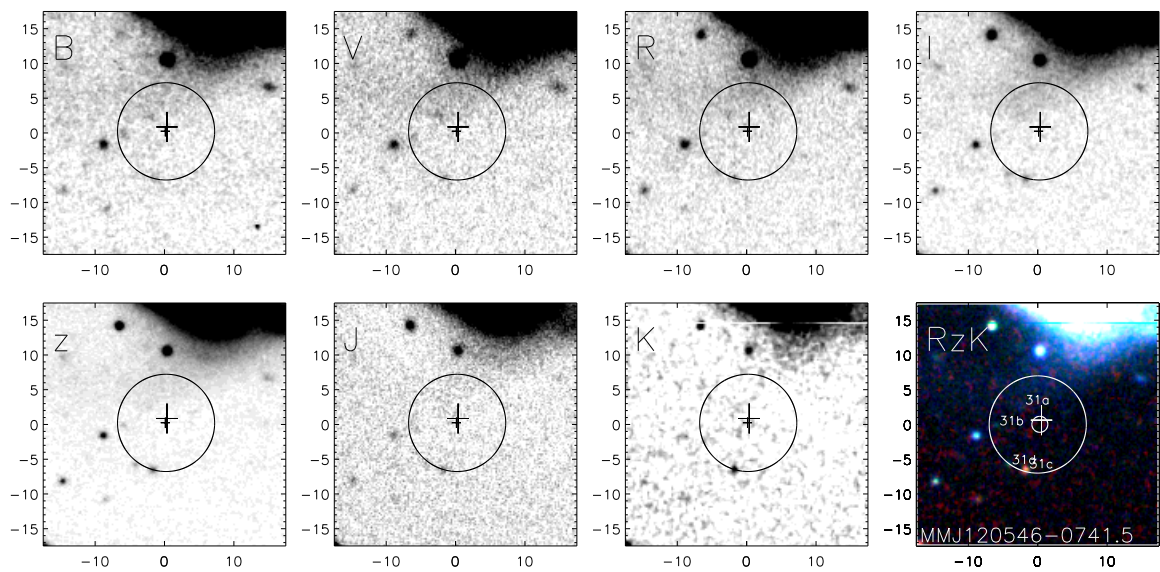


Figure 3.25 MM J120546–0741.5: K-band counterpart successfully detected in ultradeep K-band imaging at the PdBI position.

Table 3.5. Main properties of counterparts to MAMBO Sources

Source	No	Q	$S_{1.2\text{ mm}}$ mJy	$S_{1.4\text{ GHz}}$ μ Jy	K mag	z_{CY}	z_{phot}	$z_{submm/mm}$
(1)	(2)	(3)	(4)	(5)	(6)	(7)	(8)	(9)
MM J120507–0748.1	03	g	4.6	88	21.48	$2.38^{+1.19}_{-0.76}$	$2.11^{+0.26}_{-0.61}$	$4.25^{+\infty}_{-4.25}$
MM J120508–0743.1	26	u	2.7	42	>22.0	$2.64^{+1.55}_{-0.95}$		
MM J120509–0740.0	34	u	3.3	47	>22.0	$2.73^{+1.49}_{-0.91}$		(see note)
MM J120510–0747.0	10	u	3.1	41	20.58	$2.82^{+1.74}_{-1.00}$	$2.49^{+0.01}_{-0.05}$	
MM J120516–0739.5	36	g	2.2	459	20.11	$0.83^{+0.42}_{-0.34}$	$1.70^{+0.12}_{-0.20}$	
MM J120517–0743.1	25	g	4.3	40	22.50	$3.27^{+2.07}_{-1.08}$	$2.91^{+0.12}_{-0.14}$	$3.65^{+4.26}_{-2.53}$
MM J120519–0749.5	01	g	5.2	72	>22.0	$2.74^{+1.41}_{-0.87}$		>8.95
MM J120520–0738.9	39	g	2.7	336	19.04	$1.05^{+0.50}_{-0.39}$	$1.32^{+0.04}_{-0.01}$	
MM J120522–0745.1	18	g	2.0	90	19.61	$1.67^{+0.79}_{-0.58}$	$1.25^{+0.06}_{-0.06}$	
MM J120524–0747.3	08	u	2.0	47	>22.0	$2.21^{+1.25}_{-0.79}$		
MM J120526–0746.6	13	g	2.6	41	20.44	$2.62^{+1.54}_{-0.92}$	$2.26^{+0.21}_{-0.59}$	
MM J120530–0741.6	29	g	2.3	85	20.68	$1.82^{+0.88}_{-0.63}$	$2.26^{+0.10}_{-0.10}$	
MM J120530–0747.7	07	u	3.0	40	>22.0	$2.82^{+1.77}_{-1.00}$	$(0.35^{+0.34}_{-0.35})$	
MM J120531–0748.1	04	u	2.7	53	>18.0	$2.37^{+1.32}_{-0.86}$	$(0.25^{+0.03}_{-0.04})$	
MM J120534–0738.3	42	g	2.2	61	20.94	$2.05^{+1.14}_{-0.79}$	$1.52^{+0.24}_{-0.34}$	
MM J120539–0745.4	16	g	3.4	55	>22.7	$2.56^{+1.37}_{-0.84}$		$6.35^{+\infty}_{-4.85}$
MM J120545–0738.8	40	u	3.7	40	19.57	$3.05^{+1.97}_{-1.04}$	$1.52^{+1.24}_{-0.25}$	
MM Jy120546–0741.5	31	g	6.5	42	21.90	$3.86^{+2.58}_{-1.31}$		$5.25^{+6.14}_{-1.93}$

Note. — Col. (1) — MAMBO source.

Col. (2) — Short number on the original MAMBO NDF source list.

Col. (3) — Quality of the interferometric identification. g(ood) stands for objects with a good quality VLA source or a PdBI identification.

Col. (4) — MAMBO 1.2 mm flux density.

Col. (5) — VLA 1.4 GHz peak flux density.

Col. (6) — K magnitude (Vega), see Table 3.4 for other bands. For MM J120519–0749.5 and MM J120531–0748.1, we give K-band limits, as we assume that the foreground objects detected at the radio position are not linked to the dust emission.

Col. (7) — Redshift estimate from radio/mm spectral index (Carilli & Yun, 2000). Errors reflect 1σ uncertainties in alpha due to measurement errors and due to the intrinsic scatter of the relation, added in quadrature.

Col. (8) — Photometric redshift from optical/near-infrared photometry. Values in brackets refer to objects — MM J120519–0749.5 and MM J120531–0748.1 — that are likely in the foreground.

Col. (9) — Redshift estimate from the 1200 μ m/850 μ m flux ratio as derived by Eales et al. (2003). No. 34 was observed but the flux ratio could not be fit by the template used at any redshift.

3.3 Discussion

3.3.1 Optical/Near-infrared Properties: Very Faint Counterparts

The counterparts detected for the NDF mm sources are on average faint, even compared with published values for submm galaxies. This is illustrated in Fig. 3.26, which shows the distributions of I- and K-band magnitudes and limits for our sample as well as for three literature samples of submm sources that have these magnitudes available for identifications obtained with the help of radio or mm interferometry. For consistency

with our sample, we did not consider from those papers the more unreliable identifications solely based on the bolometer survey positions. The first of these surveys is the SCUBA 8 mJy survey (Scott et al., 2002; Fox et al., 2002; Ivison et al., 2002), which, for plausible assumptions about the redshift and SED of the objects, should be roughly similar in depth to our data. The median submm flux of the radio-identified 8 mJy sources is $S_{850\mu\text{m}} \sim 8.3$ mJy, while the median mm flux of our radio-identified sources is $S_{1.2\text{mm}} \sim 3.0$ mJy. This ratio ~ 2.8 of 850 μm and 1.2 mm fluxes is consistent with $z \sim 3$ ULIRG-like SEDs. We have augmented data for the second sample, the SCUBA cluster lens survey (SCLS; Smail et al., 2002a, and references therein; down to 4.5–6.6 mJy (3σ) at 850 μm), with two more objects behind one of their clusters detected by Cowie, Barger, & Kneib (2002) and discussed by Ledlow et al. (2002). For one of these we adopt the revised identification of Neri et al. (2003). Finally, we use magnitudes from the CUDSS survey (down to a 3σ level of ~ 3.5 mJy at 850 μm), for radio-identified objects in the 3h field (Webb et al., 2003b) and for the object studied by Gear et al. (2000). The latter two surveys differ more from our survey in strategy (cluster lens) or depth (CUDSS) but may still serve for comparisons.

As shown in Fig. 3.26, the NDF mm sources are significantly fainter in both K and I. Taking the median of the observed magnitudes or limits, we find $K \sim 21.5$ mag and $I \sim 25.5$ mag for the mm objects versus $K \sim 19.6$ mag and $I \sim 23.3$ mag for the identifications from the 8 mJy survey. The cluster lens and CUDSS objects have smaller statistics but are intermediate. Eliminating all those NDF identifications based on radio sources that we considered more uncertain above does not change the values strongly — the median of the remaining objects is $K \sim 20.9$ mag and $I \sim 24.9$ mag; i.e. the counterparts of the MAMBO sources are about 2 magnitudes fainter on average than those in the 8 mJy 850 μm survey. One major difference between the two populations is the absence in our sample of bright $K \sim 18$ counterparts, of which several are found in the 8 mJy survey.⁴ The trivial explanation of such a difference, in which our sample just represents much fainter members of the same population, is clearly inconsistent with the depths and areas of the various surveys. Smail et al. (2002a) claimed to see an empirical relation

⁴We note that the different aperture sizes have been used in making this comparison. For example, Ivison et al. (2002) use a 4'' diameter aperture to estimate their fluxes while we used 2'' apertures. In sources with complex extended morphologies or nearby objects, the larger apertures could lead to systematically brighter magnitudes. However, it seems unlikely that this alone could lead to an offset of 2 mag.

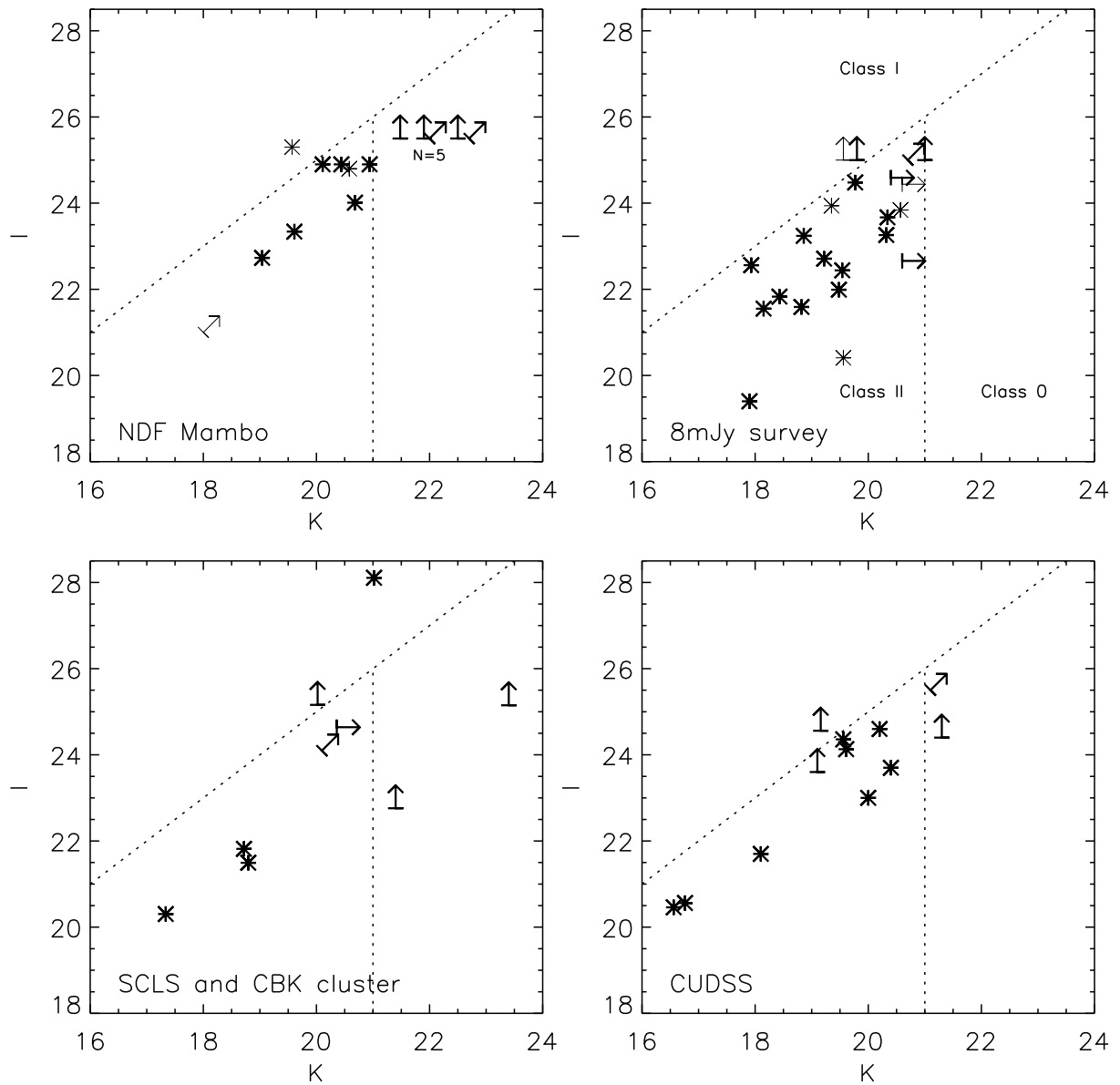


Figure 3.26 Distribution of K and I magnitudes for the interferometrically located NDF 1.2 mm objects and for three samples of interferometrically located SCUBA 850 μm galaxies. The limit symbol at $K > 22$ mag, $I > 25.5$ mag in the NDF panel represents five objects. In the panel for the 8 mJy survey, we indicate the regions occupied in this type of diagram by the class 0/I/II objects according to the definition used by Ivison et al. (2002). In the top two panels thick symbols reflect identifications described as good/robust. Magnitudes for the cluster lens sources have been corrected for the magnifications stated in the original papers.

between the K band and the submm flux (the fainter in the submm the fainter in the K band). We do not see such a trend in our sample for bright mm sources being brighter in K (see Fig. 3.27), as possibly present in the SCUBA cluster lens survey (Smail et al., 2002a). Recently, De Breuck et al. (2004) observed the environment of the $z = 4.11$ radio galaxy TN J1338-1942⁵ (De Breuck et al., 1999a,b) with MAMBO at 1.2 mm. Again, optical faintness of MAMBO 1.2 mm sources is reported.

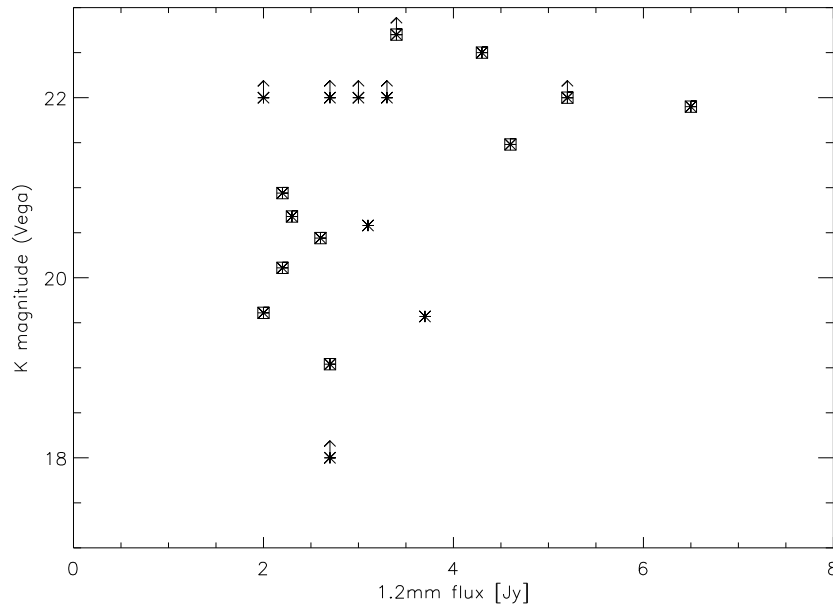


Figure 3.27 MAMBO 1.2 mm map flux versus K-band magnitude for 18 radio-identified NDF galaxies. No trend is apparent. Reliable radio sources are marked by boxes.

Ivison et al. (2000b) introduced a classification scheme (Class 0,I,II) for (sub)mm galaxies based on their optical/near-infrared properties, as a means of representing possible evolutionary phases of a (sub)mm galaxy. Ivison et al. (2002) redefined this scheme: Class 0 (sub)mm galaxies are undetected in K down to $K \sim 21$ mag, and if detected in K, $(I-K) < 5$; Class I sources are EROs detected in K ($(I-K) > 5$); and Class II sources are optically bright galaxies detected in K down to $K < 21$ with $(I-K) < 5$. Adopting these definitions, we divide the (sub)mm galaxies into the different classes. For this analysis, we define a sample that includes only (sub)mm galaxies reliably located that are published via blank-field surveys and gravitational-lens-assisted surveys. A key

⁵Venemans et al. (2002) detected a (proto)cluster around this radio galaxy.

aspect for such a comparison is the criteria used for identification. We consider as reliably located those objects with available optical and near-infrared follow-up observations that are either (1) detected with mm interferometry, which directly probes the (sub)mm dust emission (13 objects including the four MAMBO 1.2 mm galaxies identified by the PdBI), or (2) detected at $> 5\sigma$ in the (sub)mm and located through radio interferometry. Radio identification is possible through the tight radio-far-infrared correlation for star-forming galaxies but can have problems, as demonstrated in the case of the identification of HDF850.1 (Downes et al., 1999; Dunlop et al., 2002, detection of even fainter radio source than the assumed radio counterpart within the PdBI position uncertainties) and of SMM J09431+4700 (Ledlow et al., 2002; Neri et al., 2003, two faint μJy sources within the SCUBA beam). We restrict radio identification here to sources detected in the (sub)mm at a 5σ level, in order to limit contamination by galaxies with (sub)mm fluxes that are highly uncertain because of Malmquist bias in the (sub)mm surveys. We do not consider objects from radio-preselected surveys (e.g., Barger et al., 2000; Chapman et al., 2001). While such surveys efficiently locate a major part of the (sub)mm galaxy population, they are biased in redshift distribution and thus the optical/near-IR properties of counterparts. In § 3.3.2, we discuss this survey type in more detail. Table 3.6 summarizes the properties of the 28 objects meeting our selection criteria. By nature, this “reliable” sample from the literature emphasizes the bright and luminous end of the (sub)mm galaxy population, but is not a complete sample with strict selection criteria. 40 % of this sample are optically bright, ClassII, objects. At least five (and up to 16) objects are EROs (ClassI) and a maximum of 11 (down to 1) are Class0 objects — faint in K and but not as red as an ERO. Deeper I- (and K-) band imaging for Class0 objects could reveal whether they are faint EROs or faint blue galaxies.

The dustiness of local ULIRGs produces red UV/optical SEDs with considerable variation (Trentham et al., 1999). Recently, significantly improved rest-frame UV to far-infrared SEDs have become available for a number of local ULIRGs (Goldader et al., 2002; Klaas et al., 2001), which we use to analyze the observed optical to mm SEDs of (sub)mm galaxies and place constraints on their nature and redshift. We have combined UV (Trentham et al., 1999; Goldader et al., 2002) and far-infrared (Klaas et al., 2001) photometry of ULIRGs with optical and near-infrared photometry from the literature that we have approximately corrected to similar (large) apertures, to obtain good observed UV to mm SEDs for six ULIRGs: Arp 220, IRAS 19254–7245, Mrk 273,

Table 3.6. Submm/mm sources with interferometric confirmation

Source	Alias	z	Reference	Ident	Lens	S ₈₅₀	S _{1.4}	K	I	Class
(1)	(2)	(3)	(4)	(5)	(6)	mJy	μJy	mag	mag	(11)
00266+1708	M12		f00	mm,ra	2.4	18.6	94	22.45	>26.1	0(-I)
02399-0134	L3	1.06	sou99,s00	ra	2.5	11.0	500	16.34	19.31	II
02399-0136	L1+L2	2.81	i98,f98,s02a,g03	mm,ra	2.5	25.4	526	17.80	20.50	II
03025+0006	CUDSS3.7		w03b	ra	1	8.2	44	20.20	24.60	II
03026+0008	CUDSS3.6		w03b	ra	1	3.4	43	21.30	>24.40	0(-I)
04431+0210	N4	2.51	s99,s00,f03,n03	mm,ra	4.4	7.2	<70	19.41	26.50	I
09429+4658	H5		s99,s00	ra	1.5	17.2	32	19.58	>25.6	I
09429+4669	H8		c02,l02	ra	1.3	10.5	970	19.7	26.2	I
09431+4700	H7(+H6)	3.35	c02,l02,n03	mm,ra	1.2	10.5	55	>21.3	26.9	I-(0)
10519+5718	LE 850.3		i02,s02a	ra	1	7.7	98	18.86	23.24	II
10520+5724	LE 850.1		l01,i02	mm,ra	1	10.5	74	19.80	>25.0	I
10526+5724	LE 850.2		i02,s02a	ra	1	10.9	29	20.32	23.26	II
120507-0748.2	NDFnew03a		ea03	ra	1	6.1	88	21.48	>25.5	0(-I)
120509-0740.0	NDFnew34		ea03	ra	1	(8.3)	47	>22.0	>25.5	0(-I)
120517-0743.1	NDFnew25a			mm	1	(6.3)	<39	22.50	>25.5	0(-I)
120519-0749.6	NDFnew01		ea03	ra	1	4.5	47	>22.0	>25.5	0(-I)
120539-0745.4	NDFnew16			mm,ra	1	6.3	56	>22.7	>25.5	0(-I)
120546-0741.5	NDFnew31			mm,ra	1	18.5	44	21.90	>25.5	0(-I)
12368+6212	HDF850.1		d99,m00,dun02	mm,ra	3.0	7.0	16	23.60	>28.8	I
14009+0252	J5		i00a	ra	1.5	15.6	529	20.96	>23.2	0(-I)
14011+0252	J1	2.56	i00a,i01,dw03	mm,ra	2.8	14.6	115	17.60	20.70	II
14171+5229	CUDSS14A		b00,g00	mm,ra	1	8.8	120	19.61	24.13	II
154127+6615	A2125-2		b00	mm,ra	1.3	(10.0)	81	>21.2	>23.9	0(-I)
154127+6616	A2125-1		b00	ra	1.3	(10.5)	67	20.50	>23.5	II(-I)
16369+4105	N2 850.2		i02,sco02	ra	1	10.7	92	19.77	24.48	II
16370+4105	N2 850.1		i02,sco02	ra	1	11.2	45	19.48	21.99	II
16538+4057	N2 850.4	2.38	s03b,n03	mm,ra	≥1	8.2	221	18.43	21.83	II
17142+5016	No.18	2.39	s03b,k02	ra	1	5.6	260	19.40	22.50	II

Note. — Col. (1,2) — Name and aliases. Col. (3) — Spectroscopic redshift where available. Col. (4) — References. Col. (5) — Identification method: mm and/or radio interferometry. Col. (6) — Lensing magnification. *Subsequent quantities are as observed, i.e. not corrected for lensing.* Col. (7) — 850 μm flux density () means estimated as $2.5 \times S_{1.2 \text{ mm}}$. Col. (8) — 1.4 GHz flux density. Col. (9,10) — Magnitude of suggested near-infrared/optical counterpart (Vega). Col. (11) — Classification for optical/NIR counterparts of (sub)mm sources defined by Ivison et al. (2002).

Note. — Remarks on individual objects: 12368+6212 (HDF 850.1): originally identified by d99 with a faint optical arc. We follow dun02 who propose a new identification on the basis of combined MERLIN+VLA 1.4 GHz and deep SUBARU near-IR imaging.

Note. — References: b00: Bertoldi et al. 2000 — c02: Cowie et al. 2002 — d99,d03: Downes et al. 1999 — dun02: Dunlop et al. 2002 — f98,f00: Frayer et al. 1998, 2000 — g00: Gear et al. 2000 — g03: Genzel et al. 2003, — h98: Hughes et al. 1998 — i98,i00a,i01,i02: Ivison et al. 1998, 2000a, 2001, 2002 — k02: Keel et al. 2002 — l01: Lutz et al. 2001 — l02: Ledlow et al. 2002 — m00: Muxlow et al. 2000 — n03: Neri et al. 2003 — s99,s00,s02a,s03b: Smail et al. 1999, 2000, 2002a, 2003b — sco02: Scott et al. 2002 — sou99: Soucail et al. 1999 — w03b: Webb et al. 2003.

IRAS 15250+0309, IRAS 12112+0305, and IRAS 22491–1808. Figure 3.28 shows the K-band magnitude predicted for a 5 mJy source at 1.2 mm (similar to our targets), assuming these intrinsic ULIRG SEDs and redshifts up to 10. If the four bright PdBI-detected

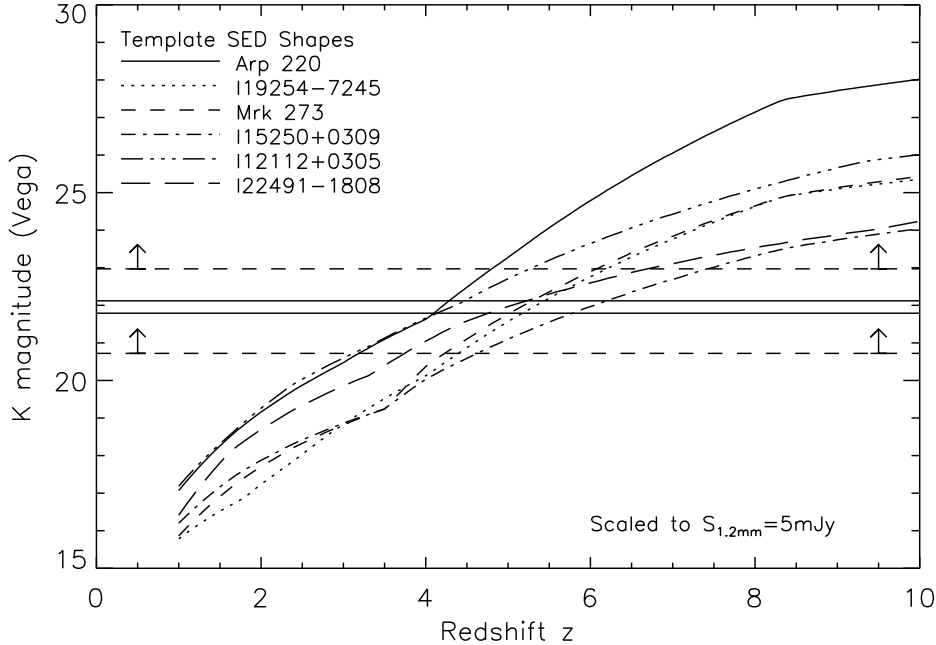


Figure 3.28 Expected K-band magnitude (Vega) of a mm galaxy as a function of redshift. The rest-frame SED is assumed to have the shape of local ULIRG SEDs for which high-quality UV to FIR photometry is available. The redshifted SEDs were scaled to $S_{1.2 \text{ mm}} = 5 \text{ mJy}$, which is representative for our MAMBO sources. Line styles identify the local ULIRGS used as SED templates. Horizontal solid lines represent the two K-band counterparts of the MAMBO galaxies MM J120517–0743.1 and MM J120546–0741.5, scaled to match a common $S_{1.2 \text{ mm}} = 5 \text{ mJy}$. Horizontal dashed lines indicate the 3σ limits for the two MAMBO galaxies MM J120549–0745.4 and J154127+6615, again scaled to match a common $S_{1.2 \text{ mm}} = 5 \text{ mJy}$.

MAMBO sources have spectral energy distributions similar to low-redshift ULIRGs, then the faint K-band limits imply that they are at very high redshifts ≥ 4 (in the case of MM J154127+6615, $z \geq 3$). Alternatively, they may be at a significant lower redshift ($z \sim 1 - 2$) but more obscured in the intrinsic UV-optical than even the most obscured local ULIRGs such as Arp 220. Both options are consistent with the radio to mm redshift estimator (Carilli & Yun, 1999, 2000), given the VLA detections of all four PdBI-detected

1.2 mm galaxies. Considering measurement errors, the scatter of the radio to mm spectral index versus redshift relation, and its flatness at high z , the four objects are consistent with the radio/mm index at any redshift ≥ 2 .

Another way to represent the optical/near-infrared properties is in the form of an I–K vs. K magnitude-color diagram as presented for SCUBA sources in Smail et al. (2002a), Ivison et al. (2002), and Webb et al. (2003a,b). Again, we restrict our analysis (Fig. 3.29) to objects with interferometric positions. For comparison, the figure also includes the field galaxy population from our NDF data and the expected properties of objects with SEDs similar to local ULIRGs. For these, we have picked both an object that is red in the UV/optical (Arp 220) and one that is blue (IRAS 22491–1808) from the objects studied in the UV by Trentham et al. (1999) and Goldader et al. (2002). We complete their SEDs with far-infrared data from Klaas et al. (2001) and large-aperture optical/near-infrared data from elsewhere in the literature. The color-magnitude relation is then derived for these redshifted SED *shapes* but scaling the absolute flux to an observed flux of 5 mJy at 1.2 mm. The main results from this analysis are the following. First, the optical/near-infrared colors of (sub)mm galaxy scatter cover a wide range at a given magnitude (the “diversity” of SCUBA galaxies, Ivison et al., 2000a). Second, with few exceptions this range is within the envelope expected for the range of redshifted local ULIRG SEDs. These exceptions are from the 8 mJy sample, which generally has a surprisingly large scatter of I–K colors, larger than for the mm counterparts, and includes some very blue objects. In our sample we find only one object with a limit consistent with $I-K < 3.3$ and one measurement $I-K = 3.33$, while there are about half a dozen identifications in the 8 mJy sample with objects at $I-K < 3.3$, a color well in the range of the normal field population. Third, for $K > 19$, the average (sub)mm source is redder in I–K than an average field galaxy of the same magnitude. This gives some support to the suggestion that nearby EROs are the most likely counterparts to SCUBA or MAMBO sources, but the dispersion in colors of both field galaxies and (sub)mm sources is too large to make this a robust criterion for identifications of individual submm sources without accurate positions. More specifically, the brightest (sub)mm counterparts ($K < 19$) are statistically indistinguishable in I–K color from the field population while (sub)mm counterparts are significantly redder at $19 < K < 21$. It is difficult to quantify at this point how the trend continues at $K > 21$ since observational limits in both K and I are significant for several of the samples involved. While the dispersion of I–K colors is larger for the 8 mJy survey counterparts than for

our objects, we do not see a significant difference in the mean color at a given magnitude.

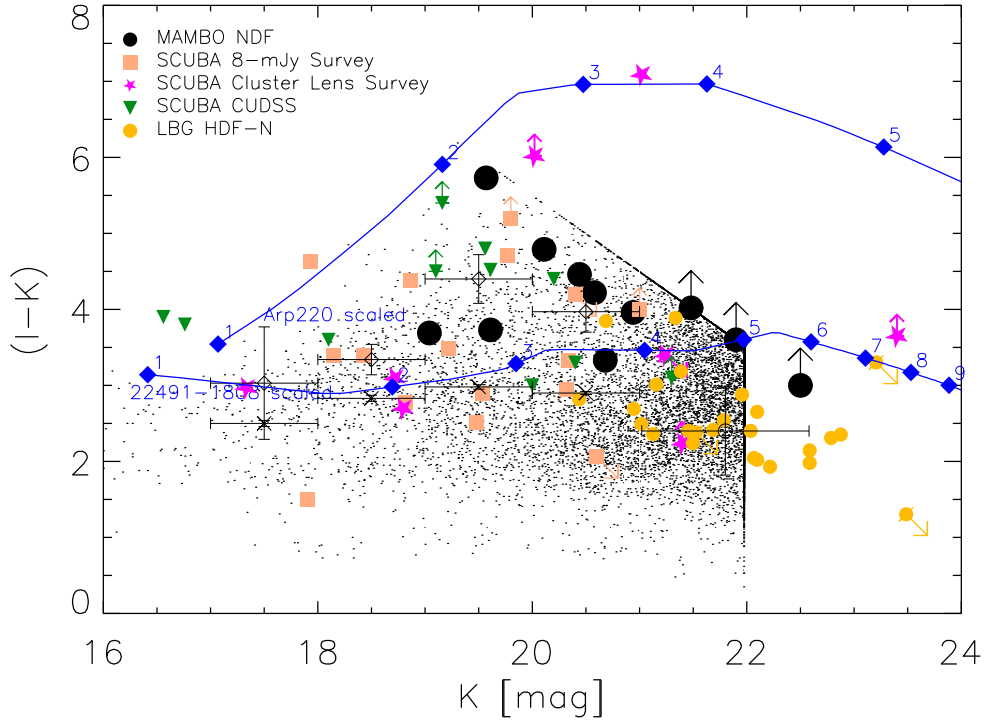


Figure 3.29 I-K vs. K magnitude-color diagram for the MAMBO identifications (large filled circles). Small dots show the field galaxy population from our NDF data. Interferometrically located SCUBA galaxies are represented by squares for the 8 mJy sample objects from Ivison et al. (2002), stars for cluster lens survey objects (corrected for magnification) from Smail et al. (2002a), and triangles for the CUDSS objects of Webb et al. (2003a,b). Filled diamonds connected by continuous lines show the expected colors/magnitudes for labelled redshift 1,2,... for objects with the SED shapes of Arp 220 and IRAS 22491–1808 *but scaled to observed* $S_{1.2\text{ mm}} = 5\text{ mJy}$. Average properties in magnitude bins are shown with error bars for the (sub)mm population (open diamonds) including all objects shown, and for the field population (crosses). Blank-field sources are not included, therefore the figure is an incomplete representation beyond the detection limits of the individual surveys. In addition, the LBG sample of Papovich, Dickinson, & Ferguson (2001, small filled circles) is included for comparison to the SMG source population.

Adelberger (2001) suggested that most of the galaxies forming the 850 μm cosmic background should be a sub-sample of galaxies selected in the rest-frame UV (e.g., LBGs). Based on the Lyman break galaxy sample (Papovich, Dickinson, & Ferguson, 2001) in the Hubble Deep Field North (HDF-N; Williams et al., 1996), which covers a redshift range $2.0 < z < 3.4$ similar to the redshift distribution of SMGs, we calculated the median I-band magnitude for a UV-selected survey, $\langle I_{LBG} \rangle_{median} = 24.3$ mag, and examined how many bright (sub)mm sources ($S_{850\mu\text{m}} \geq 8$ mJy) securely identified through interferometry would be detected in these surveys. Assuming a median redshift $\langle z_{LBG} \rangle_{median} \approx 2.8$ of this LBG sample⁶, the observed I band correspond to the rest-frame UV at ~ 2400 Å. As discussed above, the “easy detection” in the rest-frame UV is not seen for the MAMBO 1.2 mm galaxies. Only one-sixth of the radio-identified MAMBO galaxies are bright in the I band (≤ 24.3 mag). However, two-thirds of the 8 mJy SCUBA sources with a radio identification down to 40 μJy are brighter than $I = 24.3$ mag. Similarly reliable observations and identifications are currently impossible for the fainter ($S_{850\mu\text{m}} \leq 3$ mJy) objects, which comprise most of the 850 μm background. We compare the rest-frame UV-optical color of the LBG sample by Papovich, Dickinson, & Ferguson (2001) with the radio-identified SCUBA and MAMBO galaxies in Fig. 3.29. We note a small overlap between the 1.2 mm and the LBG sources, but a significant overlap is seen with the SCUBA CUDSS and SCUBA 8 mJy survey. Webb et al. (2003c) reported four possible LBG associations (all $I \leq 24.5$ mag) with SCUBA sources but they concluded that none of them is a reliable identification. The LBG sample of Papovich, Dickinson, & Ferguson (2001) spanning a range in the K band between $\sim 20.5 - 23$ mag is significantly bluer ($I-K = 2.4 \pm 0.6$) than the (sub)mm sources. A similar rest-frame UV-optical color Shapley et al. (2001) reported for its optical/NIR brighter LBG sample $\mathcal{R}-K_s = 2.9 \pm 0.6$. Baker et al. (2004, in preparation) divided LBGs into two samples, a blue ($R-K < 3$) and a red ($R-K > 3$) one, and observed both with MAMBO at 1.2 mm. The red LBG sample was detected at 2.5σ whereas the blue one at a 1σ level. This result seems to substantiate the claim by Chapman et al. (2000) based on observations of LBGs at 850 μm with SCUBA, that red LBGs could be dustier.

We compare the J–K colors that are available for our full sample with expectations for redshifted SEDs of ULIRGs. Fig. 3.30 shows the expected J–K colors as a function

⁶Only LBGs of Papovich, Dickinson, & Ferguson (2001) that have I-band photometry available (Williams et al., 1996) were selected; this sample consists of 25 LBGs. The HST I_{814} magnitudes are converted to Johnson I using the transformation from Holtzman et al. (1995).

of redshift for a sample of six local ULIRGs, using their rest-frame UV to NIR SEDs assembled on the basis of the UV data of Trentham et al. (1999) and Goldader et al. (2002) and of large aperture optical/NIR photometry from the literature. For this type of SED, the J–K color is not a unique indicator of redshift, but excursions to large J–K colors can occur for redshifts above 2 and red SEDs like that of Arp 220. Like Fig. 3.29, this diagram shows the large variety of colors for local ULIRGs. The locations of the MAMBO sources extend from J–K \sim 2, corresponding to intrinsically bluer SEDs or lower redshifts, to J–K $>$ 3.4 which is expected only for red Arp 220-like SEDs and high redshifts. Again, the most likely interpretation is that the spread in the intrinsic optical/UV SEDs of mm galaxies is large, similar to the spread for local ULIRGs.

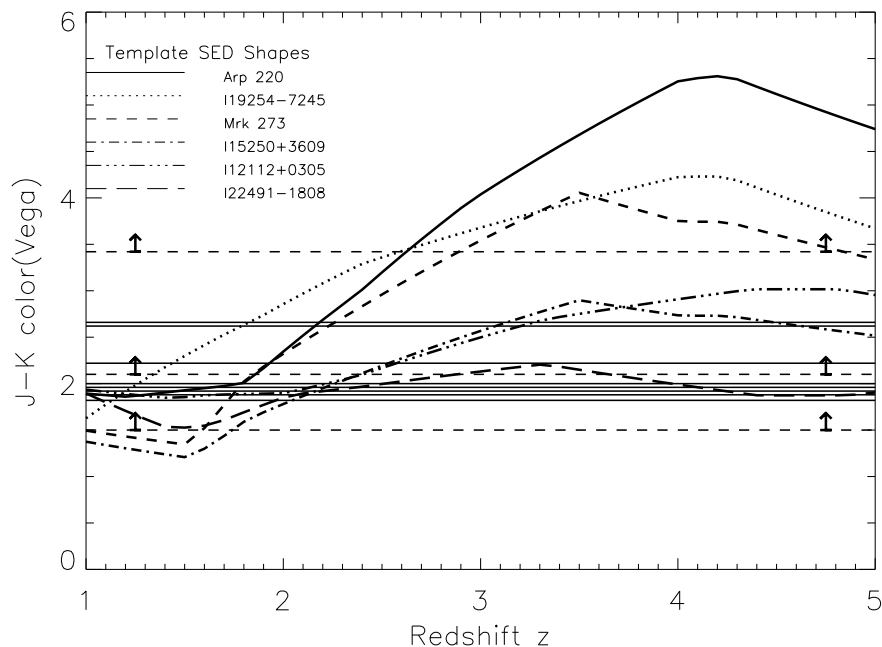


Figure 3.30 J–K color as a function of redshift for the template SED shapes of a number of local ULIRGs. Horizontal over-plotted lines show measurements (continuous line) or lower limits (dashed line) for the J–K color our MAMBO sources.

At least five of our 18 sources have ERO ($I-K > 4$) counterparts. Given the long-standing discussion about the contributions of passively evolving ellipticals and of dusty starbursts to this class, it is of interest to place our objects in this context. Fig. 3.31 shows an $I-K$ vs. $J-K$ color-color diagram proposed by Pozzetti & Mannucci (2000) to address this issue. Based on the dissimilarity between a 4000 \AA break and a red-

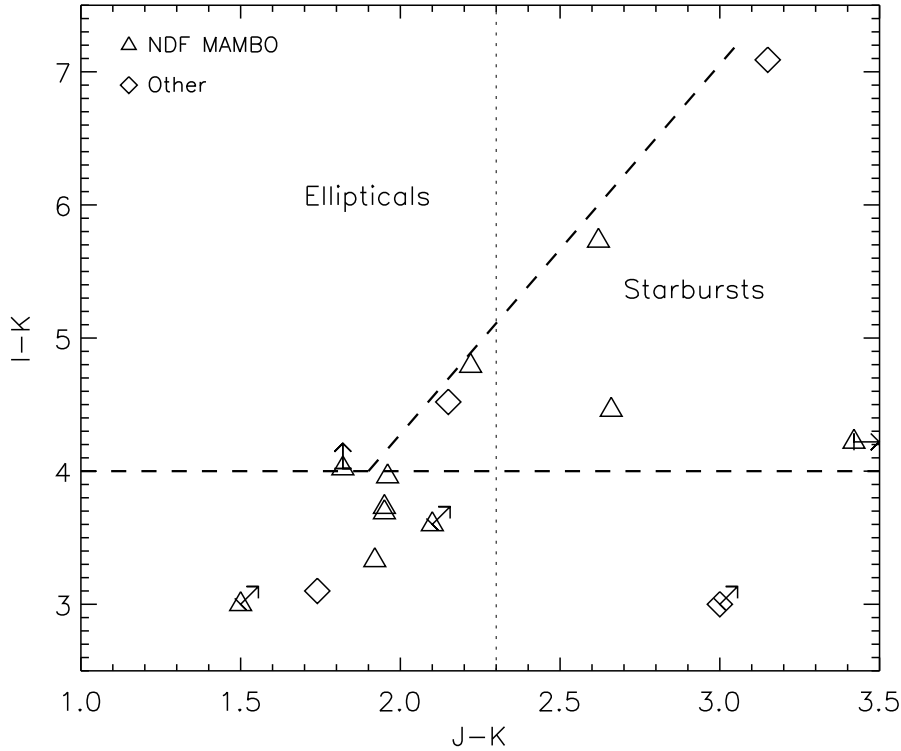


Figure 3.31 I-K vs. J-K diagram, with thick dashed lines showing the regions populated by $z \sim 1 - 2$ passive ellipticals and by dusty starbursts according to Pozzetti & Mannucci (2000). Triangles indicate NDF MAMBO sources. Diamonds indicate SCUBA sources from the literature with IJK photometry and one Abell 2125 MAMBO source from Bertoldi et al. (2000). The thin vertical dashed line indicates the $J-K > 2.3$ criterion of Franx et al. (2003).

dened, smooth starburst continuum, this diagram is expected to separate the two categories for redshifts in the range of roughly 1 to 2. With the possible exception of MM J12507-0748.1 (No. 03) the proposed mm and submm counterparts avoid the region of $z \sim 1 - 2$ evolved populations, which might be found in case of false identifications of mm sources with such objects. It is not possible to draw the inverse conclusion from this diagram, i.e. to conclude that we are observing starbursts at $z \sim 1 - 2$. The region populated by the (sub)mm sources is indicative of smooth spectra that are not very specific on redshift, or of spectra with a break between J and K. This caveat is particularly relevant since some (sub)mm objects are significantly fainter than the $z \sim 1 - 2$ EROs for which this method was developed.

Recently, Franx et al. (2003) presented a technique to select optical-break galaxies at a redshift $z > 2$ with the near-infrared filters J_s and K_s . van Dokkum et al. (2003) reported spectroscopic redshifts of a handful of such $(J_s - K_s) > 2.3$ pre-selected galaxies, five of six indeed lying at redshifts higher than $z > 2$ ($z = 2.4 - 3.5$). Individual similar objects have been found in other surveys (e.g., Dickinson et al., 2000; Maihara et al., 2001; Totani et al., 2001a; Im et al., 2002, sometimes called “HEROs”). We have probed for an overlap between this population and the MAMBO identifications. Franx et al. (2003) report a surface density of 3 ± 0.8 arcmin⁻² for objects with $J_s - K_s > 2.3$ and $K_s < 22.5$ mag. In our sample from a survey area of roughly 100 square arcmin, we suggest three identifications with $J - K > 2.3$, $K < 22$ mag galaxies. Given several more $J > 24$ mag limits, a few more might be found in deeper images to $K = 22.5$ mag among the objects with current $K > 22$ mag limits, and among the MAMBO sources without radio identification that are not discussed in this work. It is thus fair to assume that the contribution of mm galaxies in the few mJy range to the population of luminous red galaxies as observed by Franx et al. (2003) is of the order 1 to a few percent. This small overlap is consistent with submm/mm followup for the four HEROs of Totani et al. (2001a), reporting very weak sub/mm signals (Coppin et al., 2002, and P. Andreani et al. in prep.). Also, only one of the six $J_s - K_s > 2.3$ objects with spectroscopic redshifts reported by van Dokkum et al. (2003) has a spectrum consistent with that of a dusty starburst. On the other hand, the fraction of red $J - K$ sources ($J_s - K_s > 2.3$ and $K_s < 22.5$ mag) in the mm population is significantly higher. Of our MAMBO sources with radio counterparts, at least three out of 18 (~ 20 %) are identified with red $J - K$ sources. It may be higher, but the lack of deeper J-band data prevents us from estimating the colors of the faintest of the K-band counterparts. There might be an evolutionary connection beyond this small overlap, i.e. a contribution of mm galaxies in quiescent or post-active phases to the population of luminous red galaxies/HEROs.

3.3.2 Dependence on Radio Properties: Radio Pre-Selection and Detection Limits

One of the major issues in our developing understanding of the nature of (sub)mm-emitting galaxies at high redshift is how the method of selection influences the properties of the sources. For example, targeted submm follow-up of optically faint radio sources

(OFRS: $S_{1.4\text{ GHz}} \geq 40\ \mu\text{Jy}$, $I > 25\text{ mag}$; Chapman et al., 2001) has been used as an efficient method to detect and study a significant “radio-preselected” fraction of the (sub)mm population. This is a particularly important comparison for our study. Because we have limited ourselves to a investigation of only those mm sources in the NDF with interferometric identifications, we might expect a radio-preselected sample to have similar properties. Indeed, the strength of the conclusions of such studies obviously depends on the amount of overlap with the population detected in unbiased “blind” surveys (i.e., those not dependent on radio preselection), and on the nature of the biases induced by the OFRS selection. Both Barger et al. (2000) and Chapman et al. (2001), in comparing the submm detection efficiency of radio sources with that of blank field surveys, report a recovery rate of about 70% of bright ($> 5 - 6\text{ mJy}$) submm sources when targeting $S_{1.4\text{ GHz}} \geq 40\ \mu\text{Jy}$ radio sources with very faint near-infrared or optical counterparts ($\text{HK}' > 20.5\text{ mag}$ or $I > 25\text{ mag}$, respectively). In contrast, only 10 % of the refined 8 mJy sample are reported to have an $S_{1.4\text{ GHz}} \geq 40\ \mu\text{Jy}$, $I > 25\text{ mag}$ counterpart (Ivison et al., 2002). Using the same criteria, we recover 10 of 42 (about 25 %) of the original NDF MAMBO list.

While the recovery fraction of optically faint radio-identified sources presented here is similar to the low 8 mJy recovery rate of Ivison et al. (2002) at first glance, a clear difference exists in the nature of the sources not meeting the $S_{1.4\text{ GHz}} \geq 40\ \mu\text{Jy}$, $I > 25\text{ mag}$ criteria. We find 7 to 8 (about 20 %) optically bright ($I < 25\text{ mag}$) radio sources, while Ivison et al. (2002) find 12 of 30 optically bright sources (40 %) in their refined sample with $S_{1.4\text{ GHz}} \geq 40\ \mu\text{Jy}$ radio counterparts. This is another manifestation of the clear difference in typical counterpart brightnesses between the NDF MAMBO sources and the 8 mJy survey reported above. Irrespective of these differences, a large recovery rate by the radio preselection technique for faint optical sources is not supported by both “blind” surveys.

Part of the difference between the suggested 70 – 75 % recovery rates and the lower numbers found in the blind surveys may simply be due to the reference integral counts of the complete submm population and to the small areas covered by these surveys. The counts adopted by Barger et al. (2000) and Chapman et al. (2001) are near the low end of the range of count determinations summarized in Blain et al. (2002), and the number of sources in these fields meeting their criteria was relatively small (e.g., in Chapman et al. (2001), the recovery rate was determined based on 11 radio sources with submm detections and two sources without radio counterparts). In any case, a large recovery rate of the

optically faint radio pre-selection is not ensured, and the selection effects are complex (see also Chapman et al., 2002b). While the radio detection will overall favor low redshift (Carilli & Yun, 1999), optical faintness will prefer among those objects the higher-redshift ones. This is indeed suggested in our radio-identified sample, in which the mean redshift (approximated by the radio/mm indicator) is $\langle z \rangle = 2.8 \pm 0.2$ for the $I > 25$ mag objects compared with $\langle z \rangle = 2.4 \pm 0.2$ overall.

While a comparison of the recovery rate of radio-preselected sources with faint optical counterparts is interesting and instructive, perhaps a more robust comparison can be made with Chapman et al. (2003a). Their radio-preselected sample is defined without imposing constraints on magnitudes of the optical/near-infrared counterparts to the radio sources, now finding noticeable numbers of optically brighter ($I < 25$ mag) radio-identified submm sources in contrast to the earlier radio-preselected studies. Overall, they recover about 70 % of all submm sources, which is formally higher than both the MAMBO source recovery rate for our survey (~ 40 %) and that of Ivison et al. (2002, ~ 60 %). Similar to the differences we have found between our results and those of the 8 mJy SCUBA survey of Ivison et al. (2002), we also find a substantial difference between our results and the sources meeting our selection criteria of $S_{850 \mu m} \sim 8$ mJy and $S_{1.4 GHz} \geq 40 \mu Jy$ in Chapman et al. (2003a). For the 10 sources in Chapman et al. (2003a) meeting these criteria, we find a median I-band magnitude of ≈ 24 with only 20 % of the sources having I-band magnitudes fainter than $I = 25$ (two out of 10). Such a result is in stark contrast to our results with a median I-band magnitude of ~ 25.5 mag and ~ 80 % of sources having $I > 25$ mag.

It is important to note that the differences in recovery rates and counterpart properties are not a direct consequence of the applied radio flux limits combined with strong trends with flux. Making a higher flux cut ($40 \mu Jy$ as in our sample) in the radio detections of Ivison et al. (2002) only removes a small number of sources from their survey (three or four depending on how binary radio sources are treated, which still leaves a recovery rate of ~ 50 %). Similarly, the majority of sources in the radio-preselected samples of Barger et al. (2000) and Chapman et al. (2001), and Chapman et al. (2003a) have $S_{1.4 GHz} \geq 80 \mu Jy$ (well above their detection limit); changing the lower radio flux to our value thus has little effect.

3.3.3 Optical to Radio SED Constraints and The Nature of Bright (Sub)mm Sources

In the absence of spectroscopic redshifts for most objects, correlations among observed properties are useful for constraining the redshift and evolution of submm sources, and their relation to local infrared galaxies. Both panels of Fig. 3.32 combines two spectral indices derived on the basis of the near-infrared (K-band), submm, and radio properties of this sample: the abscissa is the submm/radio spectral index frequently used as a redshift indicator, and on the ordinate is a spectral index between observed K band and $850\ \mu\text{m}$, i.e., rest-frame optical and submm, which is probably a coarse redshift estimator as well (see discussion in a previous subsection and Fig. 3.28). We compare these with the indices and colors expected for six local template SEDs moved to redshifts between 1 and 5.

In addition, we compare the properties of the MAMBO sources with those of a small sample of (sub)mm galaxies that have been studied with similar methods. To be able to compare MAMBO and SCUBA sources, we estimate $850\ \mu\text{m}$ fluxes for those MAMBO sources where they have not been measured by scaling the 1.2 mm fluxes by a factor of 2.5, which is consistent with the median value of published ratios. This implicitly assumes that there is no major difference between the submm and mm populations. In Fig. 3.32, the MAMBO objects are on average below the SCUBA ones, but this is consistent with their optical/near-infrared faintness derived in the previous section.

The rest-frame optical emission of the observed (sub)mm sources is faint compared to the submm/far-infrared one, clearly requiring a high dust content. Given the opposite trends in k-corrections for the (sub)mm flux on one side and the radio and optical/NIR fluxes on the other side, redshifting a dusty galaxy SED will move the object from top left to bottom right in this diagram. Such a trend is indeed indicated in the top panel: the sources with the steepest $850\ \mu\text{m}$ to 1.4 GHz spectral indices also tend to be the sources with the steepest $2.2\ \mu\text{m}$ to $850\ \mu\text{m}$ spectral indices. This indicates, as perhaps expected, that the K band to submm index significantly depends on redshift because of the widely differing k-corrections at its defining frequencies, and that variations in source properties do not fully overwhelm this effect. Interestingly, the objects that are blank fields down to very faint K magnitudes mostly cluster in the (lower) right of this diagram, i.e. where the radio to submm redshift indicator puts them at the higher end of the redshift spread of (sub)mm galaxies. This result is most simply explained if these

are the highest redshift objects. The loci for the redshifted UV to radio SEDs of six local ULIRGs indicates clearly the scatter in the properties of the local population. In particular, significant offsets to the left are possible for objects with strong AGN, such as IRAS 19254–7245 with its reddened Type 2 AGN (Mirabel et al., 1991) and strong radio emission. It will be interesting to probe for AGN activity for the objects in the left ($\alpha(850\mu\text{m}, 1.4\text{ GHz}) \leq 0.65$) part of the diagram; indeed, some of the objects there show evidence of AGN activity (LE 850.12, Ivison et al. (2002), J02399–0134, Soucail et al. (1999)). For the radio/submm spectral index on the horizontal axis, the dispersion for a larger sample is of the order 0.16 (Carilli & Yun, 2000), and that of the NIR/submm index is of similar magnitude given the scatter arising from different ULIRG SEDs. A similar scatter is observed in the high-redshift (sub)mm population, shown by labeling of the top-panel objects with their CO-confirmed redshifts. Four of these six objects may also serve as an indication of a locus of $z \sim 2.5$ objects that is independent of the uncertain applicability of local templates. The average locus of these $z = 2.38$ to 2.81 (mean $z = 2.57$) objects is $\alpha(850\ \mu\text{m}, 1.4\text{ GHz}) = 0.76$ and $\alpha(2.2\ \mu\text{m}, 850\ \mu\text{m}) = -0.99$. Better statistics from ongoing CO follow-up observations providing confirmed redshifts is highly desirable to improve this calibration of Fig. 3.32. However, the CO-confirmed redshift may introduce an upward bias for this point, if the successful optical redshift measurements on which they depend correspond to brighter counterparts on average. Less bias should be present in the horizontal (radio/submm) direction. We find about two-thirds of the MAMBO/SCUBA objects towards the “high redshift” direction to the right of this point. This is an underestimate, since the plot shows almost exclusively radio-detected objects, thus missing roughly one-third to one-half of the parent samples including the potential highest redshift objects. Altogether, this indicates that the median redshift of 2.4 suggested for the bright SCUBA population from optical redshifts (Chapman et al., 2003a) is an underestimate of the median redshift of the complete population. The submm/radio redshift indicator is unfortunately not accurate enough to assign good redshifts, but distinguishes the K-band faint objects from the rest of the population. If they were yet more extremely obscured objects than ULIRGs but with a redshift range similar to the other sources in Fig. 3.32, the scatter across the lower half of the diagram would likely be greater than observed.

Moreover, having a significant fraction of (sub)mm sources at high redshift apparently does not violate any constraint from the SED of the cosmic infrared background

(CIRB). For example, Gispert, Lagache, & Puget (2000) showed that the contribution of objects with SEDs like those of local ultraluminous infrared galaxies at $850 \mu\text{m}$ to the CIRB at high redshifts ($z > 4$) can be quite significant ($\approx 20 - 40 \%$) without violating any constraints provided by the CIRB spectrum. Based on COBE FIRAS data, Fixsen et al. (1998) derived an average spectrum of the extragalactic far-infrared background in the frequency interval $\nu = 5 - 80 \text{ cm}^{-1}$ ($2000 - 125 \mu\text{m}$): $I_\nu = (1.3 \pm 0.4) \times 10^{-5} (\nu/\nu_0)^{0.64 \pm 0.12} B_\nu(18.5 \pm 1.2 \text{ K})$, where B_ν is the Planck function. Using the same data, but different approaches for the modeling and the removal of the far-infrared foreground emission, Puget et al. (1996) parameterized the extragalactic background light (EBL) in the far-infrared as, $\nu B_\nu \approx 3.4 \times 10^{-9} (\lambda/400 \mu\text{m})^{-3} \text{ Wm}^{-2} \text{ sr}^{-1}$, and noted that the spectrum seems to indicate the presence of high- z sources. We used both equations to calculate the EBL both at $850 \mu\text{m}$ and 1.2 mm . The Fixsen et al. (1998) method gives an EBL of $4.4 \times 10^4 \text{ mJy deg}^{-2}$ at $850 \mu\text{m}$ and of $1.9 \times 10^4 \text{ mJy deg}^{-2}$ at 1.2 mm , yielding 2.2 as the submm-mm flux ratio. We find $3.1 \times 10^4 \text{ mJy deg}^{-2}$ at $850 \mu\text{m}$ and $1.4 \times 10^4 \text{ mJy deg}^{-2}$ using the equation by Puget et al. (1996), but we note that the equation is valid only between $400 - 1000 \mu\text{m}$, so we had to extrapolate beyond $1000 \mu\text{m}$. In this case, the $850 \mu\text{m}/1.2 \text{ mm}$ flux ratio is 2.1, similar to that via Fixsen et al. (1998). Assuming a starburst galaxy at $z = 2.5$, Greve et al. (2003) scaled the counts at $850 \mu\text{m}$ of the supermap on the HDF-N (Borys, Chapman, Halpern, & Scott, 2003) by a factor of $S_{850 \mu\text{m}}/S_{1.2 \text{ mm}} = 2.5$ and reported a good agreement between shapes of the 1.2 mm and $850 \mu\text{m}$ counts. The fact that the slope used to reproduce the number counts is similar to the slope based on the far-infrared EBL flux indicates that a major fraction of the SCUBA and MAMBO source population could overlap. This could reduce the possibility of a significant redshift trend between the two populations but strengthens the hypothesis that residual misidentifications with bright objects, cosmic variance, and small-number statistics could explain our discrepancy (§ 3.3.1) in optical and near-infrared magnitudes.

A conclusion drawn from the diagnostic diagram for the near-infrared to radio SEDs of (sub)mm galaxies (Fig. 3.32) is that MAMBO and SCUBA sources are at high redshift and/or are at least as obscured as local ULIRGs. A technical factor affecting this reasoning is the unknown spatial structure of the objects. If the objects were very large, then cosmological surface brightness dimming could lead to the observed small structures (Fig. 3.7), which may just reflect the central high-surface-brightness regions of more lumi-

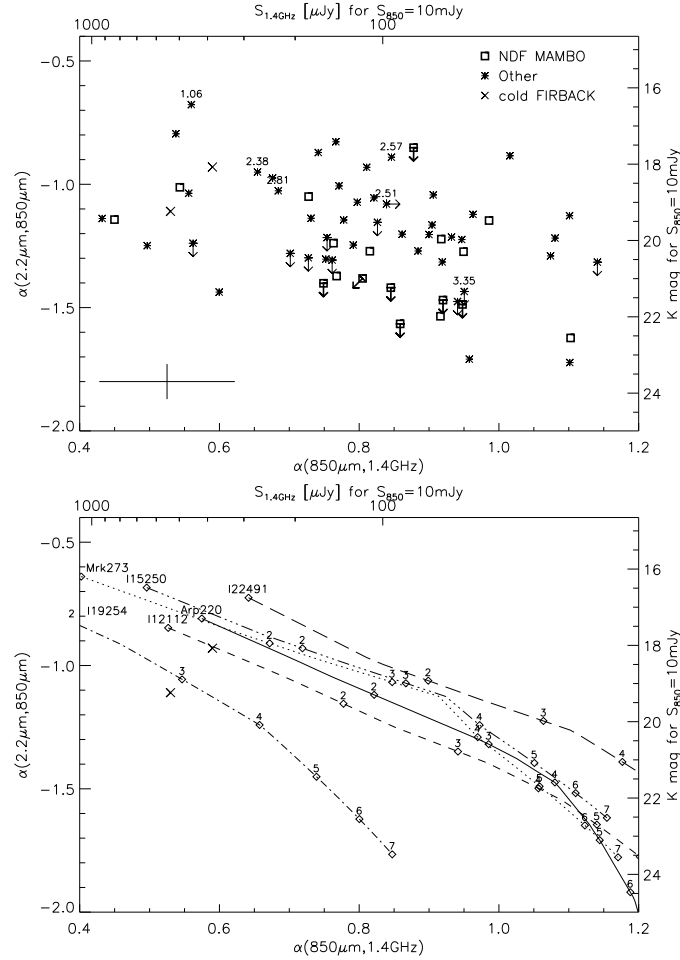


Figure 3.32 *Top*: Diagnostic diagram for the near-infrared to radio SEDs of (sub)mm sources, combining the radio/submm spectral index with a spectral index between near-infrared and submm. Squares/limits represent the NDF MAMBO source discussed in this paper, asterisks/limits represent mostly SCUBA sources from the samples described in the text, and a few individual well-studied (sub)mm objects. Objects with CO-confirmed redshifts are labeled with their redshift. A typical observational error is indicated in the bottom left. The two FIRBACK sources at $z = 0.45$ and 0.91 studied by Chapman et al. (2002b) are shown with crosses. *Bottom*: Shows for comparison the loci corresponding to the redshifted SEDs of a number of local ULIRGs with available UV to radio SEDs. Note that IRAS 19254–7245 hosts a powerful AGN.

nous extended objects that cannot be fully retrieved at realistic noise levels by increasing aperture size. This would cause a tendency to underestimate the total near-infrared flux.

There is evidence for some objects of this type in the (sub)mm population from near-IR imaging (e.g., Lockman 850.1, Lutz et al., 2001), and through radio mapping, Ivison et al. (2002) claims some objects are resolved by a $1.4''$ beam. Examples of extended and complex morphologies are also seen in *Hubble Space Telescope* images of radio-preselected submm galaxies (Chapman et al., 2003c). For many other well-studied (sub)mm sources the detected regions fit into $2''$ apertures, but these may be the deceiving effects of surface-brightness dimming if they are at very high redshift. Some estimate of the magnitude of the effect can be gained from comparison with the local ULIRG population. Half-light radii have been estimated at several wavelengths, with median results of the order of 5.3 kpc in U (Surace & Sanders, 2000), 3 kpc in I (Zheng et al., 1999) and about 1.5 kpc in H and K (Colina et al., 2001; Tacconi et al., 2002). At redshifts around 3, an aperture of $2''$ diameter spans about 15 kpc. Half-light radii of ~ 4 kpc in the rest-frame V band (observed K band) would then mean no significant loss of light outside our aperture. This is only true as long as the structural analogy to local ULIRGs holds, of course, and a major fraction of light could be lost for objects more than a factor of 2 larger, especially if at $z \geq 4$. Such large objects would be placed too low in Fig. 3.32 by our measurements. This implies that the displacement of many SCUBA and MAMBO objects downwards from the location of local ULIRGs could include an effect of large spatial extent as well as obscuration of the rest-frame optical part of the SED. Testing such a scenario would require extremely deep K imaging. Size constraints at other wavelengths (optical, millimeter, and radio) will be useful as well, but for this question they will have to be interpreted with some caution considering the strong trends for local infrared galaxies, where half-light radii decrease as wavelength increases.

All galaxies detected in (sub)mm surveys, except perhaps for a few of the very highest-redshift ones, will be observed on the long-wavelength side of their rest-frame far-infrared emission maximum, while local comparison objects were selected by IRAS near the maximum or slightly to its short-wavelength side. This situation can induce a bias, favoring detection of objects with somewhat colder dust in the (sub)mm surveys. Attempting to reproduce the observed number counts of submm galaxies, both hydrodynamical cosmological simulations by Fardal et al. (2001) and modeling based on semi-analytical galaxy formation models by Kaviani, Haehnelt, & Kauffmann (2003) invoke colder SEDs more similar to local luminous infrared galaxies (Dunne et al., 2000a) rather than the warmer SEDs of local ULIRGs (see also Eales et al., 2000). Keeping the observed (sub)mm flux

fixed, a colder SED will result in a lower-redshift and/or less luminous object. The additional optical/near-infrared and radio constraints can test the plausibility of these assumptions. In Fig. 3.33, we show where the colder ($T < 35$ K) among the local galaxies observed by Dunne et al. (2000a) would be placed for several redshifts on a diagram combining near-infrared/submm and submm/radio spectral indices, as already shown for the (sub)mm sources in Fig. 3.32. Clearly those colder LIRG-like SEDs predict K-band magnitudes that are too bright and are not consistent with the results for the (sub)mm galaxies. The scenarios of Fardal et al. (2001) where the SEDs of submm galaxies are closer to the cooler LIRGs studied by Dunne et al. rather than the ULIRGs adopted by other workers is, hence, inconsistent with the overall SED information including the observed near-infrared (rest-frame optical). This is a consequence of the lower luminosity and colder objects in the local universe having a higher relative fraction of optical to infrared luminosity. Suppressing the K-band emission observed at higher redshift for such SEDs to the required level would require that the (sub)mm galaxies are at even higher redshifts than discussed above. If the rest-frame far-infrared SEDs of (sub)mm galaxies are cool, their overall SEDs still must be distinct from local universe cold LIRGs in having a much stronger ULIRG-like obscuration of optical emission. Such galaxies — which lack analogs in the local universe — could be envisaged as a collection of the “coldest” and most obscured star-forming regions like SgrB2, without admixture of the warmer and less obscured regions normally representing other evolutionary stages of star-forming complexes. Alternatively, they could be modeled as dilute obscured “cirrus”-type systems (Efstathiou & Rowan-Robinson, 2003), but only with the stringent assumption of constant optical depth dust enclosing the entire large region. Recently, Chapman et al. (2002b) reported for two optically faint, red ULIRGs preselected from the FIRBACK survey (Puget et al., 1999; Lagache & Dole, 2001; Dole et al., 2001), temperatures of about 30 K and $z < 1$: FN1-64 at $z_{spec} = 0.91$ ($z_{CY} \sim 1.3$) and FN1-40 at $z_{spec} = 0.45$ ($z_{CY} \sim 1.2$). Based on their SCUBA ($S_{850 \mu m} = 6$ mJy) and VLA detections ($S_{1.4GHz} \sim 200 - 300 \mu Jy$) and local ULIRG templates, this was surprising as they were expected to lie at $z > 1$ (Fig. 3.32). The SED and temperature characteristics of these two FIRBACK sources are consistent with those of the cold “cirrus”-type systems — having bolometric luminosities at least as great as Arp 220 — described by Efstathiou & Rowan-Robinson (2003). We conclude that optically faint radio-identified (sub)mm galaxies which are cold ULIRGs are not numerous at redshifts $z \sim 2 - 3$. This is consistent with the report of Chapman et al.

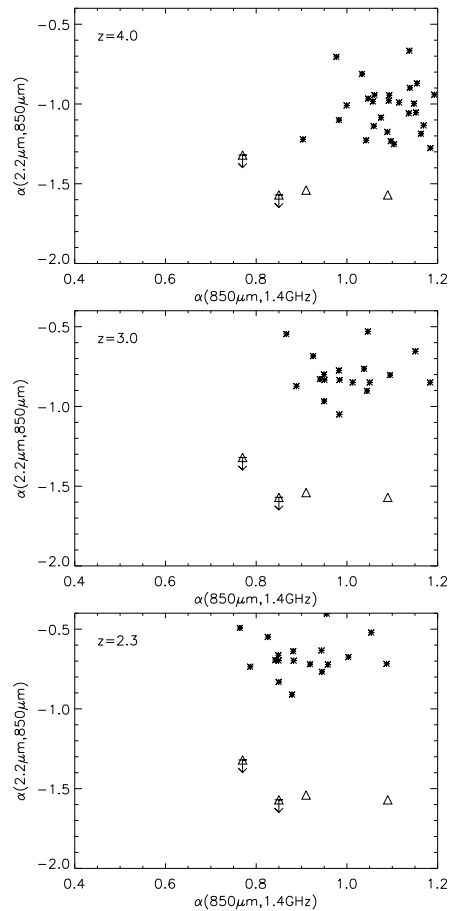


Figure 3.33 Near-infrared/submm vs. submm/radio spectral indices for cool ($T < 35$ K) galaxies from the Dunne et al. (2000a) sample of local galaxies shifted to three different redshifts. The indices for these galaxies (asterisks) at $z \sim 4$ (top), $z \sim 3$ (middle), and $z \sim 2.3$ (bottom) are derived on the basis of B, V, R fluxes (which correspond to K band at those redshifts) for those Dunne et al. galaxies where they are available (B, V) or can be extrapolated (R), and the submm and 1.4 GHz fluxes corrected for redshift using the Dunne et al. blackbody fits (submm) and a spectral index of -0.8 (radio). For comparison, we add the four PdBI-detected MAMBO galaxies (triangle) in each panel. For all these redshifts, the Dunne et al. objects are too bright in K to match the MAMBO galaxies and the other (sub)mm galaxies shown in the same diagram in the top left panel of Fig. 3.32.

(2002b) that the contribution of optically faint FIRBACK sources detected both in the radio and submm to the $850 \mu\text{m}$ counts for bright SCUBA sources (≥ 6 mJy) is small

($\sim 3\%$). Strikingly, the location of these cold, ultraluminous sources is different to that of the cool LIRGs, shown in Fig. 3.33.

We now return to the question of what causes the near-infrared faintness of the majority of our counterparts. In § 3.3.1, we have discussed two possibilities for the nature of bright (sub)mm sources that are very faint in the near-infrared ($K \geq 22$ mag). They are either heavily obscured starbursts/AGN — in this context more heavily obscured than any well-studied local starbursts or QSOs — or are, as suggested by the above analysis, similar to low-redshift, dusty, powerful starbursts but located at very high redshifts ($z \geq 4$). In either case, several important inferences can be drawn.

In the local ULIRG population, the amount of UV light observed, even if corrected for extinction, traces only a small fraction of the bolometric luminosity ($\leq 10\%$; Goldader et al., 2002). This implies that most of the intrinsic UV emission is not detected in ULIRGs but is completely obscured. The observed UV emission simply cannot be related to the sites where most of the bolometric luminosity is produced. To make the rest-frame UV/optical to far-infrared SED even redder than the most highly reddened galaxies in the local universe would require special circumstances in order to lower the ratio of optically visible to total luminosity yet further. One such special circumstance is an extremely young starburst which is completely obscured in all directions. To maintain heavy obscuration the starburst must be younger than the time necessary for significant gas removal due to the feedback from stellar winds and supernovae. This timescale is at most a few $\times 10^7$ years and likely significantly less (Lehnert, Heckman, & Weaver, 1999; Heckman et al., 2000; Thornley et al., 2000). Otherwise, in a second special case, the gas accretion rate and timescale must be such that as the feedback clears regions of young or intermediate-age stars, there would be inflowing gas available to maintain the overall obscuration. Maintaining such extremely high obscuration would require gas with substantial amounts of dust to fall onto the region of intense star formation and have a distribution such that there are very few regions of low optical depth in the rest-frame UV. In addition, such vigorous infall must be maintained for at least the gas clearance time scale and likely much longer. A third possibility would be to invoke a large-scale but still very thick and non-star-forming cocoon around the star-forming zone, delaying destruction by gas removal but putting strong requirements on the size and uniformity of such a cocoon.

The other plausible scenario for the nature of these bright (sub)mm sources is that

their SEDs are similar to those of the most obscured local dusty starbursts but are at extremely high redshift ($z \geq 4$). It is now well-understood that local ULIRGs are a result of the interaction or merger of two gas-rich spiral galaxies (see Sanders & Mirabel, 1996, and references therein). Continuing this analogy of (sub)mm sources being high-redshift galaxies with extremely high star-formation rates and SEDs that are ULIRG-like would then suggest that they too are the mergers of massive disk galaxies. Higher gas fractions in high-redshift galaxies may support such a process. The main implication of this scenario is the need to have massive units in place for the $z > 4$ merger, that are gas-rich enough to sustain star formation rates of the order $1000 M_{\odot} \text{ yr}^{-1}$ and provide the material obscuring this burst.

In either event, the implications for our understanding of the formation of spheroids is interesting. Requiring extremely high obscuration to explain the properties of the brightest mm sources is consistent with a model whereby spheroids are formed through a process similar to the “monolithic collapse” model, that is, through the rapid collapse of large amounts of gas which is maintained over several to many dynamical time scales (of order 100 Myrs – 1 Gyr; see e.g., Jimenez et al., 1999). A model like this has the attractive feature of being able to supply the gas necessary to both maintain the high UV extinction and the large fraction of the total bolometric luminosity that must be emitted in the infrared/submm. If, on the other hand, the SEDs of the mm sources are similar to those of the local ULIRGs, then the problem is that at $z = 4$ (the low end of possible redshifts for these sources, see Fig. 3), the age of the Universe is only about 1.5 Gyr or about 11 % of its current age. Within the context of the popular hierarchical merging models, this time is too short to form massive metal-rich disks for the necessary merging to take place (see Fardal et al., 2001). Hierarchical merging models simply have great difficulty in producing the high rates of star-formation — which these galaxies are likely have at such high redshifts — in sufficient numbers of galaxies. For example, in the results of the simulation by Fardal et al. (2001), the sources that can be identified with the faint submm population ($S_{850 \mu m} \geq 1 \text{ mJy}$) are found at redshifts of about 1–3 with no sources at $z \geq 4$ obtaining a large enough luminosity sufficient to be detected at the flux levels of the sources investigated here. In both merging and “monolithic collapse” models, prompt metal enrichment may also be necessary to create sufficient amounts of dust to effectively allow for the virtually complete re-emission of the bolometric luminosity into the infrared/submm.

3.3.4 Redshift Estimates and Star-Formation-Rate Density

Currently, we have not obtained a reliable spectroscopic redshift for a MAMBO 1.2 mm galaxy in the NTT Deep Field. Thus, we can only make redshift estimates based on diverse photometric techniques for individual MAMBO sources. For the NDF MAMBO survey field, 1.4GHz radio information is available, and thus we estimate redshifts based on the radio-mm spectral index (Carilli & Yun, 1999, 2000) discussed in more detail in § 1.2.3. In addition, based on our optical/near-infrared photometry, photometric redshifts for the NDF sources with optical/NIR counterparts were derived. We used the publicly available software *hyperz* (Bolzonella, Miralles, & Pelló, 2000). This photometric redshift code is widely used in the observational cosmology community (e.g., Smail et al., 2003) and offers a large parameter set (e.g., filters at different telescope facilities, reddening laws, cosmology, galactic reddening, see also Fig. A.4). Our analysis (see Appendix A) of the photometric redshifts of non-mm sources gives us confidence in the reliability of using photometric redshifts in the interpretation of mm counterparts and other objects close to the interferometric positions.

Figure 3.34 compares the photometric redshifts with the radio/mm redshift estimates. We consider this a plausibility check given the uncertainties in both methods. The sources are often faint, with relatively large photometric uncertainties in some of the bandpasses (especially the optical ones), and the templates used in the photometric redshift estimates may not be fully appropriate for the likely ULIRG-like SEDs. The radio/mm redshift estimates are affected by the faintness of the radio and mm detections and the internal scatter of the relation for the radio/mm redshift estimate. It is therefore reassuring that most sources are consistent with a one-to-one relationship between photometric and spectroscopic redshifts, with a few well-defined exceptions. Two sources (07 and 04) are at low photometric redshift but high radio/mm estimate. We have argued above for the possibility of foreground objects in these two cases. One object (36) has a relatively low radio/mm estimate that could indicate an AGN contribution but is still consistent with scatter in this relation. The optical “blank fields” tend to have high radio/mm redshift estimates. This is clearly consistent with them being faint/obscured high-redshift sources, but misidentifications due to the relatively uncertain radio sources may also contribute. For the radio-identified sources, the redshift range estimated from the radio/mm index is 0.83 – 3.86 (see Tab. 3.5). The optical/NIR photometric redshift lies for our sample

between 1.25 and 2.49 (see Tab. 3.5). The median redshift of the radio-identified mm sources is ~ 2.6 from the radio/mm estimator, and the median optical/near-infrared photometric redshift for the objects with counterparts is ~ 2.1 .

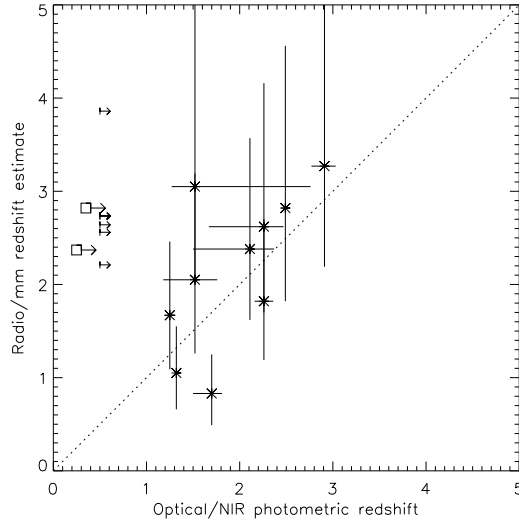


Figure 3.34 Comparison of optical/near-infrared photometric redshifts with redshift estimates from the radio/mm spectral index. Blank fields without photometric redshifts are shown with an arbitrary lower limit of 0.5 for the optical/near-infrared photometric redshift, and without the error bars for the radio/mm estimate. For two objects (squares), we believe that the measured optical/NIR photometric redshift refers to a foreground object, the true redshift of the submillimeter source being higher (see text).

Based on optical surveys (CFRS, HDF-North), several groups (e.g., Lilly, Le Fevre, Hammer, & Crampton, 1996; Madau et al., 1996) investigated the star-formation-rate history of the universe up to a redshift $z \sim 4$. Between $z = 0$ and $z \sim 1 - 1.5$ a dramatic increase of a factor ~ 10 in the star-formation-rate-density (SFRD) is observed (Lilly, Le Fevre, Hammer, & Crampton, 1996). At $z \sim 3.3$ the SFRD is at least a factor of 5 higher than at $z = 0$ (Steidel, Giavalisco, Dickinson, & Adelberger, 1996), and at $z \sim 4$ the lower limit of the SFRD is the same as at $z = 0$ (Steidel et al., 1999). The controversy is what is the form of the SFRD: does it stay constant from $z = 1$ to very high redshifts ($z \geq 4$), or does it decline? Thus, the study of dust-enshrouded active star-forming systems like the SCUBA/MAMBO galaxies gives us more insight into the star-formation history of the universe at high redshifts. The advantage is that

(sub)mm and/or radio observations of SCUBA/MAMBO sources are not hampered by obscuration. Thus, no assumption about extinction — the largest source of uncertainty for objects selected from UV/optical surveys — has to be made and the star-formation rate can be derived directly from the (sub)mm and/or radio fluxes. Using only one flux and an assumed SED for the conversion from flux to SFR introduces uncertainties. The redshift information for our MAMBO galaxies is obtained by applying the radio-mm spectral index for the whole sample MAMBO sources. The poorly known redshifts derived via this method are the disadvantage of our analysis. For the 8 mJy sample, we use the radio-submm spectral index in cases where no spectroscopic redshift has been obtained.

The observed MAMBO source population down to $S_{1.2\text{ mm}} \approx 2.0$ mJy comprises only a minor fraction of the source counts (e.g., Greve et al., 2003). Thus it would only yield a lower limit for the SFRD and we have to correct for the missing observed sources. The depth of our survey is similar to that of the SCUBA 8 mJy survey. Moreover, recently Greve et al. (2003) showed that the shapes of the number counts at 850 μm and 1.2 mm down to the limit of the MAMBO survey are similar. As MAMBO observations only observe the tip of the (sub)mm source population, we adopt the correction derived and used in the SCUBA 8 mJy survey. Based on the differential number counts of Barger, Cowie, & Sanders (1999), Ivison et al. (2002) calculated a factor ~ 12 . The correction takes into account SCUBA sources down to 1 mJy which cover a significant fraction of this source population, (see e.g., Cowie, Barger, & Kneib, 2002). To derive the SFR for our individual objects, we use the 1.2 mm and 20 cm window, both unhampered by obscuration. The estimation of the SFRD at these wavelengths is not independent because the redshift estimates used are derived from the 1.2 mm and 20 cm flux in most of the cases (radio-mm spectral index method). The calculation of the SFR based both on the radio and mm flux is similar to Ivison et al. (2002). Following Yun, Reddy, & Condon (2001), we calculate the star formation rate: $\text{SFR}(M_{\odot} \text{ yr}^{-1}) = 5.9 \pm 1.8 \times 10^{-22} L_{1.4\text{ GHz}} \text{ W Hz}^{-1}$. The calculation is based on a Salpeter initial mass function (IMF) $\phi(M) \propto M^{-2.35}$ for $0.1 < M_{\odot} < 100$ (Salpeter, 1955). The rest-frame 1.4 GHz luminosity $L_{1.4\text{ GHz}}$ is: $L_{1.4\text{ GHz}} = 4\pi D_L^2(z) S_{1.4\text{ GHz}} (1+z)^{-(\alpha+1)} \text{ W Hz}^{-1}$. We assume a spectral index $\alpha = -0.8$, $D_L(z)$ is the luminosity distance, and $S_{1.4\text{ GHz}}$ is the flux density at 1.4 GHz. Based on these equations, we compute the SFR for the whole MAMBO sample using the flux den-

sity at 1.4 GHz. Following a simple approach⁷ of e.g., Lutz et al. (2001), we estimate the infrared luminosity $L_{FIR} \approx 2.1 \times 10^{12} L_{\odot} \times \frac{S_{250\text{ GHz}}}{\text{mJy}}$ for our MAMBO 1.2 mm sources and convert it to $\text{SFR} = \frac{L_{FIR}}{5.8 \times 10^9} M_{\odot} \text{ yr}^{-1}$ (Kennicutt, 1998, Salpeter IMF). The SFRs calculated with these two methods agree well and range between $\sim 500 - 2000 M_{\odot} \text{ yr}^{-1}$ (Tab. 3.7). In cases where MAMBO sources are undetected in the radio, we assume the detection limit of $39 \mu\text{Jy}$ for the radio flux and a lower-limit redshift estimate as the redshift of the 1.2 mm source. Considering how the radio-mm spectral index is defined, SFRs based on radio detection limits must be taken as lower limits. This tends to underestimate the contribution of the non-radio detections to the SFRD of the mm population and is a key point for the trend of SFR at $z \geq 4$. We divide both the NDF MAMBO and the SCUBA 8 mJy sample among several redshift bins. In Tab. 3.8 the calculated SFRDs for both the MAMBO and the SCUBA 8 mJy sources, assuming a MAMBO survey area of ~ 126 square arcmin, are listed and in Fig. 3.35 our results are shown (squares). Due to a number of uncertainties (even partly dependent on each other) involved in the calculation of the SFRD — e.g., (sub)mm flux calibration; spurious (sub)mm sources; misidentifications; non-radio detections; no spectroscopic redshifts for the MAMBO galaxies in the NDF and only for a small part of the SCUBA 8 mJy sources; coarse redshift estimates by the radio-(sub)mm spectral index —, the calculated SFRDs for the (sub)mm populations have to be seen as rough estimates.

In Fig. 3.35 the SFRD based on the 1.2 mm flux is shown with big symbols and the SFRD derived from the 1.4 GHz flux with small symbols. In comparison, the SFRD derived for the 8 mJy survey, covering an area of 200 square arcmin (Fox et al., 2002), is presented (diamonds) as well, also using both methods. Furthermore, different high-redshift source populations are incorporated in our diagram: a μJy radio-detected ERO sample spanning a redshift range of 0.8–1.2 of Smail et al. (2002b, five pointed star), LBGs at different redshifts (Steidel, Giavalisco, Dickinson, & Adelberger, 1996; Steidel et al., 1999; Lehnert & Bremer, 2003; Stanway, Bunker, & McMahon, 2003a; Stanway et al., 2003b, cross symbols)⁸, and $\text{H}\alpha$ -selected galaxies (Yan et al., 1999, triangle symbol). At different epochs, the SFRD for the SCUBA and MAMBO source population is similar. Over-

⁷It should be noted that we make certain assumptions about SED, k-corrections and z . Thus, the calculated infrared luminosity should be seen as an approximate.

⁸Extinction corrections are taken into account for the different LBGs surveys. The survey depths vary different. Steidel, Giavalisco, Dickinson, & Adelberger (1996); Steidel et al. (1999) and Lehnert et al. (2003 and priv. comm.) go down to $0.3L_{LBG}^*$ whereas Stanway, Bunker, & McMahon (2003a) and Stanway et al. (2003b) only go down to L_{LBG}^* .

Table 3.7. SFR of MAMBO galaxies in the NDF

Source Name (1)	SFR _{1.4 GHz} (2)	SFR _{1.2 mm} (3)
MM J120519-0749.5 (01)	1764	1892
MM J120516-0748.9 (02)	* 1036	1091
MM J120507-0748.1 (03)	1657	1673
MM J120531-0748.1 (04)	998	982
MM J120518-0748.0 (05)	* 1913	1964
MM J120520-0748.0 (06)	* 878	909
MM J120530-0747.7 (07)	1062	1091
MM J120524-0747.3 (08)	728	728
MM J120508-0747.0 (09)	* 1119	1164
MM J120510-0747.0 (10)	1089	1128
MM J120524-0746.7 (11)	* 734	728
MM J120518-0746.7 (12)	* 668	655
MM J120526-0746.6 (13)	923	946
MM J120502-0746.6 (14)	* 1207	1310
MM J120527-0746.0 (15)	* 805	873
MM J120539-0745.4 (16)	1630	2328
MM J120534-0745.2 (17)	* 668	691
MM J120522-0745.1 (18)	777	728
MM J120529-0744.8 (19)	* 805	837
MM J120509-0744.4 (20)	* 805	764
MM J120518-0744.1 (21)	* 668	691
MM J120543-0743.5 (22)	* 1036	1091
MM J120535-0743.4 (23)	* 805	800
MM J120501-0743.1 (24)	* 1036	1055
MM J120517-0743.1 (25)	980	1564
MM J120508-0743.1 (26)	946	928
MM J120518-0742.7 (27)	* 604	618
MM J120530-0741.6 (29)	836	837
MM J120528-0741.6 (30)	* 604	618
MM J120546-0741.5 (31)	1962	2365
MM J120514-0741.1 (32)	* 668	691
MM J120540-0741.0 (33)	* 668	691
MM J120509-0740.0 (34)	1151	1201
MM J120542-0739.6 (35)	* 805	837
MM J120516-0739.4 (36)	693	800
MM J120538-0739.3 (37)	* 1119	1164
MM J120538-0739.0 (38)	* 1036	1091
MM J120520-0738.9 (39)	1064	982
MM J120545-0738.8 (40)	1238	1346
MM J120544-0738.4 (41)	* 878	946
MM J120534-0738.3 (42)	762	800
MM J120518-0742.6 (43)	* 878	946

Note. — Col. (1) — MAMBO source.

Col. (2) — SFR based on the radio flux and the redshift estimate based on the radio-mm spectral index. Sources marked with * are not detected in the radio down to 40 μ Jy.

Col. (3) — SFR based on the mm flux.

all, our SFRD at different epochs is similar to extinction-corrected values obtained from UV/optical-selected surveys e.g., LBGs by Steidel, Giavalisco, Dickinson, & Adelberger (1996) and Steidel et al. (1999).

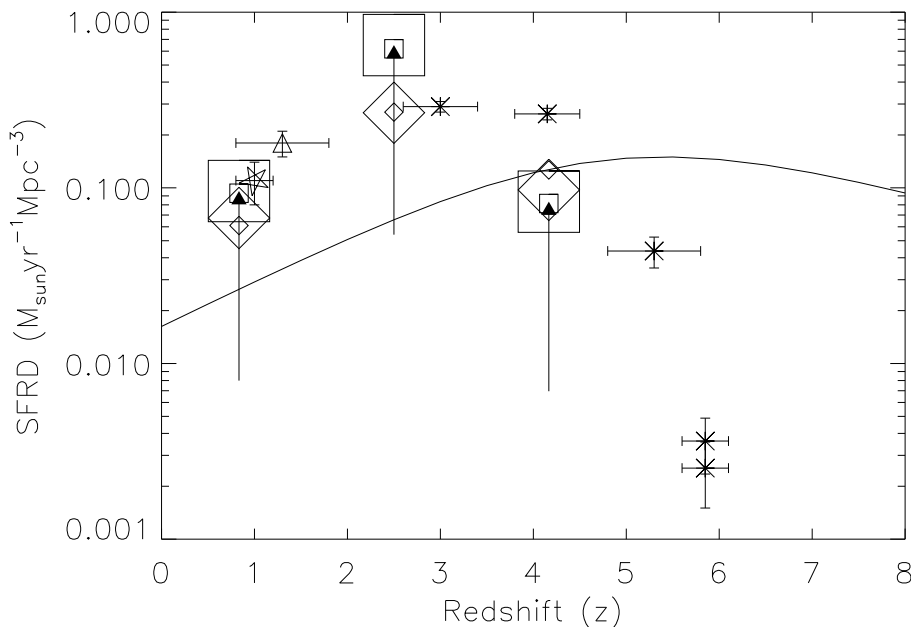


Figure 3.35 Star-formation-rate-density (SFRD) for different object classes at different epochs. The squares present the SFRD for the NDF MAMBO galaxies. The diamonds represent the corrected SFRD of SCUBA galaxies from the 8 mJy sample (Ivison et al., 2002). Big symbol shows the SFRD based on the (sub)mm and small symbols the SFR derived from the radio flux. The upward arrows represent the correction for missing observed sources we applied to the SFRD for the NDF MAMBO galaxies. The values of the 8 mJy survey presented in this diagram are also corrected. The radio-detected ERO sample presented by Smail et al. (2002b) is shown with the five pointed star. LBGs detected at different redshifts are plotted with crosses (Steidel, Giavalisco, Dickinson, & Adelberger, 1996; Steidel et al., 1999; Lehnert & Bremer, 2003; Stanway, Bunker, & McMahon, 2003a; Stanway et al., 2003b). H α -selected objects are shown as triangles (Yan et al., 1999). The curve indicates the cosmic star-formation history of the universe computed by Springel & Hernquist (2003a,b) and Hernquist & Springel (2003) using SPH simulations.

Table 3.8. SFRD

Redshift bin (1)	MAMBO NDF sample		8 mJy survey	
	SFRD _{1.4 GHz} (2)	SFRD _{1.2 mm} (3)	SFRD _{1.4 GHz} (4)	SFRD _{850 μm} (5)
0.0-1.7	0.0078	0.0080	0.0051	0.0056
1.7-3.4	0.0516	0.0541	0.0224	0.0223
3.4-5.0	0.0068	0.0070	0.0105	0.0081

Note. — Col. (1) — Redshift bins.

Col. (2-5) — SFRD in $M_{\odot}\text{yr}^{-1}\text{Mpc}^{-3}$ without correction for the whole source population.

In a recent series of papers, Springel & Hernquist (2003a,b) and Hernquist & Springel (2003) studied the star formation history from the dark ages ($z \sim 20$) to the present by using smooth-particle hydrodynamics (SPH) simulations of hierarchical formation in a Λ cold dark matter universe. The models predict the peak of star formation at $z_{peak} \sim 5-6$ and the slope between $z = 0$ and $z \sim 1-2$ to be shallower than seen in UV/optical observations. But considering the great uncertainties of the different observational results e.g., extinction correction, surface-brightness dimming (Lanzetta et al., 2002), the models are in good agreement with observations.

3.4 What Causes the Difference between SCUBA and MAMBO Populations?

In Tab. 3.9, we list the main properties of the MAMBO 1.2 mm survey in the NTT Deep Field and the SCUBA 8 mJy survey. The most striking difference between these two surveys is the faintness of the MAMBO counterparts in the optical/near-infrared. The difference in brightness of about 2 mag between typical MAMBO and SCUBA counterparts is a surprising result, given the selection of these objects at fairly similar wavelengths and in a region of the rest-frame spectral energy distribution that does not show prominent breaks or features. We discuss in the following several potential contributors to this difference.

Given the faintness of the targets relative to instrumental sensitivities at *all* wavelengths, the identification process may still make mistakes. For the NDF MAMBO sources, some of the nearly 3σ radio sources are clearly uncertain and may lead to uncertain identifications. We have argued above, however, that eliminating the uncertain sources as classified in § 3.2.1 does not change the magnitude distribution of the MAMBO counterparts significantly. For the SCUBA sources, similar problems may be present at the limit of the radio data. In addition, there are now examples in which intensified identification efforts have rejected previously adopted bright counterparts and lead to a significant upward revision of the proposed counterpart magnitudes, the most notable being these three objects HDF 850.1 (Hughes et al., 1998; Richards, 1999; Downes et al., 1999; Dunlop et al., 2002), SMM J00266+1708 (Frayser et al., 2000) and SMM J09431+4700 (Neri et al., 2003). Removing a few of the brightest or bluest 8 mJy counterparts from Fig. 3.26 does not fully explain the difference from the MAMBO counterparts, however. Noting all these uncertainties, we do not see any compelling evidence for systematic misidentifications. Identification uncertainties are also related to the presence of “complex” objects with several components, e.g., one of the mm galaxies discussed by Bertoldi et al. (2000). Ivison et al. (2002) emphasize the role of such objects in the 8 mJy survey. Again, the example of SMM J09431+4700 (Neri et al., 2003), where the submm and CO source H7 is $4''$ from the object H6 with a very similar (optical) redshift, indicates that such grouping or clustering exists. In such cases, the (sub)mm source could relate to just one or to all of the components. We find only three such objects in our sample. For object No. 10 we have preferred one component because of photometric redshift arguments. For objects 29 and 42 there is more uncertainty on whether to identify the source with one or several components, but even the sum of the components would not make a “bright” counterpart.

Optical/near-infrared magnitude differences could also reflect a significant difference in the redshift distribution of the SCUBA and MAMBO populations. The effect in the optical/near-infrared will obviously depend on the intrinsic SEDs; assuming ULIRG-like SED shapes and fixing the (sub)mm flux, explaining the magnitude difference would require a difference in median redshifts of the order $\Delta z = 1 - 2$ (Fig. 3.29). Chapman, Blain, Ivison, & Smail (2003b) suggest a median redshift of 2.4 for bright submm galaxies from optical spectroscopy. Some of these optical redshifts still require confirmation via CO detections, and it is natural to assume that the optical redshifts are still biased towards the optically bright and low-redshift end of the population. This as-

Table 3.9. Comparison between the MAMBO 1.2 mm and the SCUBA 8 mJy survey

Property (1)	Comment (2)
Brightness of the counterpart	1.2 mm sources are ~ 2 mag fainter in I and K
Morphology of the counterpart	the fraction of complex SCUBA counterparts is higher
ERO as counterpart	fraction in the two surveys is similar
Optically faint radio sources	the recovery rate of OFRS is low in both
Star-formation rate density	for all redshift epochs, the SFRD is consistent within the errors

sumption is supported by SED arguments (§ 3.3.3). Even at redshifts around or somewhat above 3, however, both SCUBA and MAMBO observations effectively sample the long-wavelength side of the rest-frame far-infrared SED peak, unless the intrinsic dust temperatures are extremely cold. Evidence that both wavelengths sample the long-wavelength side is indeed present in many of the best-studied SCUBA sources (e.g., Ivison et al., 1998; Downes et al., 1999; Gear et al., 2000; Ivison et al., 2000a; Lutz et al., 2001). At such redshifts, it will be difficult to construct a redshift distribution that fully accounts for the observed differences. Redshift estimates for the SCUBA population from the radio/submm spectral index (Carilli & Yun, 2000), and from estimates trying to more fully include the rest-frame far-infrared part of the SED under the assumption of SEDs similar to local (U)LIRGs (Yun & Carilli, 2002; Wiklind, 2003; Aretxaga et al., 2003) indicate median redshifts in the range 2.5 to 3.5 with the possibility of a significant high-redshift tail (Wiklind, 2003; Aretxaga et al., 2003). However, it is important to note that such analyses suffer from possible template mismatches between high- and low-redshift sources and from using an unrealistically narrow range of SED types and properties when making redshift estimates. For example, Aretxaga et al. (2003) may place undue weight on individual templates to constrain the possible redshift range. This means that the low-redshift SEDs that they employ in these analyses are assumed to be good analogues for those of the high-redshift sources. In addition, a substantial number of higher redshift $z > 4$ sources in the MAMBO population is also suggested by the $850 \mu\text{m}/1.2 \text{ mm}$ ratios presented by Eales et al. (2003), albeit with large uncertainties due to the technical difficulties of the method. For the objects overlapping with our study (Nos. 1, 3, 16, 25, 31), their $850 \mu\text{m}/1.2 \text{ mm}$ redshift estimates can be compared with the detections in various optical pass-bands — if they are at high redshift, these objects should be unde-

tected dropouts in optical bands. With the possible exception of No. 3 (best submm/mm estimate $z \sim 4.25$ but a marginal detection in B), the results are consistent, and even No. 3 behaves as expected considering the uncertainties. In summary, while there may be a high-redshift tail of the (sub)mm population that is preferentially sampled by MAMBO, we find it difficult to explain the magnitude differences by a bulk redshift difference. This view is consistent with Fig. 3.32, which does not show the “diagonal” offset between the two sets that is expected for such redshift offset.

Because of the degeneracy of redshift and dust temperature in interpretations of the submm/radio spectral energy distributions (e.g., Blain, Barnard, & Chapman, 2003), similar arguments can be made with respect to a possible separation of the MAMBO and SCUBA populations by dust temperature, for example due to an evolutionary difference between MAMBO and SCUBA objects. One should note, however, the need for significant obscuration in the rest-frame optical when invoking “cool” rest-frame FIR SEDs, see Fig. 3.33.

Our results here indicate that there are real differences between the counterpart brightnesses and perhaps redshifts of the SCUBA and MAMBO populations. On the sole basis of SED arguments, it is difficult to robustly weight the contributions to these differences due to real redshift offsets or SED differences of the mm and submm selected populations, in comparison with caveats due to small sample statistics, cosmic variance, and identification difficulties. Significant progress in settling these issues will come from tests of proposed identifications with available optical redshifts through CO measurements (e.g., Neri et al., 2003), and from future direct submm/mm redshift measurements for the fainter part of the population, most likely through wide-band searches for CO emission.

Appendix A

Photometric Redshifts of Sources in the NDF

For the determination of redshifts of large samples of galaxies, the application of photometric redshift methods is essential. With these techniques, we obtain redshift estimates for objects which either lie beyond observational spectroscopic limits (e.g., $R \sim 25$ mag at a 8 m class telescope like the VLT), or whose spectral features fall outside of observing windows and/or in the “redshift desert”¹ spanning z from 1.4 to 2.5. Thus in the recent years, photometric redshift methods were widely used in order to derive redshift estimates for large samples of objects. The basic idea of this technique is that we compare the observed broad-band properties of galaxies with SED predictions and focus on broad features like spectral breaks instead of emission/absorption lines which are critical for spectroscopic derived redshifts. A central question is how reliable and accurate are the derived photometric redshifts; but several groups have obtained significant accuracy for their photometric redshift, e.g., Fernández-Soto, Lanzetta, & Yahil (1999) for photometric redshifts in the Hubble Deep Field North (Williams et al., 1996). Similar results were reported for the K-20 survey (Cimatti et al., 2002). Thus, with accurate photometric redshifts we are in a position to discuss the individual properties of galaxies as a function of redshift on a solid basis.

Since our optical/NIR objects close to the interferometric position lack of redshifts, we applied the photometric redshift code *hyperz* (Bolzonella, Miralles, & Pelló, 2000). We use

¹Recently, Steidel et al. (2004) presented a new strategy to determine spectroscopic redshifts in the “redshift desert”.

the spectroscopic information obtained for 63 objects in the NTT Deep Field to determine the accuracy and reveal possible problems of our photometric redshifts. The spectroscopic redshifts of this sample range between $z = 0.07$ and 1.69 .² The optical/near-infrared properties of these objects cover a wide range of brightness, color and morphology. To test the accuracy of our photometric redshifts, we compare z_{spec} and z_{phot} ³. In Fig. A.1, we show the spectra of three random objects and overplot the best SED fit based on the BVRIzJK data set. In the top left panel of Fig. A.2, z_{phot} versus z_{spec} is presented, in the top right z_{spec} versus $z_{diff}/(1+z_{spec})$, in the bottom left (R-K) versus $z_{diff}/(1+z_{spec})$, and in the bottom right R versus $z_{diff}/(1+z_{spec})$. The dispersion $\sigma_{z_{spec}-z_{phot}}$ is 0.17. In general, a good agreement between z_{spec} and z_{phot} is found. Only in a few cases is the difference between z_{spec} and z_{phot} significant. For 40 % of the outliers⁴ we note that the secondary peak of the probability function lies closer to z_{spec} than the primary peak. For around a quarter of our 63 objects (these cases are marked with an arrow in the upper left panel of Fig. A.2), the secondary peak of the probability function would give a smaller z_{diff} . In the top left panel, these cases are presented by up- or down-arrows. A trend is seen such that in sources with $z < 0.3$ the photometric redshift is overestimated and in objects with $0.7 < z < 1.3$ the photometric redshift is underestimated. Kashikawa et al. (2003) also applied *hyperz* to ground-based images and reported a similar result. The majority of counterparts of MAMBO galaxies have very/extremely red colors, therefore, we investigated whether there is a dependency between the accuracy $z_{diff}/(1+z_{spec})$ and the color. No relation between these two parameters is found, as shown in the bottom left panel of Fig. A.2. We note however that *hyperz* does not contain an observed SED of an ultraluminous infrared galaxy (ULIRG; to which the SED of mm sources may be similar), although it does allow for a range of additional extinction to be added to the model that may approximate an SED similar to that seen in ULIRGs. The photometric redshift accuracy of faint objects (the majority of objects in MAMBO beams are rather faint) is not significantly worse than for bright objects, as demonstrated by the bottom right panel in Fig. A.2. To summarize, this analysis of the reliability of photometric redshifts justifies our use of optical/NIR photometric redshifts calculated with *hyperz* for the

²Sample includes data from MXU-spectroscopy of optical sources near the nominal MAMBO bolometer position discussed in § 2.4; MXU-spectroscopy of EROs will be presented in Lehnert et al. 2004 (in prep.); and ESO Science Verification data (http://www.eso.org/science/ut2sv/NDFs_release.html).

³ $z_{diff} = z_{spec} - z_{phot}$

⁴ $z_{diff} > 3 \times \sigma_{z_{spec}-z_{phot}}$

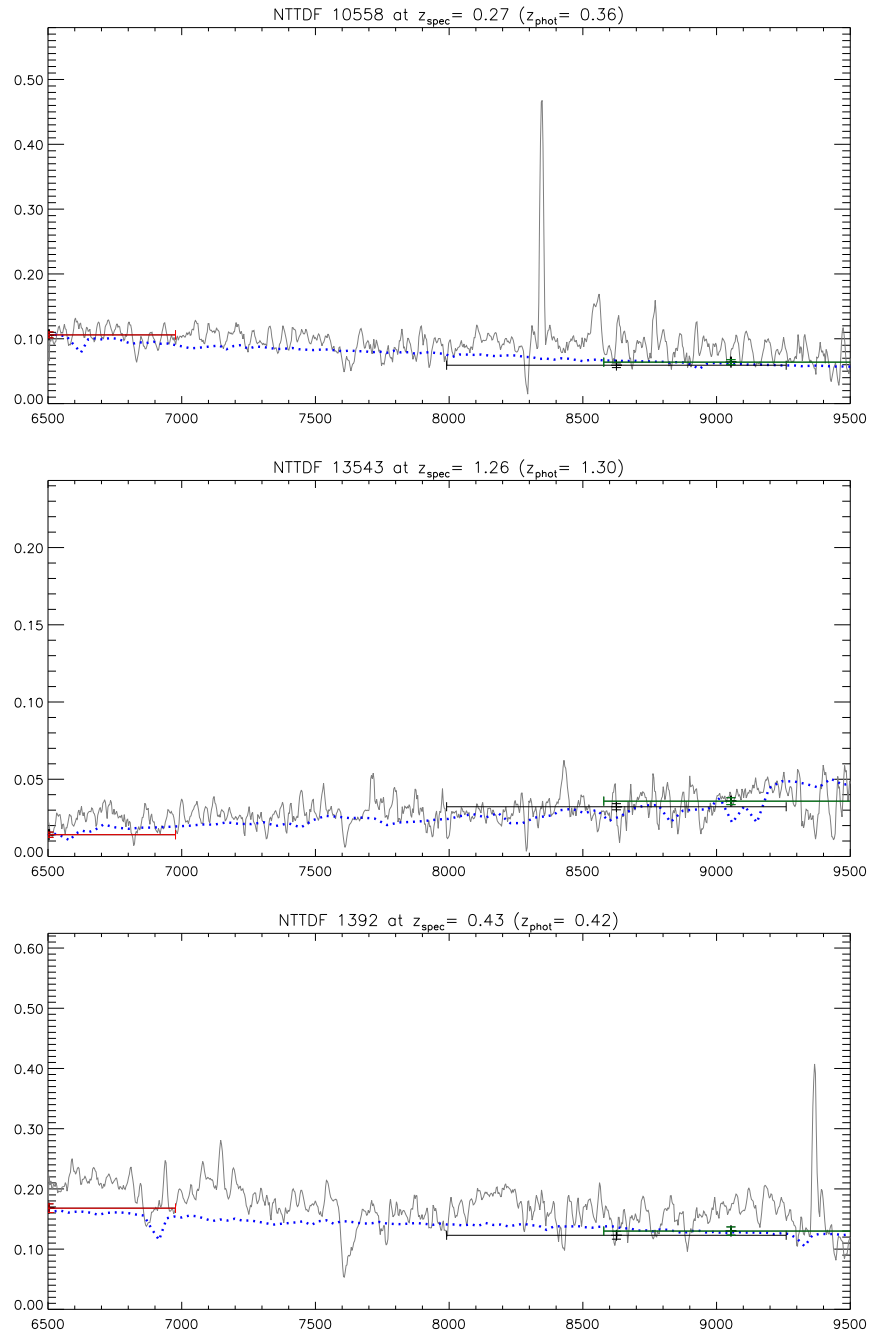


Figure A.1 For three random objects, we overlay the observed FORS2-MXU spectrum (solid line) with the best fit (dashed line) based on the broad-band data set. The broad band data points are presented with error bars. Ordinate: unit of the flux density is $2.0 \times 10^{-17} \text{ erg cm}^{-2} \text{ s}^{-1} \text{ \AA}^{-1}$. Abscissa: unit of the wavelength is \AA .

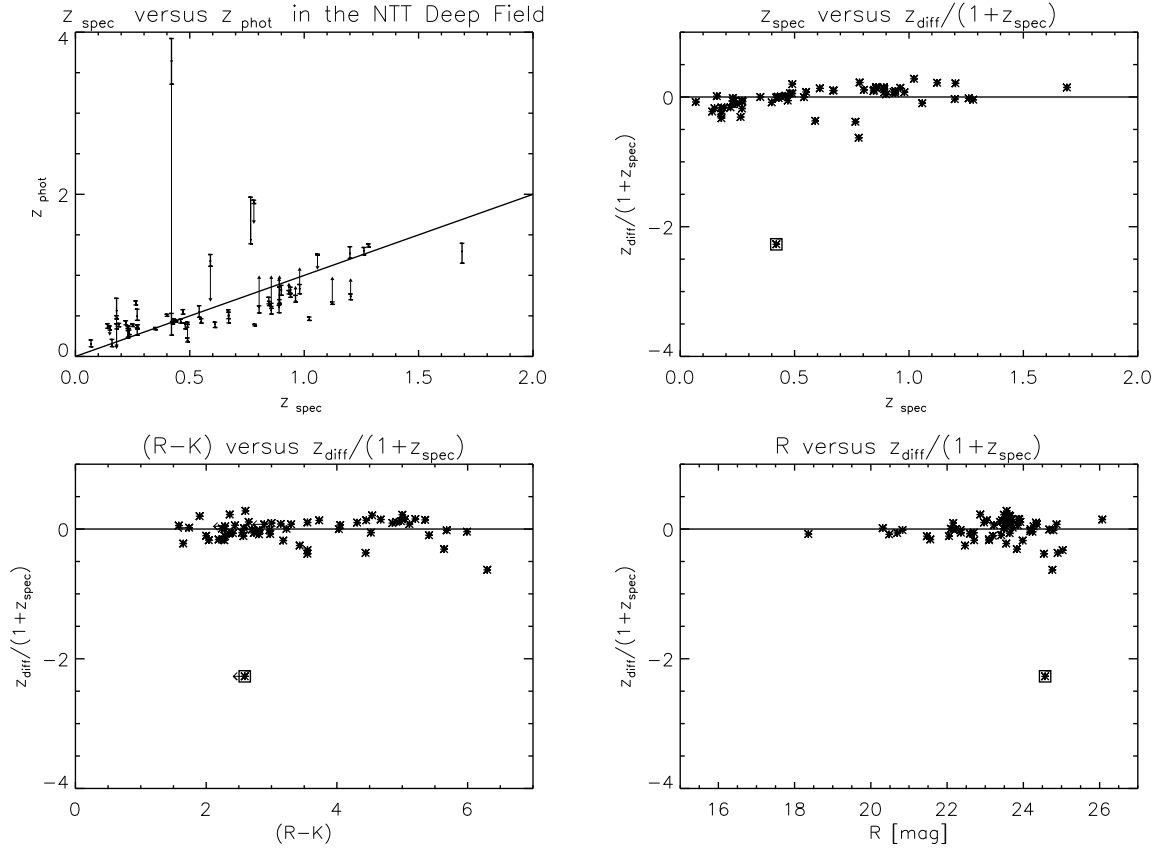


Figure A.2 *Top Left*: Spectroscopic redshifts versus photometric redshifts (based on *hyperz*) for sources in the NTT Deep Field. In cases where the z_{phot} of the second-order probability lies closer to z_{spec} , we indicate this by up- or down-arrows. *Top Right*: z_{spec} vs. $z_{\text{diff}}/(1+z_{\text{spec}})$. *Bottom Left*: $(R-K)$ vs. $z_{\text{diff}}/(1+z_{\text{spec}})$. *Bottom Right*: R vs. $z_{\text{diff}}/(1+z_{\text{spec}})$. We note that the photometric redshift (0.39) of the second-order probability of the outlier enclosed by a box lies within the errors to $z_{\text{spec}} = 0.42$.

interpretation/identification of optical and near-infrared objects near the interferometric positions.

We present the photometric redshifts of the optical and near-infrared objects near the interferometric positions of MAMBO 1.2 mm sources in the NTT Deep Field and listed in Tab. 3.4. For presentation purposes, we show in Fig. A.3 both the best fit to the broadband observations, used to derive the photometric redshifts and the probability function versus redshift. The main parameters for the best fit are listed in the plot. Finally, we provide an example parameter file showing the setup used in *hyperz* in Fig. A.4.

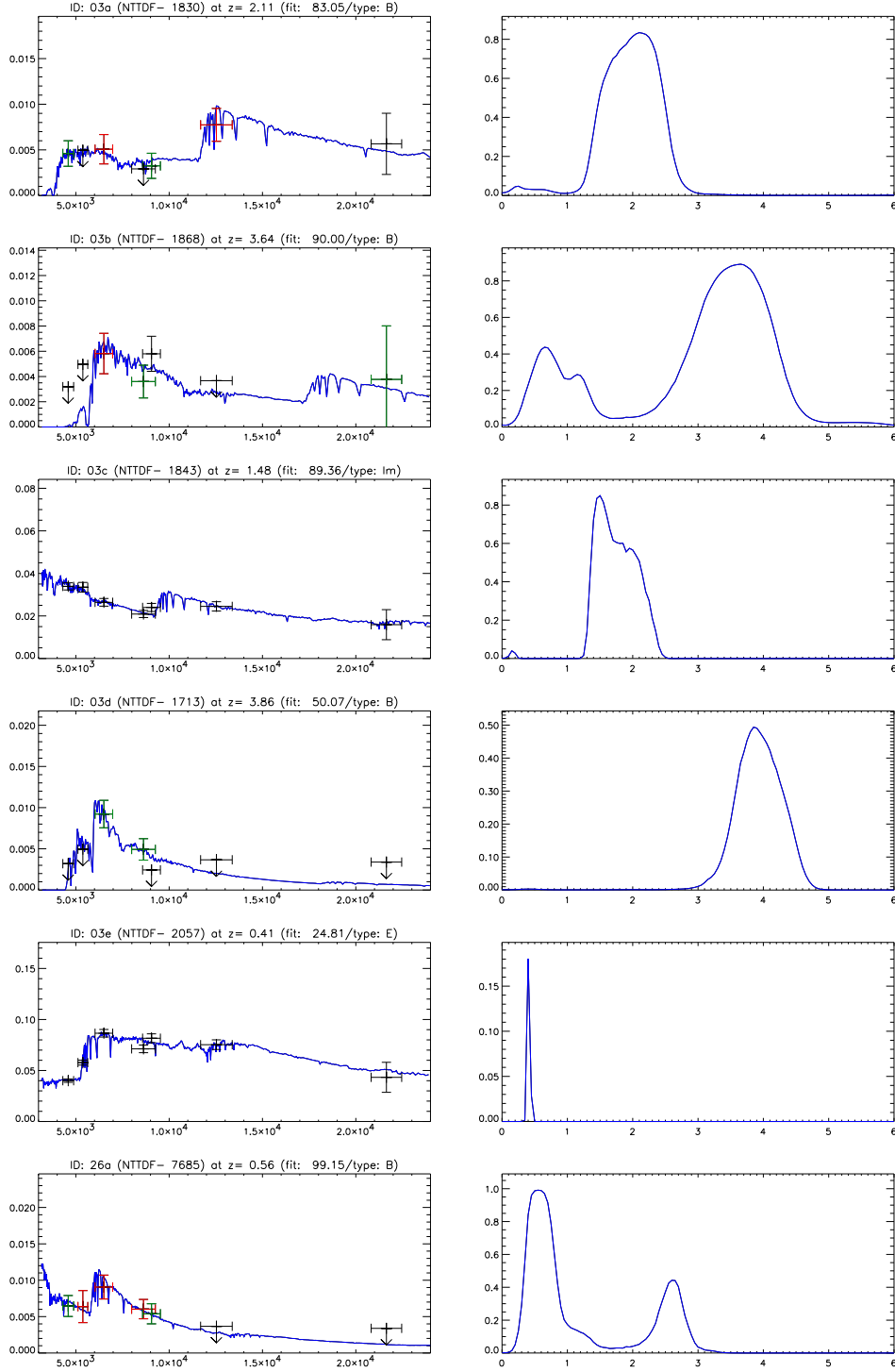


Figure A.3 *Left panel*: Best-fit SED of objects close to the interferometric positions (see Tab. 3.4) are plotted on the data points with error bars or limits marked by arrows. A green or red data point corresponds to an object only tentatively (indicated by ‘ \approx ’) or not (indicated by ‘!’) picked up by the eye in the visual inspection in this band. For each object, we give the ID, the photometric redshift, the probability of the best fit and the SED template used (B = Burst; E = Elliptical; Sc = Spiral Type c; Im = Irregular). Ordinate: unit of the flux density is $2.0 \times 10^{-17} \text{ erg cm}^{-2} \text{ s}^{-1} \text{ \AA}^{-1}$. Abscissa: unit of the wavelength is \AA . *Right panel*: Probability function.

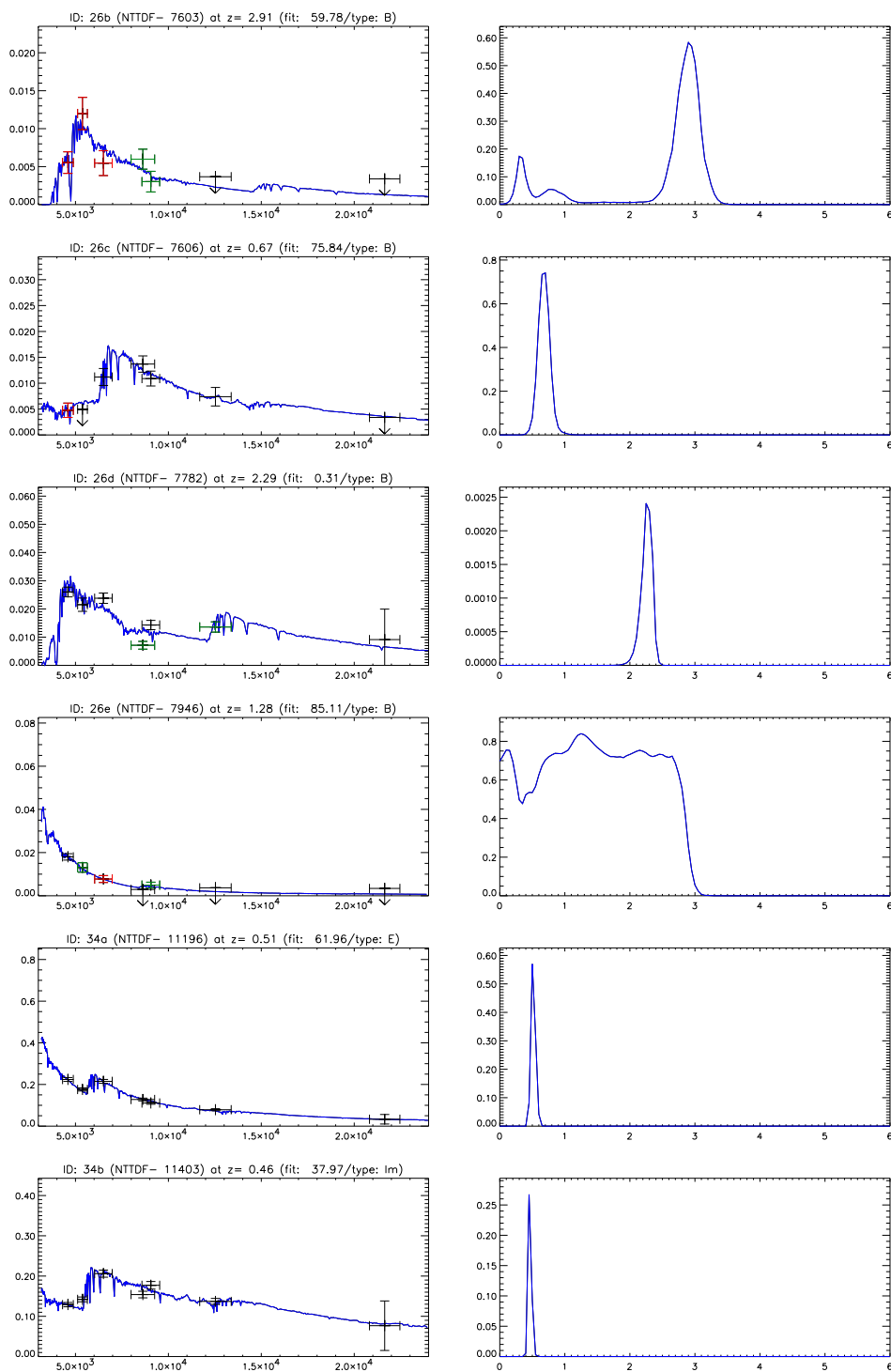


Figure A.3 (cont'd)

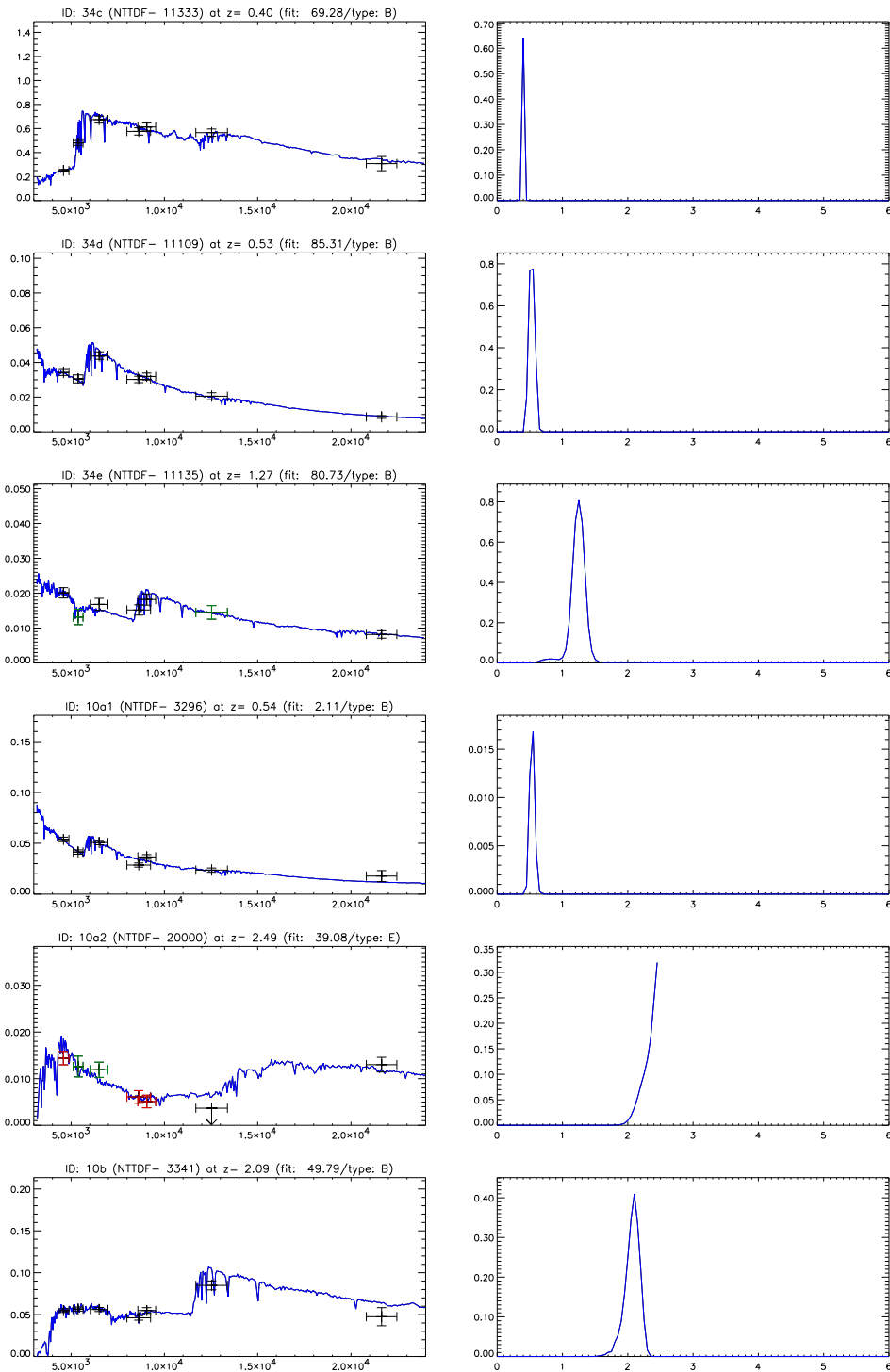


Figure A.3 (cont'd)

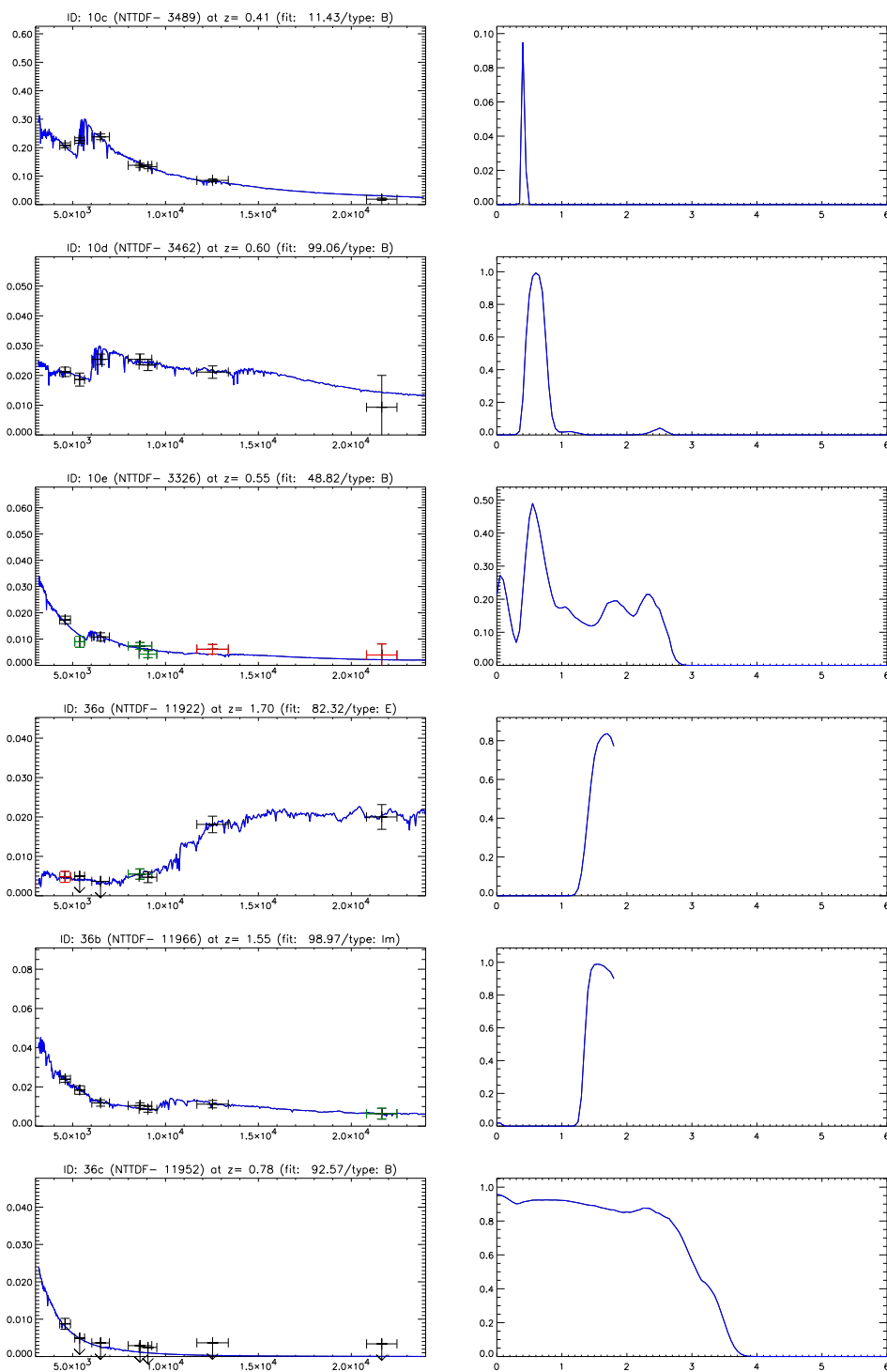


Figure A.3 (cont'd)

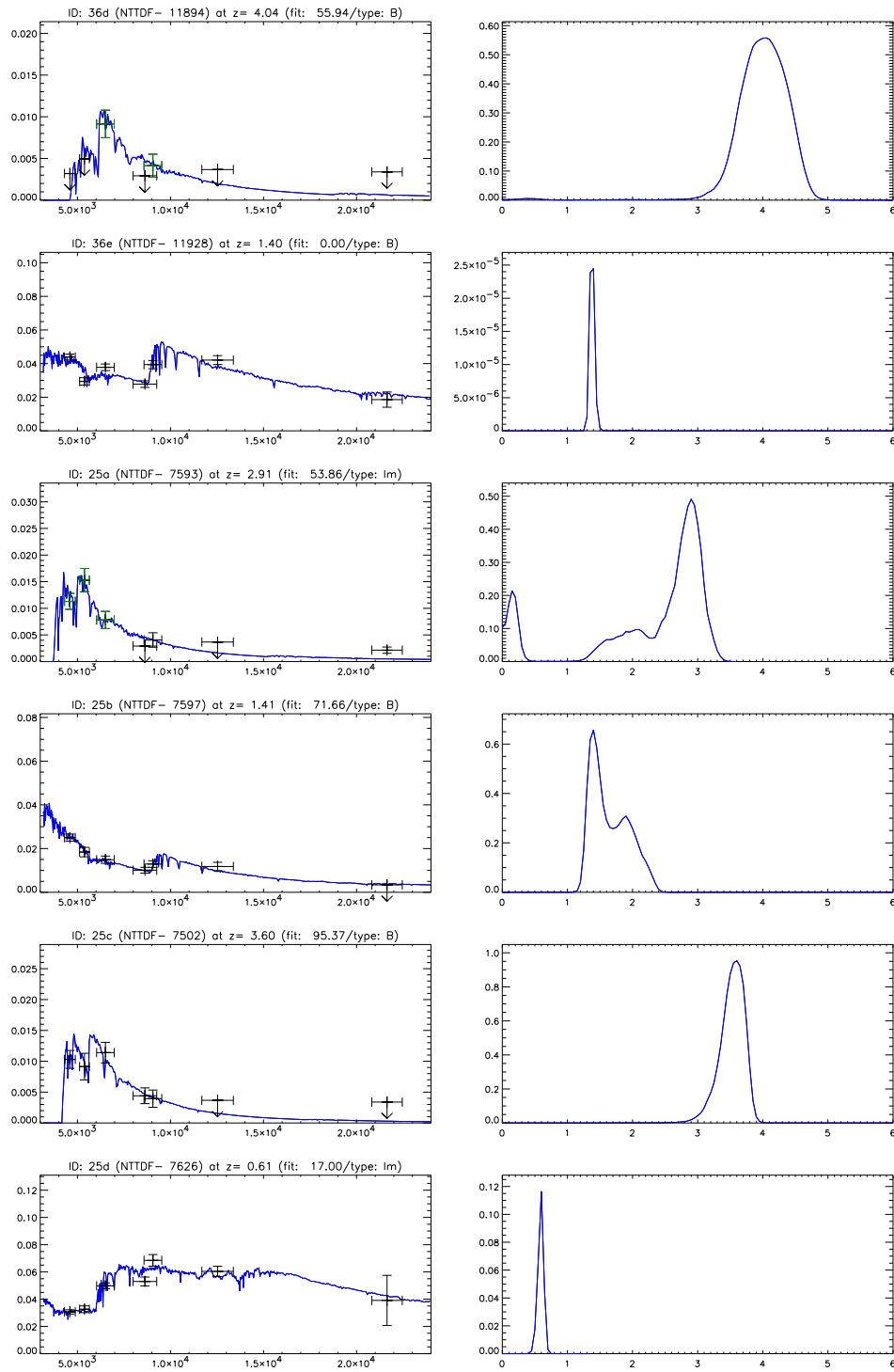


Figure A.3 (cont'd)

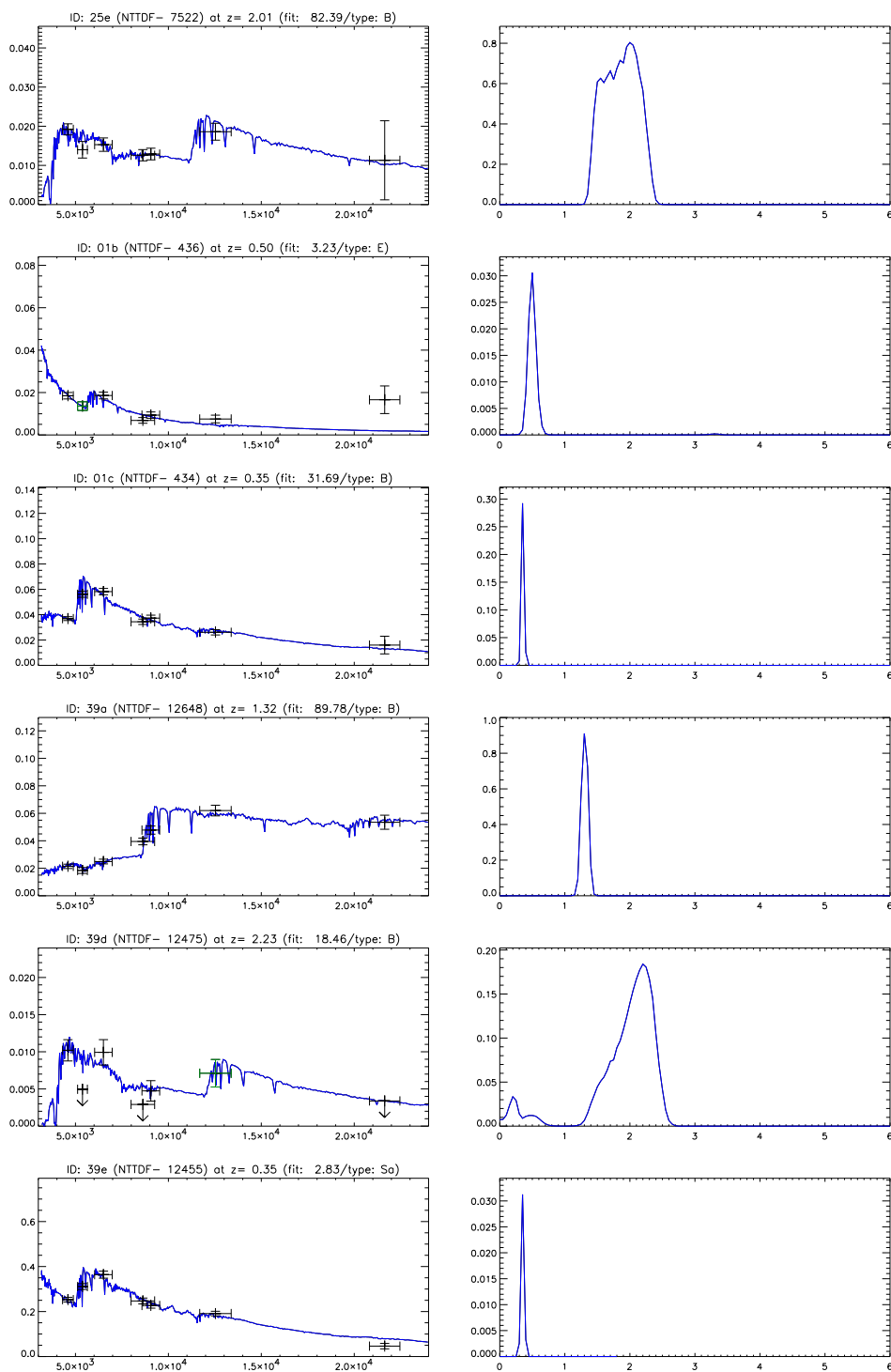


Figure A.3 (cont'd)

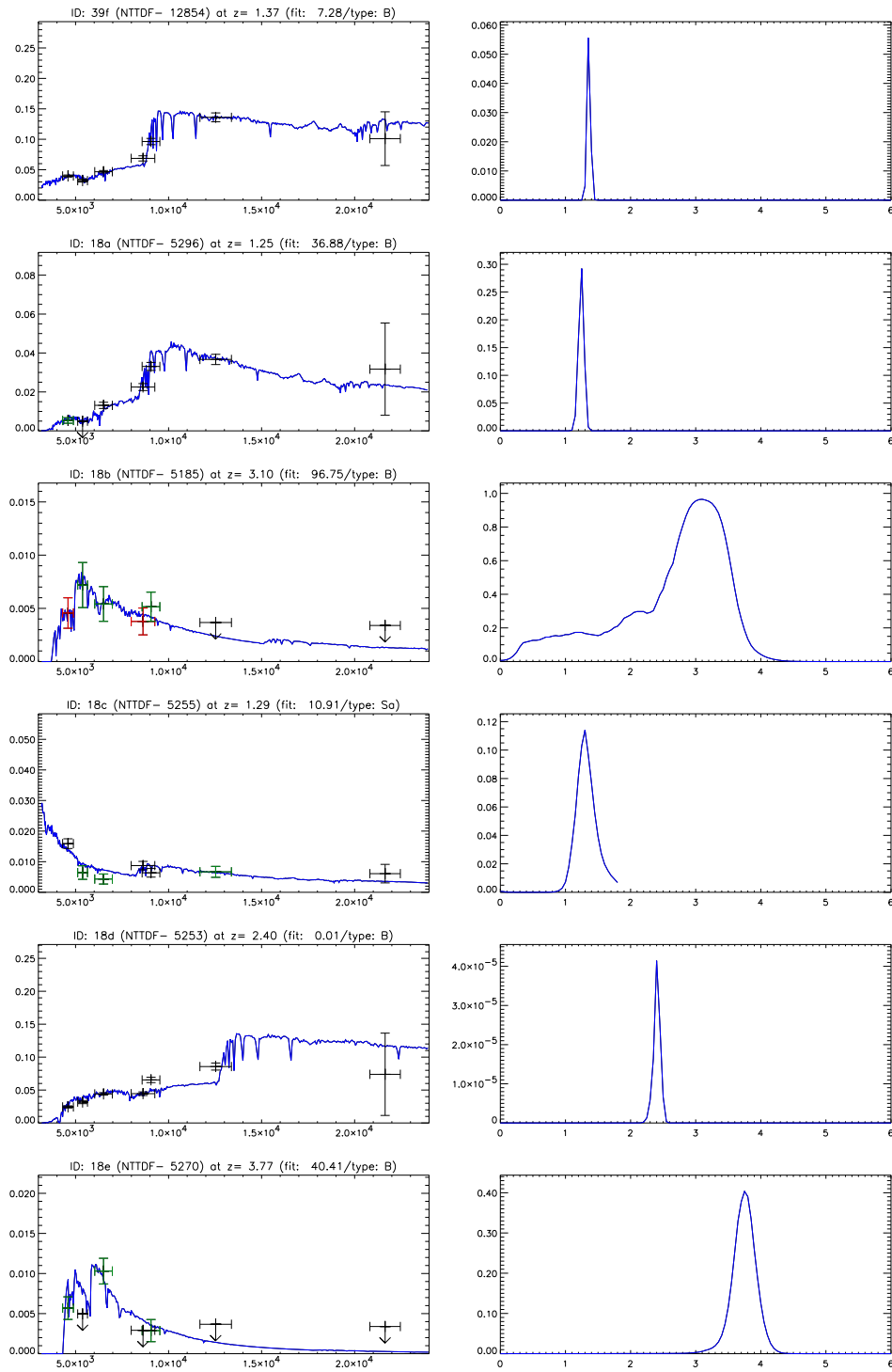


Figure A.3 (cont'd)

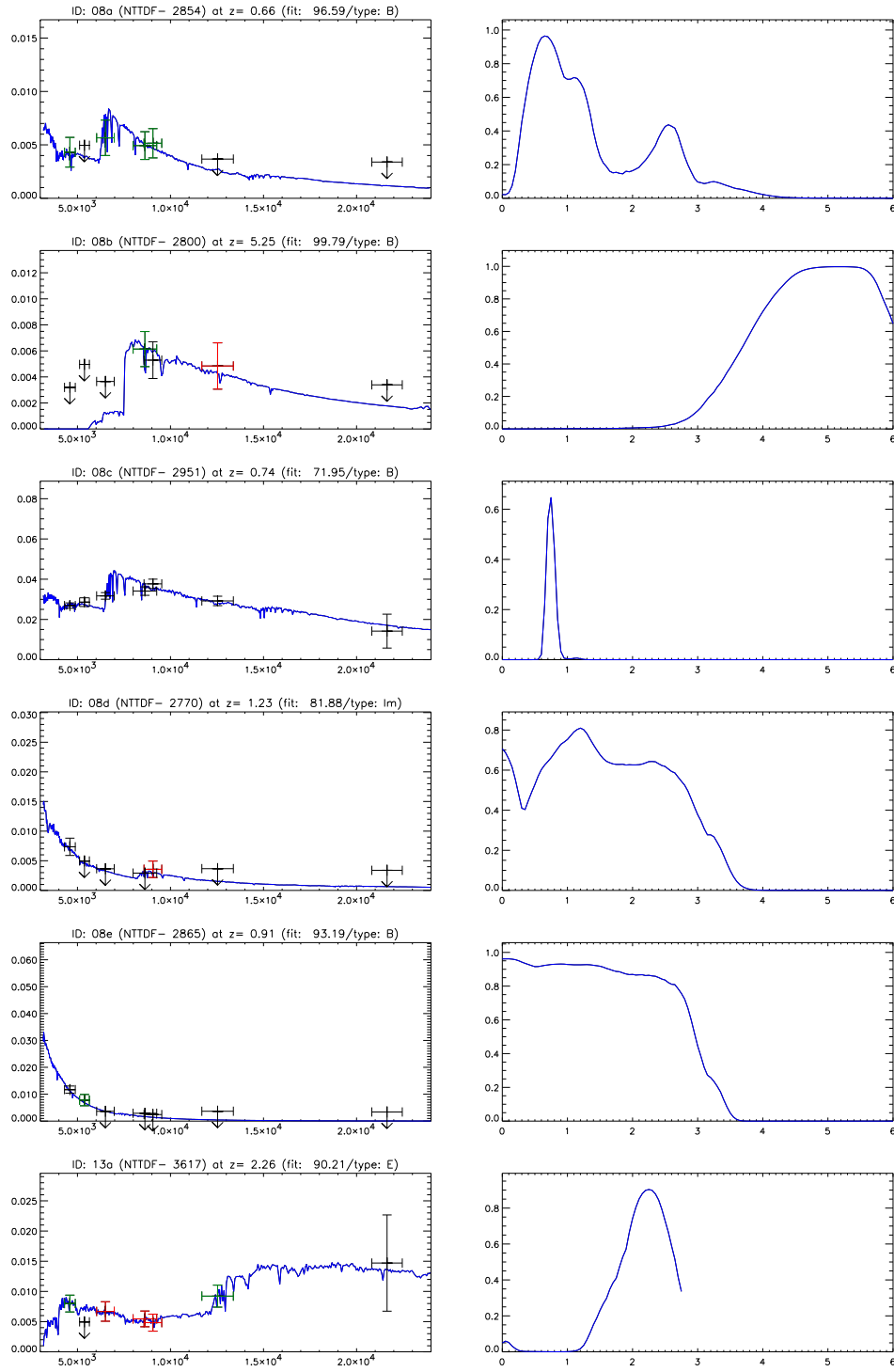


Figure A.3 (cont'd)

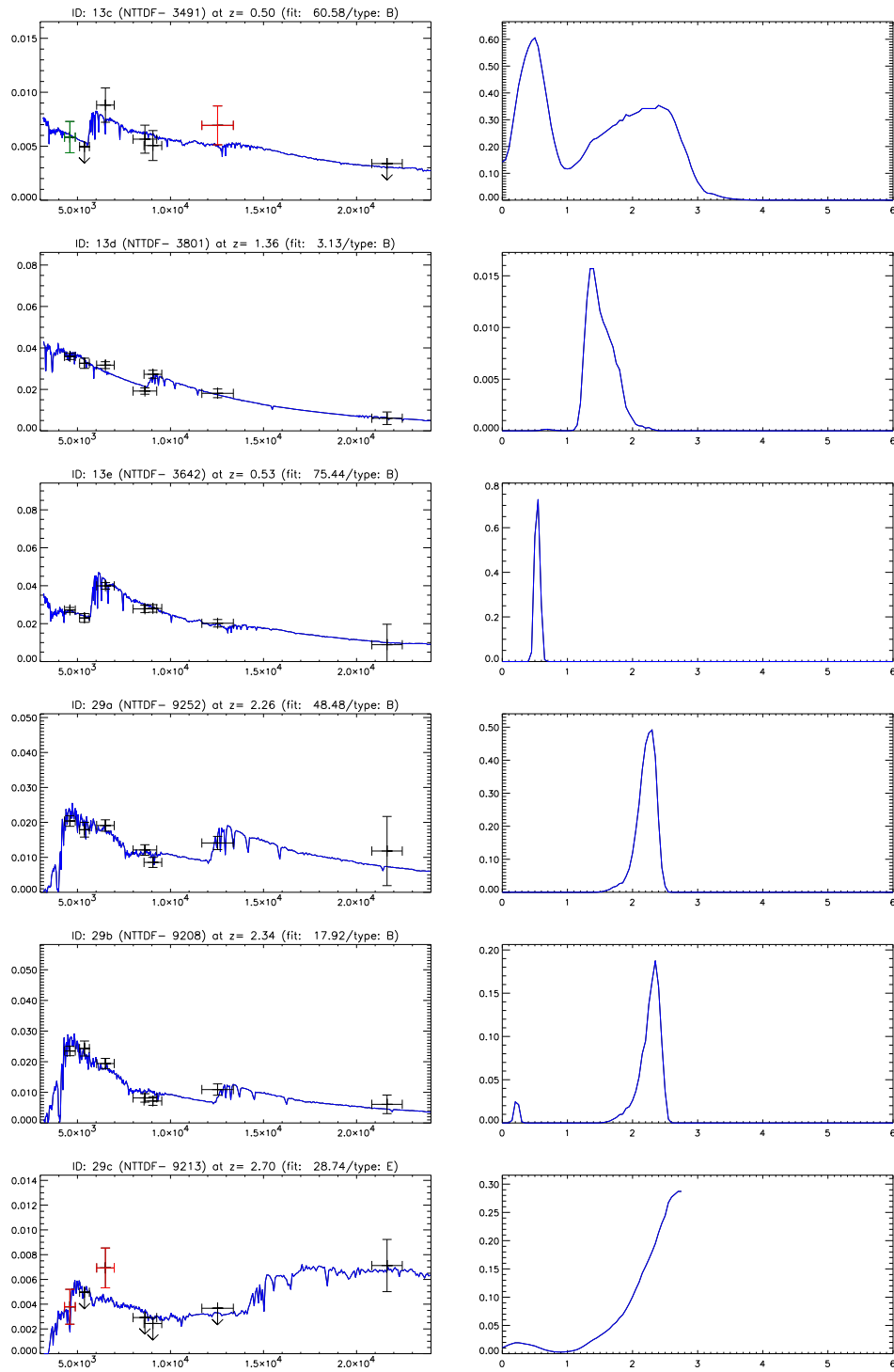


Figure A.3 (cont'd)

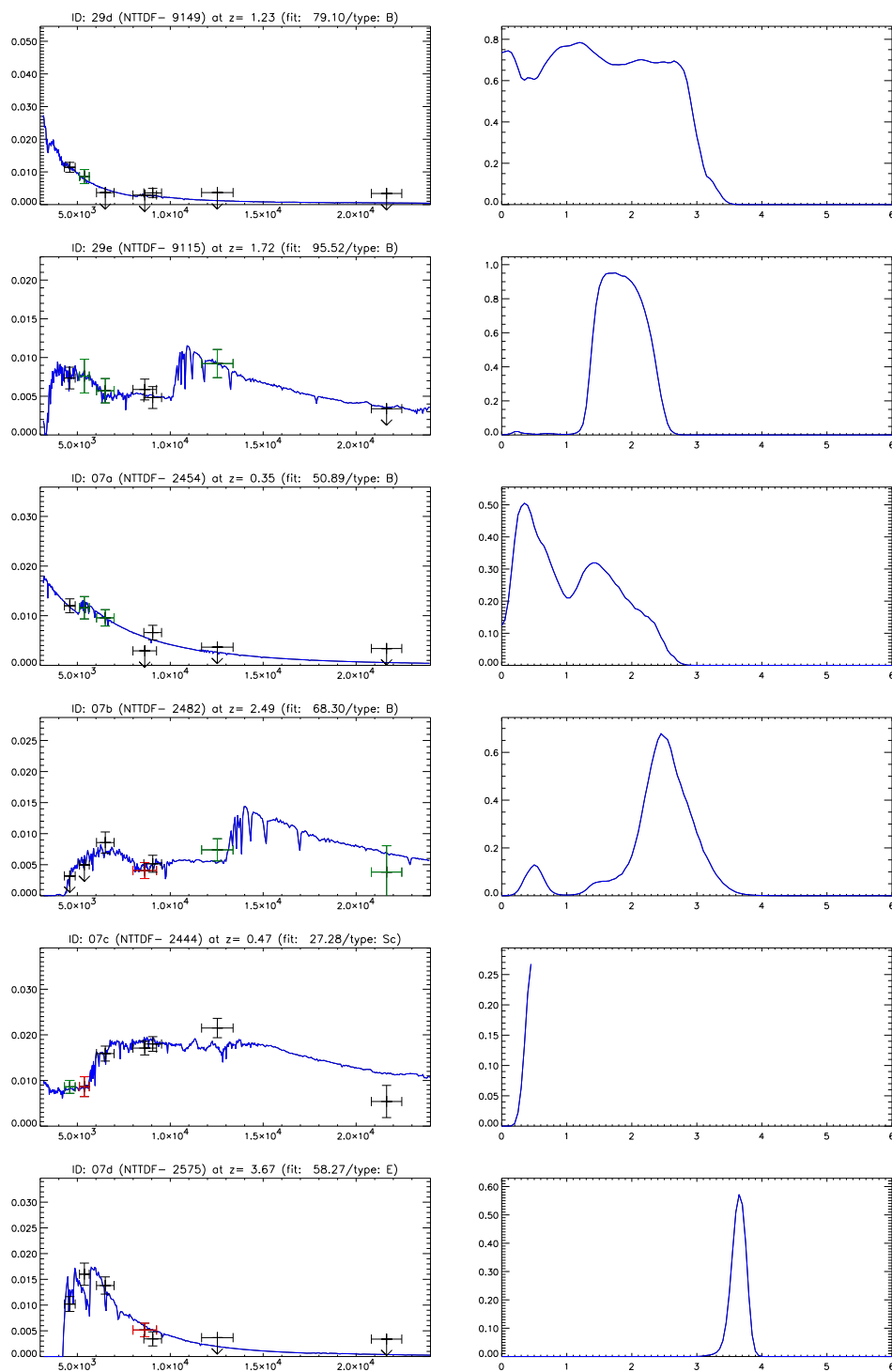


Figure A.3 (cont'd)

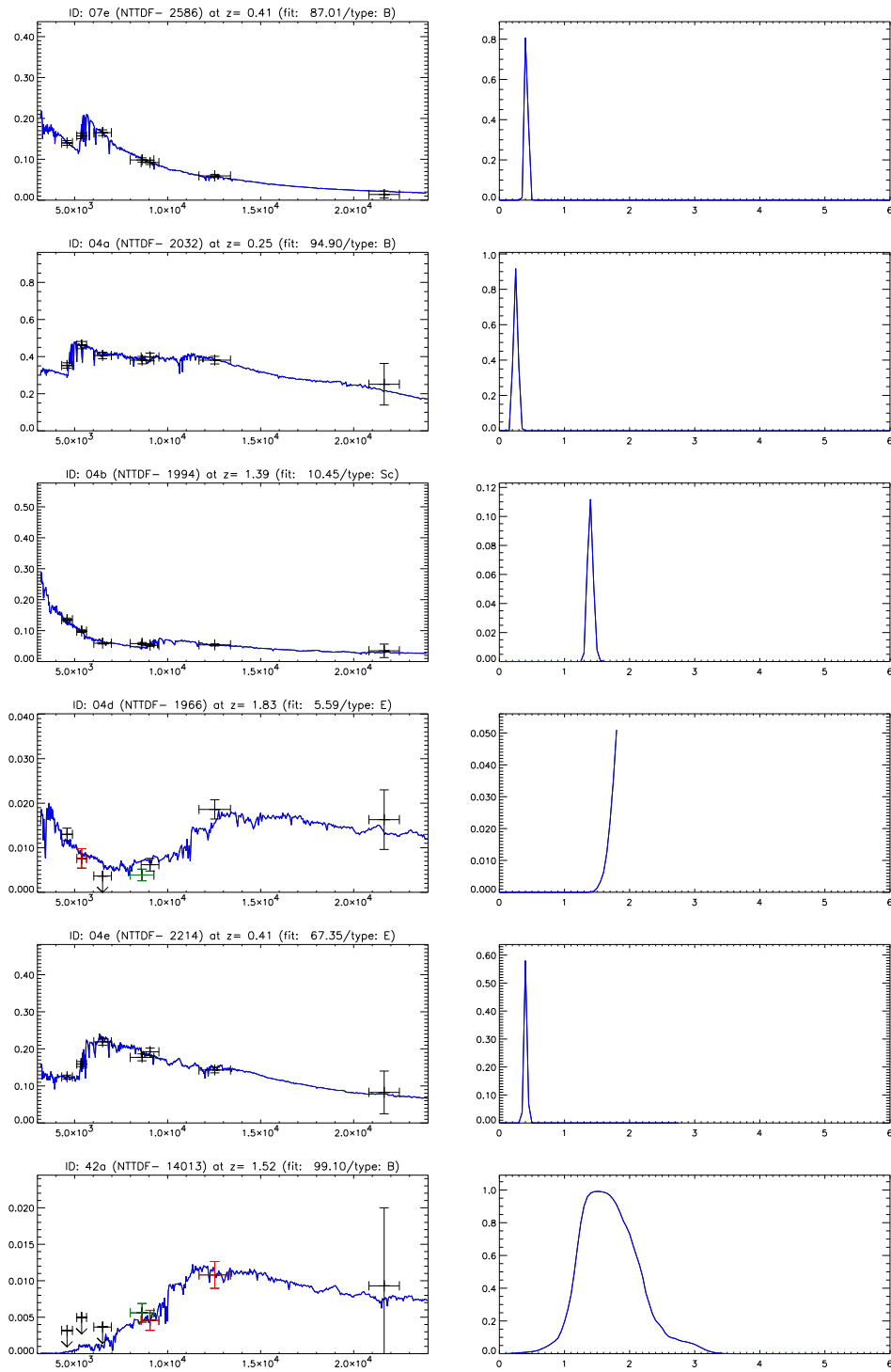


Figure A.3 (cont'd)

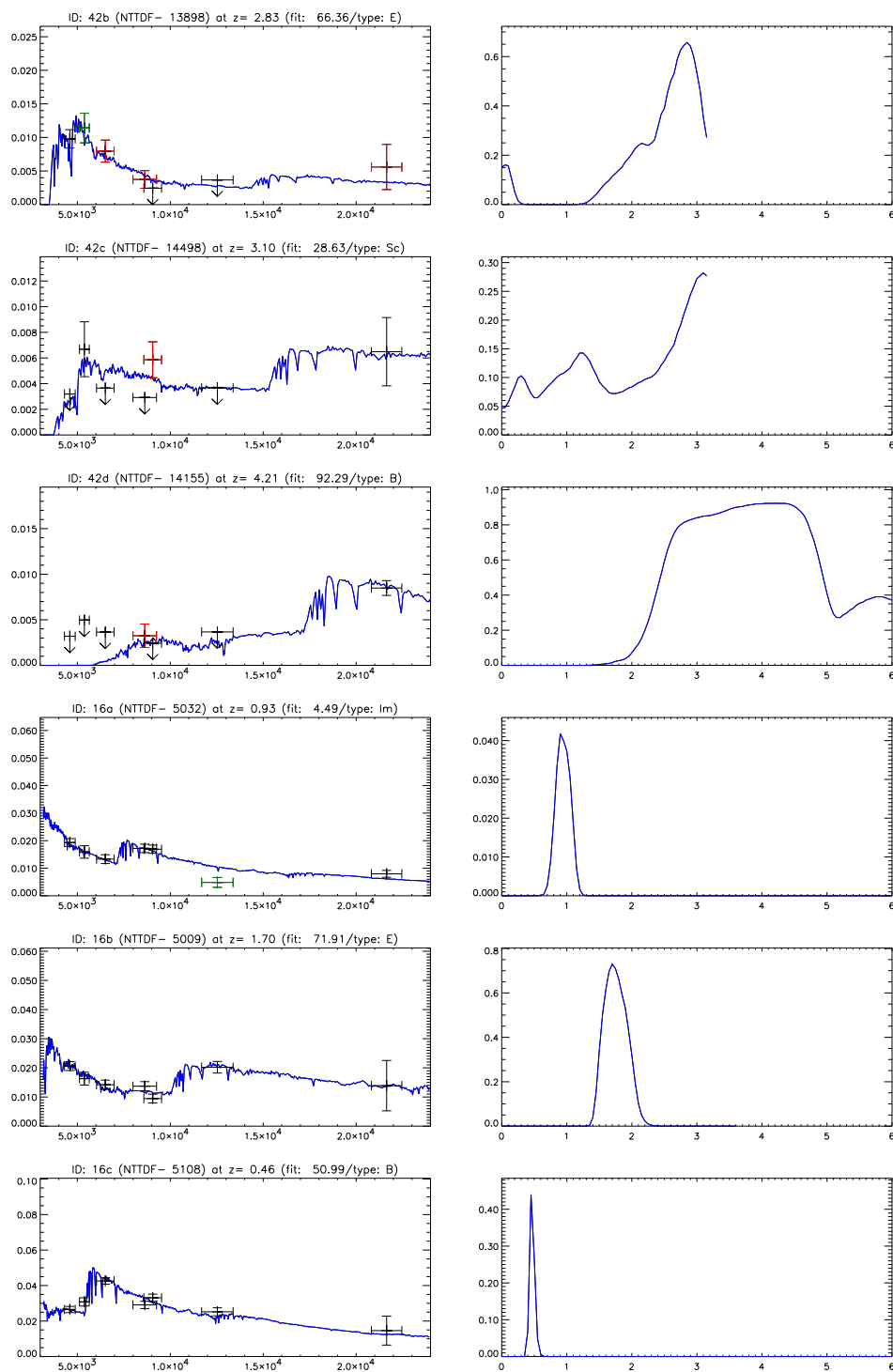


Figure A.3 (cont'd)

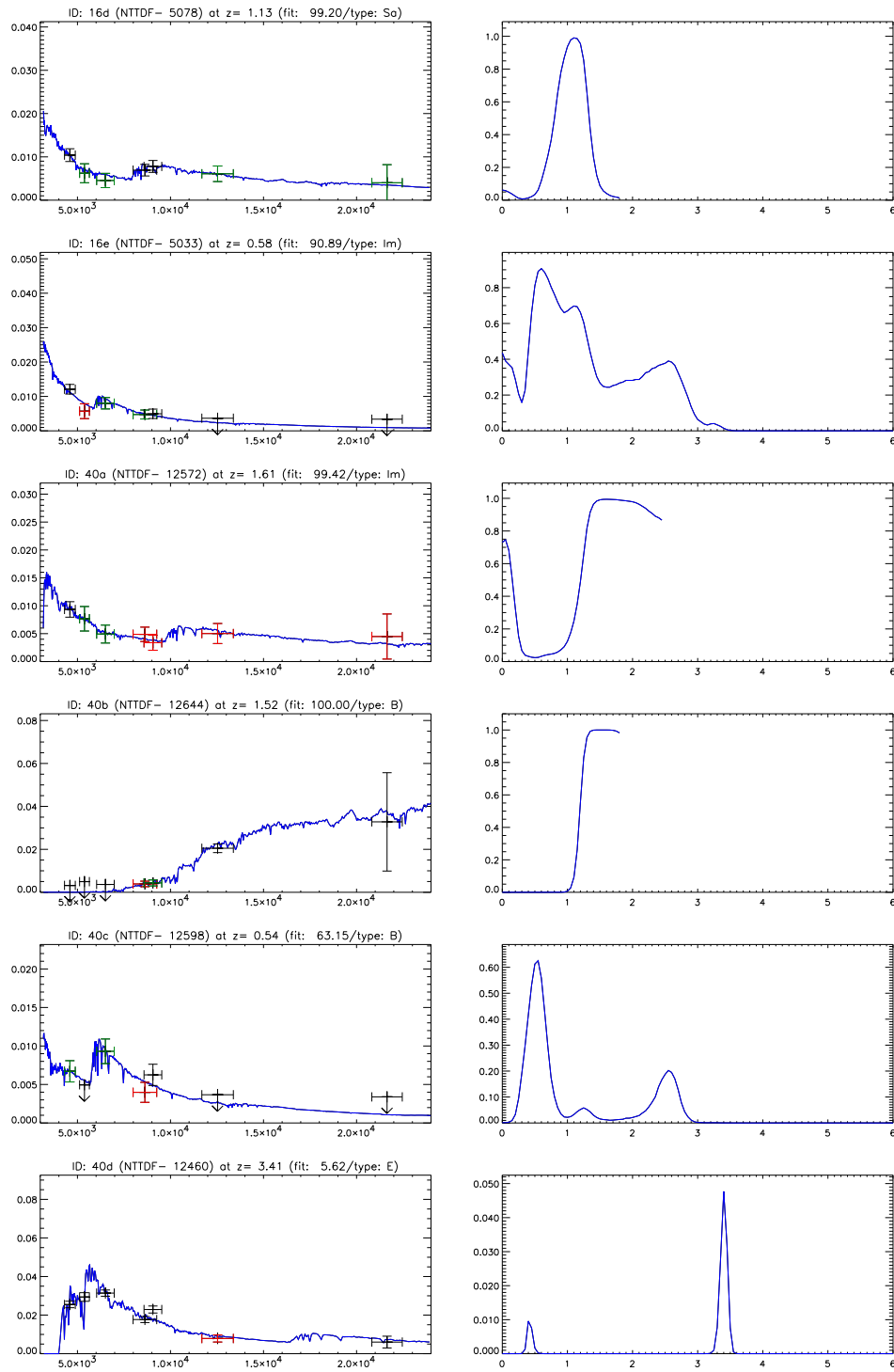


Figure A.3 (cont'd)

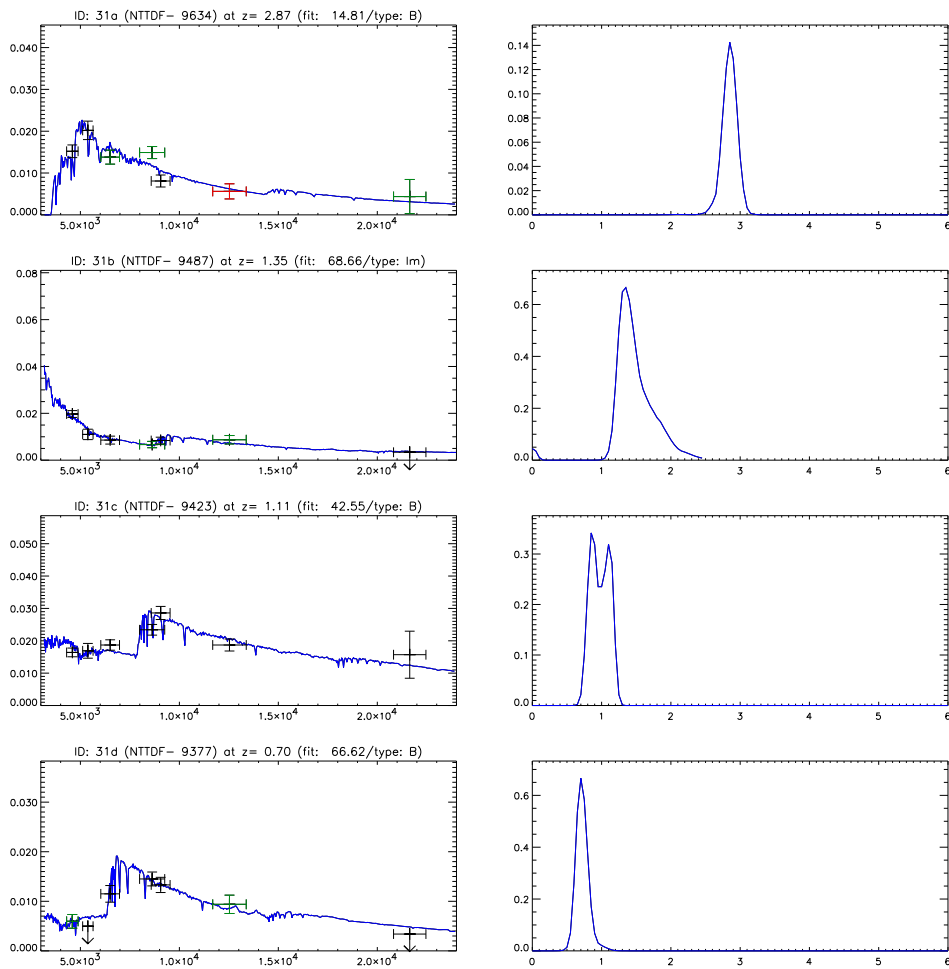


Figure A.3 (cont'd)

```

# Parameters file
AOVSED /home/dannerb/ZPHOT/filters/AOV_KUR_BB.SED # Vega SED
FILTERS_RES /home/dannerb/ZPHOT/filters/FILTER.RES # filters' transmission
FILTERS_FILE /home/dannerb/ZPHOT/filters/NTTDFBVRIZJKnew.param # filters' file
TEMPLATES_FILE spectra.param # models file
FILT_M_ABS 157 # filter for absolute magnitude
ERR_MAG_MIN 0.05 # err_min
Z_MIN 0.00 # minimum redshift
Z_MAX 6.00 # maximum redshift
Z_STEP 0.05 # step in redshift
ZSTEP_TYPE 0 # 0 step = Z_STEP
# 1 step = Z_STEP*(1+z)
CATALOG_TYPE 0 # cat.type
# 0 z/cat
# 1 z/obj
CATALOG_FILE /home/dannerb/MAMBO_PROJEKT/CATALOG_NTTDF/MAMBO_paper.cat # cat file
MAG_TYPE 0 # 0 standard Vega mag, 1 AB mag
REDDENING_LAW 5 # reddening law
# 0 no reddening
# 1 Allen (1976) MW
# 2 Seaton (1979) MW
# 3 Fitzpatrick (1983) LMC
# 4 Prevot (1984) Bouchet (1985) SMC
# 5 Calzetti (2000)
AV_MIN 0.00 # Av_min
AV_MAX 2.00 # Av_max
AV_STEP 0.20 # Av_err
AGE_CHECK y # check age gal. < age universe
PROB_THRESH 10.00 # prob. thresh. for second. max. (0,100)
OUTPUT_FILE RESULTSmambo_paper_new # name of output files (no extension)
OUTPUT_TYPE 0 # 0 2.E-17 erg/cm^2/s/A, 1 microJy, 2 mag_AB
SED_OBS_FILE y # file .obs_sed
SED_TEMP_FILE n # file .temp_sed
LOGPHOT_FILE n # file .log_phot
CATPHOT_FILE n # file .cat_phot
ZPHOT_FILE y # file .z_phot
H0 70. # Hubble constant
# used to compute absolute magnitude and
# ages if AGE_CHECK = y
OMEGA_M 0.3 # density parameter (matter)
# used to compute absolute magnitude and
# ages if AGE_CHECK = y
OMEGA_V 0.7 # density parameter (Lambda)
# used to compute absolute magnitude and
# ages if AGE_CHECK = y
##### cluster option #####
#Z_CLUSTER 1. # redshift of cluster

##### optional parameters #####
M_ABS_MIN -28. # minimum absolute magnitude (bright)
M_ABS_MAX -15. # maximum absolute magnitude (faint)
MATRIX n # file .m for each object
SPECTRUM n # file .spe for each object
EBV_MW 0.03 # E(B-V) for galactic dereddening

```

Figure A.4 Example for the setup applied for the photometric redshift estimation based on the broad-band optical/near-infrared data with *hyperz*.

Bibliography

- Adelberger, K. 2001, in: ‘Starburst Galaxies: Near and Far’, eds. L. Tacconi, D. Lutz, Springer Proceedings in Physics 88, 318 3.3.1
- Alexander, D. M. et al. 2003, AJ, 125, 383 1.1
- Almaini, O. et al. 2003, MNRAS, 338, 303 1.1
- Archibald, E. N. & Coulson, I. 2000, Estimating SCUBA Integration Time, http://www.jach.hawaii.edu/JACpublic/JCMT/Continuum_observing/SCUBA/alloc/call00b.html#inttimes 2.1
- Arexaga, I., Hughes, D. H., Chapin, E. L., Gaztañaga, E., Dunlop, J. S., & Ivison, R. J. 2003, MNRAS, 342, 759 1.2.3, 3.4
- Arnouts, S., D’Odorico, S., Cristiani, S., Zaggia, S., Fontana, A., & Giallongo, E. 1999, A&A, 341, 641 1.3, 2.2, 2.2
- Baade, D. et al. 1998, The ESO Messenger, 93, 13 2.2
- Baade, D. et al. 1999, The ESO Messenger, 95, 15 2.2
- Barger, A. J., Cowie, L. L., Sanders, D. B., Fulton, E., Taniguchi, Y., Sato, Y., Kawara, K., & Okuda, H. 1998, Nature, 394, 248 1.2.2
- Barger, A. J., Cowie, L. L., & Sanders, D. B. 1999, ApJ, 518, L5 3.3.4
- Barger, A.J., Cowie, L.L., Richards, A.E. 2000, AJ, 119, 2092 1.2.2, 3.3.1, 3.3.2
- Barger, A. J., Cowie, L. L., Mushotzky, R. F., Richards, E. A. 2001a, AJ, 121, 662 1.1
- Barger, A. J., Cowie, L. L., Steffen, A. T., Hornschemeier, A. E., Brandt, W. N., Garmire, G. P. 2001b, ApJ, 560, L23 1.1

- Bautz M.W., et al. 2000, ApJ, 543, L119 1.1
- Bertin, E. & Arnouts, S. 1996, A&AS, 117, 393 2.2.3
- Bertoldi, F. et al. 2000, A&A, 360, 92 1.2.2, 2.2.3, 2.3.1, 2.4, 3.1.2, 3.2, 3.3.1, 3.4
- Blain, A. W. & Longair, M. S. 1993, MNRAS, 264, 509 1.2, 1.2.1
- Blain, A. W., Smail, I., Ivison, R. J., Kneib, J.-P., & Frayer, D. T. 2002, Phys. Rep., 369, 111 1.1, 3.3.2
- Blain, A. W., Barnard, V. E., & Chapman, S. C. 2003, MNRAS, 338, 733 3.4
- Bogges, N. W. et al. 1992, ApJ, 397, 420 1.1
- Bolzonella, M., Miralles, J.-M., & Pelló, R. 2000, A&A, 363, 476 3.3.4, A
- Borys, C., Chapman, S., Halpern, M., & Scott, D. 2003, MNRAS, 344, 385 3.3.3
- Carilli, C. L., & Yun, M. S. 1999, ApJ, 513, L13 1.2.2, 1.2.3, 3.2.2, 3.3.1, 3.3.2, 3.3.4
- Carilli, C. L., & Yun, M. S. 2000, ApJ, 530, 618 1.2.2, 1.2.3, 3.2.2, 3.5, 3.3.1, 3.3.3, 3.3.4, 3.4
- Chapman, S. C. et al. 2000, MNRAS, 319, 318 3.1.1, 3.3.1
- Chapman, S.C., Richards, E.A., Lewis, G.F., Wilson, G., Barger, A.J. 2001, ApJ, 548, L147 3.3.1, 3.3.2
- Chapman, S. C., Shapley, A., Steidel, C., & Windhorst, R. 2002a, ApJ, 572, L1 3.1.1
- Chapman, S. C., Smail, I., Ivison, R. J., Helou, G., Dale, D. A., & Lagache, G. 2002b, ApJ, 573, 66 3.3.2, 3.3.2, 3.3.3
- Chapman, S. C. et al. 2003a, ApJ, 585, 57 3.3.2, 3.3.3
- Chapman, S. C., Blain, A. W., Ivison, R. J., & Smail, I. R. 2003b, Nature, 422, 695 2.4, 2.4, 3.4
- Chapman, S. C., Windhorst, R., Odewahn, S., Yan, H., & Conselice, C. 2003c, ApJ, 599, 92 3.3.3

- Cimatti, A., et al. 2002, *A&A*, 392, 395 A
- Colina, L., et al. 2001, *ApJ*, 563, 546 3.3.3
- Condon, J. J. 1992, *ARA&A*, 30, 575. 1.2.2
- Coppin, K., et al. 2002, *BAAS*, 201, #06.19 3.3.1
- Cowie, L. L., Barger, A. J., & Kneib, J.-P. 2002, *AJ*, 123, 2197 1.1, 3.3.1, 3.3.4
- De Breuck, C., van Breugel, W., Röttgering, H., Miley, G., & Carilli, C. 1999a, *Looking Deep in the Southern Sky*, 246 3.3.1
- De Breuck, C., van Breugel, W., Minniti, D., Miley, G., Röttgering, H., Stanford, S. A., & Carilli, C. 1999b, *A&A*, 352, L51 3.3.1
- De Breuck, C. et al. 2004, *A&A*, in press, (astro-ph/0405339) 3.3.1
- De Jong, T., Klein, U., Wielebinski, R., & Wunderlich, E. 1985, *A&A*, 147, L6 1.2.2
- Devillard N. 1997, *The ESO Messenger*, 87, 19 2.2.2
- Dickinson, M., et al. 2000, *ApJ*, 531, 624 3.3.1
- Dole, H. et al. 2001, *A&A*, 372, 364 1.1, 3.3.3
- Downes, A. J. B., Peacock, J. A., Savage, A., & Carrie, D. R. 1986, *MNRAS*, 218, 31 3.2.1, 3.2.2
- Downes, D. et al. 1999, *A&A*, 347, 809 2.2.3, 2.3.1, 3.3.1, 3.4, 3.4
- Dunlop, J. S. et al. 2002, *MNRAS*, submitted, (astro-ph/0205480) 1.2.2, 3.3.1, 3.4
- Dunne, L., Eales, S., Edmunds, M., Ivison, R., Alexander, P., Clements, D. 2000a, *MNRAS*, 315, 115 3.3.3, 3.33
- Dunne, L., Clements, D. L., & Eales, S. A. 2000b, *MNRAS*, 319, 813 1.2.3
- Eales, S., Lilly, S., Gear, W., Dunne, L., Bond, J. R., Hammer, F., Le Fèvre, O., & Crampton, D. 1999, *ApJ*, 515, 518 1.2.2
- Eales, S., Lilly, S., Webb, T., Dunne, L., Gear, W., Clements, D., & Yun, M. 2000, *AJ*, 120, 3.3.3

- Eales, S., Bertoldi, F., Ivison, R., Carilli, C., Dunne, L., & Owen, F. 2003, MNRAS, 344, 169 2.5, 3.2.2, 3.2.2, 3.2.2, 3.2.2, 3.2.2, 3.2.2, 3.5, 3.4
- Efstathiou, A. & Rowan-Robinson, M. 2003, MNRAS, 343, 322 3.3.3
- Eggen, O. J., Lynden-Bell, D., & Sandage, A. R. 1962, ApJ, 136, 748 1.1
- Ellis, R. 1998, Nature, 395, A3 1.1
- Fabian, A. C. et al. 2000, MNRAS, 315, L8 1.1
- Fardal, M. A., Katz, N., Weinberg, D. H., Davé, R., & Hernquist, L. 2001, ApJ, submitted, (astro-ph/0107290) 3.3.3, 3.3.3
- Fernández-Soto, A., Lanzetta, K. M., & Yahil, A. 1999, ApJ, 513, 34 A
- Fixsen, D. J. et al. 1994, ApJ, 420, 457 1.1
- Fixsen, D. J., Dwek, E., Mather, J. C., Bennett, C. L., & Shafer, R. A. 1998, ApJ, 508, 123 1.1, 3.3.3
- Fomalont, E. B. 1999, in Synthesis Imaging in Radio Astronomy II, A Collection of Lectures from the Sixth NRAO/NMIMT Synthesis Imaging Summer School, Ed. G. B. Taylor, C. L. Carilli, and R. A. Perley., ASP Conf. Series, 180, 301 1.2.2, 2.2.2, 3.2.1
- Fox, M. J. et al. 2001, MNRAS, 331, 839 2.1, 3.3.1, 3.3.4
- Frayer, D. T., et al. 1998, ApJ, 506, L7 1.2, 1.2.2, 1.2.3
- Frayer, D. T., et al. 1999, ApJ, 514, L13 1.1, 1.2.2, 1.2.3
- Frayer, D. T., Smail, I., Ivison, & Scoville, N. Z. 2000, AJ, 120, 1668 3.4
- Frayer, D. T., Armus, L., Scoville, N. Z., Blain, A. W., Reddy, N. A., Ivison, R. J., & Smail, I. 2003, AJ, 126, 73 2.4, 3.2.2
- Franx, M. et al. 2003, ApJ, 587, L79 3.31, 3.3.1
- Fukugita, M., Hogan, C. J., & Peebles, P. J. E. 1998, ApJ, 503, 518 1.1
- Garrett, M. A. 2002, A&A, 384, L19 1.2.2

- Gear, W. K., Lilly, S. J., Stevens, J. A., Clements, D. L., Webb, T. M., Eales, S. A., & Dunne, L. 2000, MNRAS, 316, L51 3.3.1, 3.4
- Genzel, R., Tacconi, L. J., Rigopoulou, D., Lutz, D., & Tecza M. 2001, ApJ, 563, 527 1.1
- Genzel, R., Baker, A. J., Tacconi, L. J., Lutz, D., Cox, P., Guilloteau, S., & Omont, A. 2003, ApJ, 584, 633 1.1
- Gispert, R., Lagache, G., & Puget, J. L. 2000, A&A, 360, 1 1.1, 3.3.3
- Goldader, J. D., Meurer, G., Heckman T. M., Seibert M., Sanders, D. B., Calzetti, D. and Steidel C. C. 2002, ApJ, 568, 651 3.3.1, 3.3.1, 3.3.1, 3.3.3
- Greve, T. R., Ivison, R. J., Bertoldi, F., Stevens, J. A., Chapman, S. C., Smail, I., & Blain, A. W. 2003, to appear in the Proceedings of the ESO/USM/MPE Workshop on "Multiwavelength Mapping of Galaxy Formation and Evolution", (astro-ph/0312455) 3.3.3, 3.3.4
- Guilloteau, S., et al. 1992, A&A, 262, 624 1.2.2
- Hainaut, O., West, R. M., Smette, A., & Marsden, B. G. 1994, A&A, 289, 311 2.2.1
- Hainaut, O. R., Meech, K. J., Boehnhardt, H., & West, R. M. 1998, A&A, 333, 746 2.2.1
- Hainline, L. J., Scoville, N. Z., Yun, M. S., Hawkins, D. W., Frayer, D. T., & Isaak, K. G. 2004, ApJ, in press, (astro-ph/0403194) 1.2.2, 1.2.3
- Hamuy, M., Suntzeff, N. B., Heathcote, S. R., Walker, A. R., Gigoux, P., & Phillips, M. M. 1994, PASP, 106, 566 2.2.1, 2.4
- Hauser, M. G. et al. 1998, ApJ, 508, 25 1.1
- Hauser, M. G. & Dwek, E. 2001, ARA&A, 39, 249 1.1
- Heckman, T. M., Lehnert, M. D., Strickland, D. K., & Armus, L. 2000, ApJS, 129, 493 3.3.3
- Helou, G., Soifer, B. T., & Rowan-Robinson, M. 1985, ApJ, 298, L7 1.2.2
- Hernquist, L. & Springel, V. 2003, MNRAS, 341, 1253 3.35, 3.3.4

- Hoekstra, H. et al. 2001, *ApJ*, 548, L5 3.2.2
- Holland, W. S., Cunningham, C. R., Gear, W. K., Jenness, T., Laidlaw, K., Lightfoot, J. F., & Robson, E. I. 1998, *Proc. SPIE*, 3357, 305 1
- Holtzman, J. A., Burrows, C. J., Casertano, S., Hester, J. J., Trauger, J. T., Watson, A. M., & Worthey, G. 1995, *PASP*, 107, 1065 6
- Hornschemeier, A. E. et al. 2000, *ApJ*, 541, 49 1.1
- Hughes, D. H. et al. 1998, *Nature*, 394, 241 1.1, 1.2.2, 3.4
- Im, M., Yamada, T., Tanaka, T., Kajisawa, M. 2002, *ApJ*, 578, L19 3.3.1
- Iverson, R. J., Smail, I., Le Borgne, J.-F., Blain, A. W., Kneib, J.-P., Bezecourt, J., Kerr, T. H., & Davies, J. K. 1998, *MNRAS*, 298, 583 1.2, 3.4
- Iverson, R. J., Smail, I., Barger, A. J., Kneib, J.-P., Blain, A. W., Owen, F. N., Kerr, T. H., & Cowie, L. L. 2000a, *MNRAS*, 315, 209 2.4, 3.3.1, 3.4
- Iverson R.J., Dunlop J.S., Smail I., et al. 2000b, *ApJ*, 542, 27 3.3.1
- Iverson, R. J. et al. 2002, *MNRAS*, 337, 1 3.1.1, 3.2.1, 3.2.2, 3.3.1, 4, 3.26, 3.3.1, 3.6, 3.3.1, 3.29, 3.3.2, 3.3.3, 3.3.3, 3.3.4, 3.35, 3.4
- Jimenez, R., Friaca, A. C. S., Dunlop, J. S., Terlevich, R. J., Peacock, J. A., & Nolan, L. A. 1999, *MNRAS*, 305, 16 3.3.3
- Kashikawa, N. et al. 2003, *AJ*, 125, 53 A
- Kaviani, A., Haehnelt, M. G., & Kauffmann, G. 2003, *MNRAS*, 340, 739 3.3.3
- Kennicutt, R. C. 1998, *ApJ*, 498, 541 5, 3.3.4
- Klaas, U. et al. 2001, *A&A*, 379, 823 3.3.1, 3.3.1
- Kreysa, E. et al. 1998, *Proc. SPIE*, 3357, 319 1.3, 2.1
- Kurz, R., Guilloteau, S., & Shaver, P. 2002, *The Messenger*, 107, 7 11
- Lagache, G., Abergel, A., Boulanger, F., Désert, F. X., & Puget, J.-L. 1999, *A&A*, 344, 322 1.1

- Lagache, G. & Dole, H. 2001, *A&A*, 372, 702 1.1, 3.3.3
- Landolt, A. U. 1992, *AJ*, 104, 340 2.2.1
- Lanzetta, K. M., Yahata, N., Pascarelle, S., Chen, H., & Fernández-Soto, A. 2002, *ApJ*, 570, 492 3.3.4
- Lawrence, A. 2001, *MNRAS*, 323, 147 1.2
- Ledlow, M. J., Smail, I., Owen, F. N., Keel, W. C., Ivison, R. J., & Morrison, G. E. 2002, *ApJ*, 577, L79 2.4, 3.3.1, 3.3.1
- Lehnert, M. D., Heckman, T. M., & Weaver, K. A. 1999, *ApJ*, 523, 575 3.3.3
- Lehnert, M. D. & Bremer, M. 2003, *ApJ*, 593, 630 3.3.4, 3.35
- Lilly, S. J., Le Fevre, O., Hammer, F., & Crampton, D. 1996, *ApJ*, 460, L1 3.3.4
- Lilly, S. J., Eales, S. A., Gear, W. K. P., Hammer, F. ;., Le Fèvre, O., Crampton, D., Bond, J. R., & Dunne, L. 1999, *ApJ*, 518, 641 1.1, 1.2.2
- Lisenfeld, U., Isaak, K. G., & Hills, R. 2000, *MNRAS*, 312, 433 3
- Low, F. J. et al. 1984, *ApJ*, 278, L19 3
- Lutz, D. et al. 2001, *A&A*, 378, 70 1.1, 3.3.3, 3.3.4, 3.4
- Madau, P., Ferguson, H. C., Dickinson, M. E., Giavalisco, M., Steidel, C. C., & Fruchter, A. 1996, *MNRAS*, 283, 1388 3.3.4
- Maihara, T., et al. 2001, *PASJ*, 53, 25 3.3.1
- Mather, J. C., Fixsen, D. J., Shafer, R. A. 1993, in *Proc. SPIE Conf. 2019, Infrared Spaceborne Remote Sensing*, ed. M. S. Scholl (Bellingham: SPIE), 168 1.1
- Mather, J. C., Fixsen, D. J., Shafer, R. A., Mosier, C., & Wilkinson, D. T. 1999, *ApJ*, 512, 511 1.1
- McMahon, R. G., Omont, A., Bergeron, J., Kreysa, E., & Haslam, C. G. T. 1994, *MNRAS*, 267, L9 2.1
- McLean, I. S. et al. 1998, *Proc. SPIE*, 3354, 566 2.4

- Meisenheimer, K. 1998, User Guide to the CAFOS 2.2, <http://www.mpia-hd.mpg.de/CAFOS22/cafos22.ps> 2.2.1
- Mirabel, I.F., Lutz, D., Maza, J. 1991, *A&A*, 243, 367 3.3.3
- Monet, D. et al. 1996, USNO-SA1.0, (U.S. Naval Observatory, Washington DC). 2.2.1
- Moran, James M. 1998, Submillimeter array , Proc. SPIE Vol. 3357, p. 208-219, *Advanced Technology MMW, Radio, and Terahertz Telescopes*, Ed. Thomas G. Phillips 10
- Moorwood, A., Cuby, J. G., & Lidman, C. 1998a, *The ESO Messenger*, 91, 9 2.2
- Moorwood, A. et al. 1998b, *The ESO Messenger*, 94, 7 2.2
- Neri, R., et al. 2003, *ApJ*, 597, L113 1.1, 1.2.2, 1.2.3, 2.4, 3.2.2, 3.3.1, 3.3.1, 3.4, 3.4
- Oke, J. B., & Gunn, J. E. 1983, *ApJ* 266, 713 2.2.1, 2.2
- Omont, A., McMahon, R. G., Cox, P., Kreysa, E., Bergeron, J., Pajot, F., & Storrie-Lombardi, L. J. 1996a, *A&A*, 315, 1 2.1
- Omont, A., Petitjean, P., Guilloteau, S., McMahon, R. G., Solomon, P. M., & Pecontal, E. 1996b, *Nature*, 382, 428 2.1
- Pahre, M. A., Djorgovski, S. G., & de Carvalho, R. R. 1998, *AJ*, 116, 1591 3.2.2
- Papovich, C., Dickinson, M., & Ferguson, H. C. 2001, *ApJ*, 559, 620 3.2.9, 3.3.1, 6
- Partridge, R. B. & Peebles, P. J. E. 1967, *ApJ*, 148, 377 1.1
- Peacock, J. A. 1999, *Cosmological physics*. Publisher: Cambridge, UK: Cambridge University Press, 1999. ISBN: 0521422701, 3.2.2
- Persic, M. & Salucci, P. 1992, *MNRAS*, 258, 14P 1.1
- Persson, S. E., Murphy, D. C., Krzeminski, W., Roth, M., & Rieke, M. J. 1998, *AJ*, 116, 2475 2.2.2, 2.2.2
- Pozzetti, L., Madau, P., Zamorani, G., Ferguson, H. C., & Bruzual A., G. 1998, *MNRAS*, 298, 1133 3.2.2
- Pozzetti, L. & Mannucci, F. 2000, *MNRAS*, 317, L17 3.3.1, 3.31

- Puget, J.-L., Abergel, A., Bernard, J.-P., Boulanger, F., Burton, W. B., Desert, F.-X., & Hartmann, D. 1996, *A&A*, 308, L5 1.1, 3.3.3
- Puget, J. L. et al. 1999, *A&A*, 345, 29 1.1, 3.3.3
- Richards, E. A. 1999, *ApJ*, 513, L9 3.4
- Richards, E. A. 2000, *ApJ*, 533, 611 1.2.2, 3.2.1
- Salpeter, E. E. 1955, *ApJ*, 121, 161 3.3.4
- Sanders, D. B., Scoville, N. Z., & Soifer, B. T. 1991, *ApJ*, 370, 158 3
- Sanders, D. B., & Mirabel, I. F. 1996, *ARA&A*, 34, 749 3.3.3
- Sanders, D.B. 1999, *Ap&SS*, 269, 381 1.1
- Schink, H. et al. 2000, *Proc. SPIE*, 4008, 175. 2.4
- Schirmer, M., Erben, T., Schneider, P., Pietrzynski, G., Gieren, W., Micol, A., & Pierfederici, F. 2003, *A&A*, 407, 869 2.2.1
- Schlegel, D. J., Finkbeiner, D. P., & Davis, M. 1998, *ApJ*, 500, 525 1.1
- Schneider, D. P., Gunn, J. E., Hoessel, J. G. 1983, *ApJ*, 264, 337 2.2.1
- Scott, S. E. et al. 2002, *MNRAS*, 331, 817 1.2.2, 2.1, 3.2.1, 3.3.1
- Searle, L. & Zinn, R. 1978, *ApJ*, 225, 357 1.1
- Seifert, W. et al. 2000, *Proc. SPIE*, 4008, 96. 2.2
- Shapley, A. E., Steidel, C. C., Adelberger, K. L., Dickinson, M., Giavalisco, M., & Pettini, M. 2001, *ApJ*, 562, 95 3.1.1, 3.3.1
- Silverberg, R. F., Hauser, M. G., Boggess, N. W., Kelsall, T. J. et al. 1993, in *Proc. SPIE Conf. 2019, Infrared Spaceborne Remote Sensing*, ed. M. S. Scholl (Bellingham: SPIE), 180 1.1
- Smail, I., Ivison, R. J., & Blain, A. W. 1997, *ApJ*, 490, L5 1.1, 1.2, 1.2.2
- Smail, I., Ivison, R. J., Kneib, J.-P., Cowie, L. L., Blain, A. W., Barger, A. J., Owen, F. N., & Morrison, G. 1999, *MNRAS*, 308, 1061 2.1, 3.2.2

- Smail, I., Ivison, R.J., Blain, A.W., Kneib J.-P. 2002a, MNRAS, 331, 495 1.2, 2.4, 3.3.1, 3.3.1, 3.3.1, 3.29
- Smail, I., Owen, F. N., Morrison, G. E., Keel, W. C., Ivison, R. J., & Ledlow, M. J. 2002b, ApJ, 581, 844 3.3.4, 3.35
- Smail, I., Ivison, R. J., Gilbank, D. G., Dunlop, J. S., Keel, W. C., Motohara, K., & Stevens, J. A. 2003, ApJ, 583, 551 3.3.4
- Soucail, G., Kneib, J.P., Bézecourt, J., Metcalfe, L., Altieri, B., & Le Borgne, J. F. 1999, A&A, 343, L70 2.4, 3.3.3
- Springel, V. & Hernquist, L. 2003a, MNRAS, 339, 289 3.35, 3.3.4
- Springel, V. & Hernquist, L. 2003b, MNRAS, 339, 312 3.35, 3.3.4
- Stanway, E. R., Bunker, A. J., & McMahon, R. G. 2003a, MNRAS, 342, 439 3.3.4, 8, 3.35
- Stanway, E., Bunker, A., McMahon, R., Ellis, R., Treu, T., & McCarthy, P. 2003b, ApJ, in press, (astro-ph/0308124) 3.3.4, 8, 3.35
- Steidel, C. C., Giavalisco, M., Dickinson, M., & Adelberger, K. L. 1996, AJ, 112, 352 1.1, 3.3.4, 3.3.4, 8, 3.35
- Steidel, C. C., Adelberger, K. L., Giavalisco, M., Dickinson, M., & Pettini, M. 1999, ApJ, 519, 1 3.3.4, 3.3.4, 8, 3.35
- Steidel, C. C., Shapley, A. E., Pettini, M., Adelberger, K. L., Erb, D. K., Reddy, N. A., & Hunt, M. P. 2004, ApJ, in press, (astro-ph/0401439) 1
- Surace, J., Sanders, D.B. 2000, ApJ, 120, 604 3.3.3
- Tacconi, L. J., Genzel, R., Lutz, D., Rigopoulou, D., Baker, A. J., Iserlohe, C., & Tecza, M. 2002, ApJ, 580, 73 1.1, 3.3.3
- Tan, J. C., Silk, J., & Balland, C. 1999, ApJ, 522, 579 1.1
- Thompson, D., & Bizenberger, P. 1999, Omega Prime - Observer's Manual, http://www.mpia-hd.mpg.de/IRCAM/OPRIME/Manual/OP_manual.html 2.2.2

- Thornley, M.D., Förster Schreiber, N.M., Lutz, D., Genzel, R., Spoon, H.W.W., Kunze, D., Sternberg, A. 2000, *ApJ*, 539, 641 3.3.3
- Thuan, T. X. & Gunn, J. E. 1976, *PASP*, 88, 543 2.2.1
- Thum, C. 2004, *MPIfR Bolometer Arrays*,
http://www.iram.fr/GENERAL/calls/calls_s04/node17.html 2.1
- Totani, T., Yoshii, Y., Iwamuro, F., Maihara, T., Motohara, K. 2001a, *ApJ*, 558, L57 3.3.1
- Totani, T., Yoshii, Y., Maihara, T., Iwamuro, F., & Motohara, K. 2001b, *ApJ*, 559, 592 3.2.2
- Trager, S. C., Faber, S. M., Worthey, G., & González, J. J. 2000a, *AJ*, 119, 1645 1.1
- Trager, S. C., Faber, S. M., Worthey, G., & González, J. J. 2000b, *AJ*, 120, 165 1.1
- Trentham, N., Kormendy, J., Sanders, D.B. 1999, *AJ*, 117, 2152 3.3.1, 3.3.1, 3.3.1
- Turon, C., et al. 1995, *A&A*, 304, 82 2.2.2
- Turon, C. 1999, *C.R. Acad. Sci. Ser. II*, 327, 161-172 (1999), 327, 161 2.2.2
- van Dokkum, P. G. et al. 2003, *ApJ*, 587, L83 3.3.1
- van Leeuwen, F. 1996, *Space Science Reviews*, 81, 201 2.2.2
- Venemans, B. P. et al. 2002, *ApJ*, 569, L11 5
- Vikhlinin, A., McNamara, B. R., Forman, W., Jones, C., Quintana, H., & Hornstrup, A. 1998, *ApJ*, 502, 558 2.1
- Webb, T. M. et al. 2003a, *ApJ*, 582, 6 3.3.1, 3.29
- Webb, T. M. A. et al. 2003b, *ApJ*, 587, 41 3.3.1, 3.3.1, 3.29
- Webb, T. M. A., Lilly, S. J., Clements, D. L., Eales, S., Yun, M., Brodwin, M., Dunne, L., & Gear, W. K. 2003c, *ApJ*, 597, 680 3.3.1
- Wiklind, T. 2003, *ApJ*, 588, 736 1.2.3, 3.4

- Williams, R. E. et al. 1996, AJ, 112, 1335 3.3.1, 6, A
- Yan, L., McCarthy, P. J., Freudling, W., Teplitz, H. I., Malumuth, E. M., Weymann, R. J., & Malkan, M. A. 1999, ApJ, 519, L47 3.3.4, 3.35
- Yun, M. S., Reddy, N. A., & Condon, J. J. 2001, ApJ, 554, 803 1.2.2, 3.3.4
- Yun, M. S. & Carilli, C. L. 2002, ApJ, 568, 88 1.2.3, 3.4
- Zheng, Z., Wu, H., Mao, S., Xia, X.-Y., Deng, Z.-G., Zou, Z.-L. 1999, A&A, 349, 735 3.3.3
- Zylka, R., 1998, Pocket Cookbook for the MOPSI Software.
<http://www.iram.es/IRAMES/otherDocuments/manuals/Index.html> 2.5

List of Tables

2.1	Summary of the multi-wavelength follow-up observations of the NDF . . .	24
2.2	PdBI positions and fluxes of the five MAMBO 1.2 mm galaxies	27
2.3	MAMBO on-off observations	35
3.1	Fluxes of the three NDF mm galaxies with PdBI detections	41
3.2	Fluxes of the Abell 2125 PdBI detection	41
3.3	NDF MAMBO sources and associated 1.4 GHz radio sources	47
3.4	Optical/near-infrared objects close to the interferometric positions	51
3.4	Optical/near-infrared objects close to the interferometric positions	53
3.5	Main properties of counterparts to MAMBO Sources	66
3.6	Submm/mm sources with interferometric confirmation	71
3.7	SFR of MAMBO galaxies in the NDF	94
3.8	SFRD	96
3.9	Comparison between the MAMBO 1.2 mm and the SCUBA 8 mJy survey	98

List of Figures

2.1	MAMBO 1.2 mm mosaic map centered on the NTT Deep Field	12
2.2	Comparison between the ESO SUSI and our WFI data	18
2.3	<i>SExtractor</i> setup	22
2.4	Example of source extraction in the K band	23
2.5	“Dirty” 1.26 mm interferometric maps and beams for the PdBI detections	26
2.6	MXU Mask-1.	30
2.7	Two-dimensional raw and reduced spectrum of two objects	31
2.8	Presentation of $\approx 70\%$ of the on-off data taken on MM J120539-0741.0. . .	34
2.9	Map flux versus on-off flux for the sample presented in Tab. 2.3.	36
3.1	K-, I-, and R-band images for the fields of the three NDF PdBI detections	39
3.2	ISAAC K-band images of the fields of two PdBI detections	40
3.3	K- and R-band image of the MAMBO source J154127+6615	40
3.4	Reliability test	44
3.5	Histogram of the separations between the mm and radio position	45
3.6	Radio-mm offset	46
3.7	BzK composites of the NDF MAMBO sources with interferometric positions	49
3.8	BVRIZJK images for the field of MM J120507–0748.1	57
3.9	BVRIZJK images for the field of MM J120508–0743.1	57
3.10	BVRIZJK images for the field of MM J120508–0740.1	58
3.11	BVRIZJK images for the field of MM J120510–0747.0	58
3.12	BVRIZJK images for the field of MM J120516–0739.4	59
3.13	BVRIZJK images for the field of MM J120517–0743.1	59
3.14	BVRIZJK images for the field of MM J120519–0749.5	60
3.15	BVRIZJK images for the field of MM J120520–0738.9	60
3.16	BVRIZJK images for the field of MM J120522–0745.1	61
3.17	BVRIZJK images for the field of MM J120524–0747.3	61
3.18	BVRIZJK images for the field of MM J120526–0746.6	62
3.19	BVRIZJK images for the field of MM J120530–0741.6	62
3.20	BVRIZJK images for the field of MM J120530–0747.7	63
3.21	BVRIZJK images for the field of MM J120531–0748.1	63
3.22	BVRIZJK images for the field of MM J120534–0738.3	64
3.23	BVRIZJK images for the field of MM J120539–0745.4	64
3.24	BVRIZJK images for the field of MM J120545–0738.8	65

3.25	BVRIZJK images for the field of MM J120546–0741.5	65
3.26	Distribution of K and I magnitudes for interferometrically located samples	68
3.27	MAMBO 1.2 mm flux vs. K magnitude for radio-identified NDF galaxies	69
3.28	Expected K-band magnitude of a mm galaxy as a function of redshift	72
3.29	I–K vs. K magnitude-color diagram for MAMBO and SCUBA samples	74
3.30	Expected (J–K) color of a mm galaxy as a function of redshift	76
3.31	(I–K) vs. (J–K) diagnostic plot applied to a sample of (sub)mm galaxies	77
3.32	Diagnostic diagram for the near-infrared to radio SEDs of (sub)mm sources	84
3.33	Near-infrared/submm vs. submm/radio spectral indices for cool galaxies	87
3.34	Optical/NIR photometric z versus z from the radio/mm spectral index	91
3.35	Star-formation-rate density for different object classes at different epochs	95
A.1	Comparison of observed spectra with best SED fits of <i>hyperz</i>	102
A.2	Spectroscopic redshift versus photometric redshift for NDF sources	103
A.3	Best-fit SED for objects close to the interferometric positions	104
A.3	(cont'd)	105
A.3	(cont'd)	106
A.3	(cont'd)	107
A.3	(cont'd)	108
A.3	(cont'd)	109
A.3	(cont'd)	110
A.3	(cont'd)	111
A.3	(cont'd)	112
A.3	(cont'd)	113
A.3	(cont'd)	114
A.3	(cont'd)	115
A.3	(cont'd)	116
A.3	(cont'd)	117
A.4	Setup of <i>hyperz</i>	118

Danksagung

An erster Stelle möchte ich mich bei Herrn Professor Reinhard Genzel herzlich bedanken, der mir die Möglichkeit gab, in einem wissenschaftlich sehr interessanten und hochaktuellen Forschungsgebiet meine Promotionsarbeit in seiner Arbeitsgruppe durchzuführen.

Ausserdem bedanke ich mich bei:

- Dr. Matthew D. Lehnert und Dr. Dieter Lutz, die mich während meiner Promotionsarbeit tatkräftig unterstützten, immer Zeit für wissenschaftliche Diskussionen über MAMBO-Quellen hatten und sowohl aufmerksam als auch kritisch die vorliegende Arbeit korrekturlasen. All dies trug wesentlich zum Gelingen dieser Arbeit bei.
- Dr. Linda Tacconi, die großen Anteil an der erfolgreichen Detektion von MAMBO-Quellen mit dem PdBI hatte.
- Dr. Frank Bertoldi und Prof. Karl Menten, die mit der Durchführung des MAMBO-Surveys die Basis für diese vorliegende Arbeit schufen.
- Dr. Chris C. Carilli, ohne dessen VLA-Beobachtungen die Identifikation einer großen Anzahl von MAMBO-Quellen im optischen/NIR unmöglich gewesen wäre.
- Prof. Dave Sanders, durch dessen Zusammenarbeit es uns möglich war, den NIR-Spektrographen NIRSPEC am KECKII in Hawaii zu verwenden, um interessante MAMBO-Quellen zu beobachten.
- Dr. Thomas Erben und Mischa Schirmer, die uns eine von ihnen entwickelte Datenreduktionspipeline zur Verfügung stellten, um die zeit- und speicherintensiven WFI-Daten zu reduzieren und eine hilfreiche Unterstützung bei der Reduktion dieser waren.
- Mitarbeitern verschiedener Observatorien (Calar Alto, ESO, IRAM und KECK), deren Hilfe und Unterstützung beitrug erfolgreiche Beobachtungen durchzuführen, die unentbehrlich für meine Promotionsarbeit waren.
- Marco Barden, Dr. Peter Englmaier, Dr. Lowell Tacconi-Garman, Dr. Thomas Ott und Jimmy Viehhauser, die immer schnell und kompetent auftretende Computer- und/oder Netzwerkprobleme lösten und bei Bedarf Installationen von notwendiger Software durchführten.
- Dr. Andrea Gilbert, die zügig und sehr aufmerksam das vorliegende Manuskript korrekturlas.
- Dr. Thomas Müller, Dr. Daniel Schaudel und Dr. Eckhard Sturm, die immer ein offenes Ohr für mich hatten.
- Frau Susanne Harai-Ströbl, für ihre Unterstützung und Hilfe bei administrativen Angelegenheiten.
- meinen Eltern Manda und Helmut Dannerbauer, ohne deren immer währende Unterstützung ich es nie soweit gebracht hätte.
- meiner Frau Alexandra, die besonders in der finalen Phase der Promotionsarbeit viel Verständnis und Geduld aufbrachte, immer eine tolle Unterstützung war und mir somit half über manchen Tiefpunkt hinwegzukommen.

Abschließend möchte ich mich bei allen Diplomanden, Doktoranden und Mitarbeitern sowohl der Infrarotgruppe als auch den anderen Arbeitsgruppen des MPEs bedanken, die mir immer mit Rat und Tat zur Seite standen.

Lebenslauf

Persönliches

Name: Helmut Dannerbauer
Geburtsdatum: 2. Februar 1971
Geburtsort: München
Familienstand: verheiratet
Nationalität: deutsch

Ausbildung

1977-1981 Grundschule, München
1981-1983 Hauptschule, München
1983-1987 Realschule, München
1987 Mittlere Reife
1987-1990 Berufsausbildung zum Industriekaufmann bei Siemens München
1990 IHK Abschluss, Industriekaufmann
1990-1992 Berufsoberschule Wirtschaft, München
1992 Allgemeine Hochschulreife
1994-2000 Physikstudium an der Ludwig-Maximilians-Universität München
1996-1997 ERASMUS-Austauschprogramm, Universität von Sevilla
1999-2000 Diplomarbeit in Physik am
Max-Planck-Institut für extraterrestrische Physik, Garching
März 2000 Physikdiplom an der Ludwig-Maximilians-Universität München
2000-2004 Anfertigung der Dissertation am
Max-Planck-Institut für extraterrestrische Physik, Garching

Referierte Veröffentlichungen

“Properties of Millimeter Galaxies: Constraints from K-Band Blank Fields”,
Dannerbauer H., Lehnert M.D., Lutz D., Tacconi L., Bertoldi F., Carilli C., Genzel R. & Menten K.,
2002, ApJ, 573, 473

“The faint Counterparts of MAMBO mm Sources near the NTT Deep Field”,
Dannerbauer H., Lehnert M.D., Lutz D., Tacconi L., Bertoldi F., Carilli C., Genzel R. & Menten K.,
2004, ApJ, 606, 664

